

---

# High-precision ion trap for spectroscopy of Coulomb crystals

---

Von der Fakultät für Mathematik und Physik  
der Gottfried Wilhelm Leibniz Universität Hannover

zur Erlangung des Grades

Doktor der Naturwissenschaften  
Dr. rer. nat.

genehmigte Dissertation

von

Dipl.-Phys. Karsten Pyka  
geboren am 17. Januar 1983 in Röbel/Müritz

2013

Referent: Prof. Dr. Piet O. Schmidt  
Korreferent: Prof. Dr. Christian Ospelkaus  
Tag der Promotion: 14. Mai 2013

# Abstract

Trapped atomic ions represent well-controlled quantum systems with various applications, for example in precision spectroscopy, quantum information and quantum simulation, as well as in frequency standards. The latter have been providing significant contributions in numerous technical applications and physical experiments over the last 60 years.

Within the past two decades, a new generation of frequency standards has been taking its position next to the established systems based on atomic microwave transitions and has even surpassed the latter in terms of accuracy and stability, although not yet in terms of reliability. These frequency standards based on atomic optical transitions in particular systems based on trapped ions, offer an unprecedented level of control of the atomic system. Highest accuracies in frequency measurements are currently obtained with single ion or two-species ion systems due to the high environmental isolation.

In terms of stability, however, a limitation is set by the inherently low signal-to-noise ratio (SNR) of such systems, and an improvement by scaling up the number of ions was prevented so far because of increasing systematic frequency shifts due to imperfections in the trap geometry. In contrast, other systems based on neutral atom ensembles profit from their higher signal-to-noise ratio in terms of short-term stability, but experience a trade-off in environmental isolation which leads to a more difficult handling of systematic uncertainties.

The motivation of this work lies in the attempt to combine the advantages of both systems by developing a scalable trap structure to trap arrays of linear Coulomb crystals. Here, the gain in SNR should not be paid-off with a decrease in accuracy. To obtain a low accuracy with a larger ensemble of ions a detailed analysis of the trap design is done in terms of machining tolerances and alignment errors.

As a candidate for a multi-ion optical clock  $^{115}\text{In}^+$  is introduced, sympathetically cooled by  $^{172}\text{Yb}^+$  ions. The latter is further used as an atomic test system for the characterization of prototype ion traps, that are designed, assembled and tested in this work. The introduced experimental apparatus is optimized for tests of trap designs and measurements of residual radiofrequency (rf) fields, which can contribute significantly to systematic frequency shifts at the envisaged level in relative accuracy of  $< 10^{-18}$ .

The results of this work demonstrate the capability of the introduced trap design to enter a new regime of precision and control that is required in clock spectroscopy, geodesy or extra-terrestrial navigation.

Furthermore, the system serves as a testbed for various physical studies, exemplified in the presented measurements regarding the non-equilibrium nature of structural phase transitions in Coulomb crystals. Here, the formation of defects during the non-adiabatically driven linear to zigzag phase transition is investigated numerically and experimentally and compared to predictions of universal scaling laws.

**keywords:** ion trap, excess micromotion, optical clock, Kibble-Zurek mechanism

## Zusammenfassung

Gespeicherte atomare Ionen stellen Quantensysteme mit hoher Kontrollierbarkeit dar, welche Anwendung in einer Vielzahl von Gebieten finden: von Präzisionsspektroskopie über Quanteninformation und Quantensimulation zu Frequenzstandards. Letztere haben innerhalb der vergangenen 60 Jahre signifikante Beiträge in verschiedensten technischen Anwendungen und physikalischen Experimenten geleistet.

Innerhalb der letzten 2 Jahrzehnte, ist eine neue Generation von Frequenzstandards entwickelt worden, welche die etablierten auf atomaren Übergängen im Mikrowellenbereich basierten Systeme in Genauigkeit und Stabilität schließlich sogar übertrafen, aber noch nicht in Zuverlässigkeit. Diese auf optischen atomaren Übergängen basierten Frequenzstandards, insbesondere solche, die auf gespeicherten Ionen basieren, bieten eine unübertroffene Manipulierbarkeit der atomaren Referenz. Systeme mit einzelnen Ionen oder Zwei-Ionen Systeme erzielen höchste Genauigkeiten bei Frequenzmessungen aufgrund des hohen Grads an Isolation von der Umgebung.

Die Stabilität solcher Systeme ist allerdings limitiert aufgrund des innewohnenden niedrigen Signal-zu-Rausch-Verhältnisses und dessen Erhöhung durch eine größere Anzahl an Ionen war bislang nicht möglich ohne zunehmende systembedingte Frequenzverschiebungen aufgrund von mechanischen Toleranzen in der Fallenherstellung. Im Kontrast dazu profitieren Systeme, die auf Ensembles neutraler Atome basieren, von ihrem charakteristischen hohen Signal-zu-Rausch-Verhältnis, müssen aber mehr Aufwand gegen Störeinflüsse aus der Umgebung und damit einhergehende systematische Unsicherheiten betreiben.

Die vorliegende Arbeit versucht die Stärke beider Arten von Systemen in der Entwicklung einer skalierbaren Fallengeometrie zum Speichern von Gruppen von linearen Coulomb-Kristallen zu verbinden. Dabei sollen keine Kompromisse zwischen Signal-zu-Rausch-Verhältnis und Genauigkeit gemacht werden. Um dies zu erreichen, wurden die Einflüsse von Herstellungstoleranzen und Ungenauigkeiten beim Zusammenbau detailliert untersucht.

Als möglicher Kandidat für eine Multi-Ionen optische Uhr wird  $^{115}\text{In}^+$  vorgestellt, welches sympathisch von  $^{172}\text{Yb}^+$  gekühlt wird. Letzteres wird auch als Testsystem zur Fallencharakterisierung von Prototypen, welche in dieser Arbeit entworfen, gebaut und getestet werden, benutzt. Der hier vorgestellte experimentelle Aufbau ist optimiert für die Fallencharakterisierung und die Messung remanenter elektrischer Wechselfelder im Fallenzentrum, welche deutlich zur systematischen Unsicherheit beitragen können bei der Zielsetzung einer relativen Ungenauigkeit von  $< 10^{-18}$ .

Die Ergebnisse dieser Arbeit demonstrieren die Fähigkeit der vorgestellten Fallenstruktur, einen neuen Grad von Präzision und Kontrolle zu erlangen, welcher Voraussetzung für Uhren-Messungen, Geodäsie oder extraterrestrische Navigation ist.

Des Weiteren bietet das vorgestellte System die Möglichkeit, verschiedenste physikalische Untersuchungen durchzuführen. Dies wird beispielhaft durch Messungen auf dem Gebiet der nichtlinearen Dynamik in strukturellen Phasenübergängen in Coulomb-Kristallen gezeigt. Dabei wird die Entstehung von strukturellen Defekten während des überadiabatisch getriebenen linear zu "zigzag" Phasenübergangs numerisch und experi-

mentell untersucht und mit Vorhersagen über eine universelle Abhängigkeit verglichen.

**Schlagworte:** Ionenfalle, Mikrobewegung, Optische Atomuhr, Kibble-Zurek Mechanismus



# Contents

<b>1</b>	<b>Introduction</b>	<b>7</b>
<b>2</b>	<b>Theory</b>	<b>10</b>
2.1	$^{115}\text{In}^+$ as a suitable candidate for a multi-ion clock . . . . .	10
2.2	Theory of Paul traps . . . . .	13
2.2.1	The ideal quadrupole trap . . . . .	13
2.2.2	Excess micromotion . . . . .	15
2.2.3	Real traps . . . . .	16
2.3	Influence of Trap geometry on clock spectroscopy . . . . .	17
2.3.1	Trap dimensions and heating rates . . . . .	17
2.3.2	RF voltage configuration . . . . .	18
2.3.3	RF phase shifts and residual rf fields . . . . .	18
2.4	FEM calculations . . . . .	21
2.4.1	Method . . . . .	21
2.4.2	Influence of trap geometry on axial rf field . . . . .	22
2.4.3	Influence of machining and alignment . . . . .	24
<b>3</b>	<b>Trap development</b>	<b>27</b>
3.1	Choice of materials – requirements on ion trap for clock operation . . . .	27
3.2	Prototype trap design and calculations . . . . .	29
3.3	Trap fabrication . . . . .	36
3.4	Magnetization of trap parts . . . . .	40
<b>4</b>	<b>Experimental setup</b>	<b>42</b>
4.1	Laser system . . . . .	43
4.1.1	Level scheme of $^{172}\text{Yb}^+$ . . . . .	43
4.1.2	Lasers . . . . .	44
4.2	Laser stabilization . . . . .	47
4.3	Atomic oven design and photoionization of Yb and In . . . . .	49
4.4	Vacuum system . . . . .	51
4.5	Trap drive . . . . .	52
4.5.1	RF voltage drive . . . . .	52
4.5.2	DC voltages . . . . .	56
4.6	Detection . . . . .	58

<b>5</b>	<b>Characterization of prototype trap</b>	<b>60</b>
5.1	Loading and trapping ions . . . . .	61
5.1.1	Deterministic loading of $^{172}\text{Yb}^+$ ions . . . . .	61
5.1.2	Measured secular frequencies . . . . .	63
5.2	Photon-correlation spectroscopy . . . . .	67
5.2.1	Method . . . . .	67
5.2.2	Sensitivity of the method . . . . .	70
5.2.3	Evaluation of the rf field and resolution . . . . .	71
5.3	Micromotion in the trap . . . . .	72
5.3.1	Radial micromotion . . . . .	72
5.3.2	Axial micromotion . . . . .	74
5.3.3	Longterm analysis of micromotion compensation . . . . .	78
5.3.4	Measurement crosstalk of compensation voltages . . . . .	83
<b>6</b>	<b>Phase transitions and defects in Coulomb crystals</b>	<b>87</b>
6.1	Introduction to the field . . . . .	88
6.2	Theoretical description . . . . .	89
6.3	Simulating dynamics of trapped Coulomb crystals . . . . .	92
6.3.1	Method and kink detection . . . . .	92
6.3.2	KZM regimes . . . . .	94
6.3.3	Loss mechanisms . . . . .	95
6.4	Experimental realization . . . . .	98
6.4.1	Measurement sequence and parameters . . . . .	98
6.4.2	Controlled quench of the order parameter . . . . .	99
6.4.3	Kink detection and data analysis . . . . .	100
6.5	Results . . . . .	102
6.5.1	KZM scaling . . . . .	102
6.5.2	Kink lifetime . . . . .	104
<b>7</b>	<b>Summary and outlook</b>	<b>105</b>
<b>A</b>	<b>DC control schematic</b>	<b>109</b>
	<b>Bibliography</b>	<b>117</b>



# Chapter 1

## Introduction

This thesis consists of two thematically separated, yet fundamentally connected parts. The main focus is on the part which documents the design, assembly and characterization of a segmented linear Paul trap for precision spectroscopy of Coulomb crystals.

Due to the demonstrated high-level control and longterm stability of this trap, statistical measurements have been carried out regarding the non-equilibrium dynamics during structural phase transitions in Coulomb crystals. These will be described subsequently, exemplifying the versatility of the trap introduced in the main part.

Frequency is the measurement quantity with the highest degree of accuracy. Due to this, frequency standards are established as a tool within most fields of technology and a wide range of fundamental research areas aside from the traditional task as a time reference. Two prominent examples are the global positioning system (GPS) or experiments regarding the question if the constants in fundamental physical theories are, in fact, constant.

The constantly advancing performance of frequency standards goes hand in hand with technological progress, exemplified in the development of microwave based Cs beam clocks in the 1950s outperforming the previous systems based on mechanical oscillators in terms of accuracy within only a short period [1]. In turn, the performance of many technological applications, like the stated GPS or network synchronization, relies on the quality of the frequency reference provided by the used frequency standard.

A similar relationship exists between frequency standards and fundamental research. The most stringent tests of physical theories are obtained by doing frequency measurements and many experiments rely on stable references. One example is the determination of the fine-structure constant  $\alpha = e^2/(4\pi\epsilon_0\hbar c) \sim 1/137$  from the compared frequency measurements of an Al<sup>+</sup> and Hg<sup>+</sup> atomic clock [2]. Here, a repeated precise measurement of  $\alpha$  over about a year lead to the preliminary constraint for a possible temporal drift of the fine-structure constant of  $\dot{\alpha}/\alpha = (1.6 \pm 2.3) \times 10^{-17} \text{ a}^{-1}$ . Comparing this Al<sup>+</sup> clock to a similar system with the same clock ion species demonstrated the measurement of relativistic frequency shifts with unprecedented sensitivity [3]. In this experiment, time dilation was demonstrated in two ways. The first was to measure a change in fractional frequency difference of the two Al<sup>+</sup> clocks of  $(4.1 \pm 1.6) \times 10^{-17}$  after a change of their

relative distance in height by only 33 cm, thus illustrating the difference in the rates of two clocks experiencing unlike gravitational potential. In the same experiment time dilation due to a change in relative speed of the clock ions could be demonstrated by introducing controlled harmonic motion to one of the ions.

Atomic frequency standards based on microwave transitions play a central role in many applications due to their high degree of reliability, that concludes from the long period of continuous improvement since their advent around 1950 [4]. The first systems already exhibited relative accuracies on the order of 1 part in  $10^{10}$ . With the technique of laser cooling introduced in 1975 [5–8], not only the existing systems experienced an improvement in performance [9, 10], but also new systems became attractive in the field of precision spectroscopy. In 1981, shortly after the successful trapping of a laser cooled single ion [11], Hans Dehmelt proposed the use of an optical transition in a single trapped ion as a reference with a possible frequency resolution of 1 part in  $10^{18}$  [12].

The first optical frequency standards, however, could not utilize their full potential yet. A significant step towards the spectroscopy of narrow optical transitions was taken by stabilizing the spectroscopy laser to isolated ultra-stable optical cavities to reach unprecedented linewidths [13, 14]. With this, cooling techniques like sideband cooling enabled recoil-free spectroscopy and reduction of motion-induced relativistic frequency shifts. The femtosecond frequency comb [15] facilitates measurement of optical frequencies by transferring them to the electronically countable regime in a compact and reliable setup.

Today, optical clocks have surpassed microwave standards in terms of accuracy and stability, but yet require further improvements in terms of reliability for the use as a primary frequency standard. With a relative accuracy below  $10^{-17}$  within reach, new applications emerge for optical clocks in various fields: further improvements of tests of fundamental theories, as well as in geodesy or navigation in space are only few examples. For these applications to be realized, considerable effort has to be put in improving the accuracy down to  $10^{-18}$  or below. This can be achieved by reduction of systematic shifts with better control of the system and reduction of the measurement time by improved short-term stability in order to minimize the contributions of drifts and to increase the reliability of the system.

Today's best optical clocks in terms of accuracy are two-species ion systems [16], where the clock ion is sympathetically cooled by another ion and the detection is realized by quantum logic spectroscopy [17]. The use of single-ion clocks offers an excellent potential to reach lowest frequency inaccuracy with the trade-off of limited short-term stability due to their intrinsically low signal-to-noise ratio (SNR). One approach to improve the short-term stability of the clock measurement is to increase the spectroscopy pulse time on long-lived atomic states [16, 18]. This naturally limits the number of available clock ion candidates and places severe requirements on the clock laser stability.

Another approach is to increase the SNR with a larger number of clock ions [19, 20]. The challenge in doing this is to provide a trap that is capable of offering confinement without introducing excessive systematic frequency shifts due to residual rf fields. Linear Paul traps in principle offer an extended region, however, current limitations in accuracy are due to residual axial rf fields in such a system [16] caused by trap imperfections.

In the field of quantum information and quantum computation considerable effort has been put into the development of miniaturized scalable trap structures, optimized for fast ion transport with relevant timescales in the millisecond regime or below [21–29]. For optical clocks, the dimensions should be larger to reduce heating rates [30, 31] during measurement cycles on the scale of seconds. Together with maximal optical access and low machining and alignment tolerances, stringent conditions emerge for the trap development.

The main part of this work is dedicated to the development, assembly and characterization of a scalable linear Paul trap that can be used to operate a multi-ion optical clock with an array of linear ion chains and in doing so, offer a high level of control and lowest systematic frequency shifts of  $|\Delta\nu/\nu| \leq 1 \times 10^{-18}$  due to residual rf fields.

In Ch. 2 the atomic properties of  $^{115}\text{In}^+$  are presented to motivate its use in an optical clock with many ions and benchmarks are set in the development of a suitable trap design. Technical guidelines for the trap design are derived analytically and numerically. Chapter 3 is dedicated to the development and the assembly of a prototype trap to demonstrate the operational aspects and optimized features of the trap design that is derived in the preceding Chapter, including a detailed numerical analysis of the trap potential. The atomic test system  $^{172}\text{Yb}^+$  and experimental setup are introduced in Ch. 4, including the used lasers and the laser stabilization. Tests of the atomic ovens for both indium and ytterbium are shown and the photoionization processes are illustrated. The vacuum system, the electronics for the trap control and their calibration are presented.

The prototype trap is characterized in Ch. 5 in terms of trap parameters, residual rf electric fields and longterm stability. A second trap with similar dimensions and a different manufacturing technique is characterized as well and compared to the first trap. For the measurement of rf fields, photon-correlation spectroscopy is used. The technique is characterized and its sensitivity evaluated to investigate its ability as a tool to characterize ion traps that are used in metrological applications.

In Ch. 6 the high-level control of Coulomb crystals in the prototype trap is shown exemplified in measurements on the non-equilibrium dynamics during structural phase transitions in Coulomb crystals. The formation of defects during the non-adiabatically driven linear to zigzag transition is investigated, in particular the scaling of the rate of defects as a function of the rate at which the phase transition is driven.

A summary and outlook in Ch. 7 combines the conclusions that are derived in the preceding chapters.

# Chapter 2

## Theory

In this chapter, a motivation is given for the development of a segmented linear Paul trap, with which it is possible to perform high-precision spectroscopy on linear Coulomb crystals. First, the advantageous atomic properties and low systematic shifts of the clock candidate  $^{115}\text{In}^+$  are summarized, which set requirements for the trap design.

Second, a brief review of the theoretical framework of the Paul trap is shown to introduce the relevant parameters which are taken into account during optimization of the trap design.

Influences of the trap geometry on systematic shifts in clock spectroscopy are presented, which in turn give feedback to the trap design and provide reasons why a segmented trap structure is used. Phase shifts of the rf trapping field due to geometric and electrical imperfections are calculated and the resulting systematic frequency shifts of the clock transition are estimated.

The last section focuses on residual axial rf fields, which are negligible only in an ideal Paul trap, whereas in practise their contribution reaches an order of magnitude that puts limits on the performance of a clock measurement. Finite element method (FEM) analysis is carried out in order to study the effects of the geometry itself as well as tolerances in machining and alignment. From the calculations an optimized design is derived.

### 2.1 $^{115}\text{In}^+$ as a suitable candidate for a multi-ion clock

This section details on the work in Herschbach *et al.* [19]. The single  $^{115}\text{In}^+$  ion is a well known, previously investigated candidate for an ultra-stable and accurate optical clock [32–34]. Its narrow clock transition  $^1\text{S}_0 \leftrightarrow ^3\text{P}_0$  at 236.5 nm, with a natural linewidth of  $\Gamma = 2\pi \times 0.8 \text{ Hz}$  and electronic quadrupole moment  $\Theta = 0$ , see Fig. 2.1, makes it an interesting candidate for a scalable optical clock with many ions.

The possibility to detect the quantum information of the clock excitation directly via the  $^3\text{P}_1$  state with a natural lifetime of  $0.44 \mu\text{s}$  ( $\Gamma = 2\pi \times 360 \text{ kHz}$ ) [32] can facilitate the atomic signal read-out of a larger chain of ions, without the need for quantum logic techniques [17]. Its transition wavelength of 230.5 nm can be generated with standard diode laser technology and second harmonic generation [35]. The narrow linewidth of this

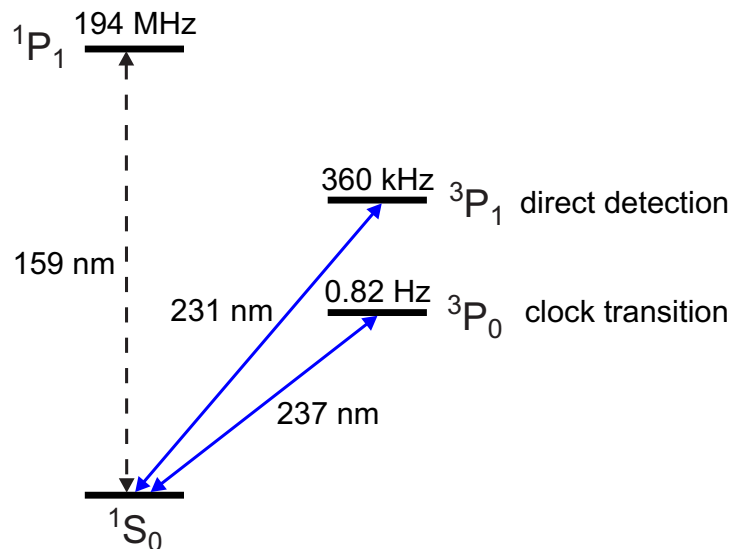


**Figure 2.1:** Schematic of the relevant energy levels of  $^{115}\text{In}^+$ . The  $^1\text{S}_0 \leftrightarrow ^3\text{P}_1$  transition allows direct detection of the ion fluorescence. The  $^1\text{S}_0 \leftrightarrow ^3\text{P}_0$  transition can be used as an optical clock transition due to its lack of quadrupole moment and its inherently low sensitivity to electric and magnetic strayfields. The  $^1\text{S}_0 \leftrightarrow ^1\text{P}_1$  transition may be used for Doppler cooling, but so far it is not accessible by current laser technology. Because the Doppler limit of  $^{172}\text{Yb}^+$  is eight times lower than for  $^{115}\text{In}^+$ , the latter can be cooled to lower temperatures sympathetically with  $^{172}\text{Yb}^+$  than directly.

transition and increased rf heating in Coulomb crystals suggests sympathetic cooling with an ion that has a stronger transition to increase the cooling efficiency. A suitable partner for this purpose is  $^{172}\text{Yb}^+$  owing to its similar mass [36], long lifetime in ion traps and easily accessible transition wavelengths.  $\text{YbH}^+$  formed in collisions with background gas can be dissociated with the Doppler cooling light [37]. In addition, the  $^{172}\text{Yb}^+$  isotope has no hyperfine structure, which simplifies cooling. Besides the enhanced cooling efficiency and control of ions, the presence of a second species allows for sympathetic cooling during the clock interrogation in case of excessive heating, additional characterization of the trap environment, such as magnetic fields and stray electric fields, and an alternative clock read-out via quantum logic for comparative studies.

Besides the absence of electronic quadrupole moment, the  $^1\text{S}_0 \leftrightarrow ^3\text{P}_0$  transition in  $^{115}\text{In}^+$  has the advantage of a very low sensitivity to environmental effects, which are summarized in Tab. 2.1.

In particular, indium profits from its heavy mass when considering relativistic frequency shifts (second-order Doppler shift) due to time dilation  $\Delta\nu_{td}/\nu = -E_{\text{kin}}/(mc^2)$ , where  $E_{\text{kin}}$  is the kinetic energy of the ion,  $m$  its rest mass,  $c$  the speed of light and  $\nu$  the frequency of the atomic transition. At the Doppler cooling limit  $T_D = 0.5 \text{ mK}$  of  $^{172}\text{Yb}^+$  this frequency shift amounts to  $\Delta\nu_{td}/\nu = -E_{\text{kin}}/(mc^2) \approx -1 \times 10^{-18}$ , where  $E_{\text{kin}} = 5/2 k_B T$  is the kinetic energy due to thermal secular and micromotion in a linear

<sup>1</sup>A heating rate of 50 phonons per second at  $\omega_m = 2\pi \times 1 \text{ MHz}$  is assumed, see text.

**Table 2.1:** Systematic relative frequency shifts in  $^{115}\text{In}^+$ . For the uncertainty of the BBR shift the theoretical uncertainty is given [19].

Type of shift	Relative shift $ \Delta\nu/\nu $ in $10^{-18}$	Uncertainty in $10^{-18}$
Thermal motion ( $T = 0.5$ mK)	1	1
Heating <sup>1</sup>	$< 0.1$	$< 0.1$
Excess micromotion	$\approx 1$	$< 1$
2nd order Zeeman	$< 0.1$	$< 0.1$
BBR at 300 K	13.6	1
DC Stark	0.3	0.3

ion trap [38]. If relative uncertainties below  $10^{-18}$  are targeted, further cooling such as sideband cooling of the  $^{172}\text{Yb}^+$  ion or direct cooling on the intercombination line of the  $^{115}\text{In}^+$  ion [39] can be implemented, where temperatures on the order of  $100\ \mu\text{K}$  are feasible.

Additional kinetic energy can be brought into the system by excess heating due to thermally activated patch potential and contaminations on the electrodes [2, 40]. Assuming an enhanced electronic field noise with a power spectral density of  $S_E = 10^{-12} (\text{V/m})^{-2} \text{Hz}^{-1}$  and an ion-electrode distance<sup>2</sup> of  $\approx 0.7$  mm, this heating leads to an average increase of motional quanta of  $d\langle n \rangle / dt = e^2 / (4m\hbar\omega_m) \times S_E(\omega_m) \approx 35 \text{ s}^{-1}$  at a secular frequency of  $\omega_m = 1$  MHz [30]. With a clock interrogation time of  $t_c = 100$  ms limited by the natural lifetime of the  $^3\text{P}_0$  state of the indium ion this amounts to 3 – 4 phonons, yielding a maximum relative frequency shift of  $-1 \times 10^{-19}$ . Commonly observed heating rates in such ion traps can be a factor 10 to 100 lower [41], giving relative frequency shifts of  $10^{-20}$  and below.

Regarding ac Stark shifts due to blackbody radiation (BBR),  $^{115}\text{In}^+$  has one of the smallest sensitivities among optical clock candidates. With a differential static polarizability of  $\Delta\alpha_0 = 5 \times 10^{-8} \text{ Hz} (\text{V/m})^{-2}$  between the  $^1\text{S}_0$  and  $^3\text{P}_0$  state [42], it is comparable to  $^{27}\text{Al}^+$  [42, 43]. Here, dynamic corrections due to the frequency distribution are neglected, as they are typically of the order of a few percent or below. At room temperature (300 K) this corresponds to a blackbody shift of the clock transition of  $1.36(10) \times 10^{-17}$ , with an uncertainty of about  $1 \times 10^{-18}$  when determining the temperature of the trap environment to  $T = (300 \pm 10)$  K.

Two major systematic frequency shifts arising from imperfections in the rf trapping potential are excess micromotion (EMM) and dc Stark shifts. If the driving radiofrequency (rf) field  $E_{\text{rf}}$  of the trap cannot be zeroed at the location of the ion, it causes a second-order Doppler shift of  $\Delta\nu_{\text{td}}/\nu = -e^2 E_{\text{rf}}^2 / (4c^2 m^2 \Omega_{\text{rf}}^2)$ , where  $e$  is the electronic charge,  $E_{\text{rf}}$  the amplitude of the electric rf field at the ion and  $\Omega_{\text{rf}}/2\pi$  the trap drive

<sup>2</sup>Dimension is taken from the prototype trap. The heating rate is a conservative estimate according to the comparison of heating rates measured in a variety of ion traps [41].

frequency [38]. This effect is the dominating uncertainty in today's best ion clocks and aggravates for a larger number of ions. In order to overcome this limitation the trap design presented in this work is optimized to have the maximum possible trapping region along the trap axis with an rf field amplitude not larger than  $115 \text{ V m}^{-1}$ , corresponding to a relative frequency shift of  $1 \times 10^{-18}$  for a trapped  $^{115}\text{In}^+$  ion at a trap drive frequency of  $\Omega_{\text{rf}} = 2\pi \times 25 \text{ MHz}$ . In addition, any residual electric field seen by the ion, will give rise to a dc Stark shift  $\nu_S$  in the clock transition. Here,  $^{115}\text{In}^+$  profits from its low static differential polarizability  $\Delta\alpha_0$  [42]. At an rf field amplitude of  $115 \text{ V m}^{-1}$  this Stark shift corresponds to  $\nu_S = \Delta\alpha_0 \langle E_{\text{rf}}^2 \rangle \approx 3 \times 10^{-19} \times \nu$ .

Last, the influence of static and dynamic magnetic fields in the ion trap are considered. The linear Zeeman shift from the  $m_F = 9/2$  to  $m_F = 7/2$  states amounts to  $6.36 \text{ kHz mT}^{-1}$  [44] and is due to hyperfine mixing of  $^3\text{P}_0$  and  $^1\text{P}_1$  states (the nuclear spin of  $^{115}\text{In}$  is  $I = 9/2$ ). It can be measured and subtracted by alternatively pumping the ion into the stretched states of the ground state with opposite magnetic moments [2, 45]. The second-order Zeeman shift is given by  $\Delta\nu = \beta \langle B^2 \rangle$ . Here, for the alkaline-earth like system  $\beta = 2\mu_B^2 / (3h^2 \Delta_{\text{FS}}) = 4.1 \text{ Hz mT}^{-2}$ , where  $\mu_B$  is the Bohr magneton and  $h$  the Planck constant. Owing to the large fine-structure splitting  $\Delta_{\text{FS}} = 3.2 \times 10^{13} \text{ Hz}$  of the excited triplet states, indium has an advantageously low second-order B-field dependency, 10000 times lower than  $^{171}\text{Yb}^+$  and 20 times lower than  $^{27}\text{Al}^+$ . Due to unbalanced currents in ion traps, alternating magnetic fields with  $B_{\text{rms}}^2 = 2.2 \times 10^{-11} \text{ T}^2$  have been observed [16]. For  $^{27}\text{Al}^+$  this leads to an ac Zeeman shift of  $\Delta\nu/\nu = 1.4 \times 10^{-18}$ . However, for the  $^{115}\text{In}^+$  ion with  $\Delta\nu/\nu = 7 \times 10^{-20}$  this effect is negligible at the level of  $10^{-18}$ .

While static and dynamic B-fields can be determined quite accurately and frequency shifts can be taken into account, for an optical clock based on many ions, requirements on the homogeneity of magnetic fields become important. With the given linear Zeeman shift, variations in the magnetic field amplitude should be less than  $16 \text{ nT}$  across the ion chain to ensure that the broadening of the atomic line is less than  $0.1 \text{ Hz}$ . Distortions of the line profile due to spatially varying systematic shifts will have to be evaluated carefully to avoid locking offsets. The fast interrogation cycle, that is possible with a multi-ion frequency standard, will be most advantageous when both stretched states are probed, in order to avoid offsets due to temporally varying magnetic fields.

The above considerations show that it should be possible to evaluate the clock frequency of a larger sample of  $^{115}\text{In}^+$  ions with a fractional frequency uncertainty of  $10^{-18}$ , assuming that a sufficiently ideal trap can be machined. This issue will be addressed in more detail in the following sections of this Chapter.

## 2.2 Theory of Paul traps

### 2.2.1 The ideal quadrupole trap

A comprehensive insight in the theoretical framework for the trapping of charged particles can be found in numerous sources in literature [46, 47]. Here, only the basic principles are illustrated to introduce the relevant equations and parameter.

In one or two dimensions a charged particle can be trapped simply by a static electric potential. In all three dimensions this is not possible according to *Earnshaws theorem*. For a potential of the form:  $\varphi(\vec{x}) = Ax^2 + By^2 + Cz^2$ , with the constants  $A, B, C \in \mathbb{R}$  the Laplace equation  $\Delta\varphi = 0$  can only be satisfied, if  $A + B + C = 0$ .

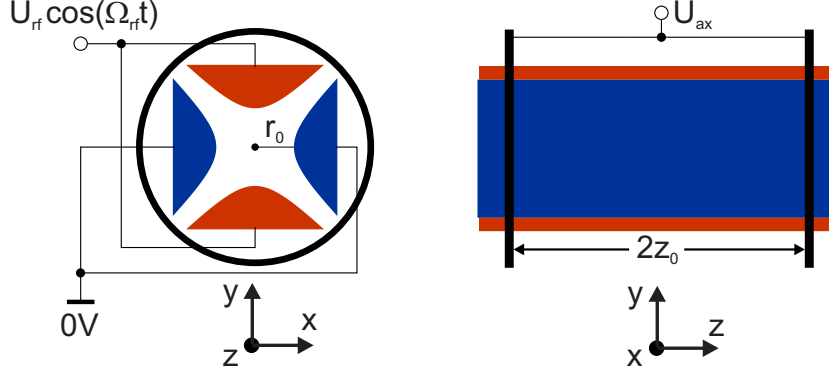


**Figure 2.2:** Schematic of a linear Paul trap with elongated hyperbolic shaped electrodes for confinement in the radial ( $xy$ ) plane with an rf potential. Additional ring shaped electrodes provide confinement in axial direction (along  $z$  axis) with a dc potential.

By introducing an oscillating potential, three dimensional confinement can be provided. Consider an ion of mass  $m$  and charge  $e$  the in a linear trap geometry with radial symmetry as shown in Fig. 2.2 with an applied potential of the form:

$$\phi(x, y, z, t) = \underbrace{\frac{U_{\text{rf}}}{2r_0^2} \cos(\Omega_{\text{rf}}t) (x^2 - y^2)}_{\phi_{\text{rf}}} + \underbrace{\frac{U_{\text{ax}}}{z_0^2 \kappa} \left[ z^2 - \frac{1}{2}(x^2 + y^2) \right]}_{\phi_{\text{ax}}}. \quad (2.1)$$

Here,  $2r_0$  is the distance between opposite radial electrodes,  $2z_0$  the distance between the two ring electrodes and  $\kappa$  a geometrical factor. For the ion the equations of motion read:

$$\frac{d^2 r_i(t)}{dt^2} = -\frac{e}{m} \frac{\partial \phi}{\partial r_i}, \quad \text{with } r_i \in \{x, y, z\} \quad (2.2)$$

In order to simplify calculations dimensionless parameters are introduced, yielding the equations of motion in the form of Mathieu equations:

$$\frac{d^2 r_i}{d\tau^2} + [a_i + 2q_i \cos(2\tau)] r_i = 0, \quad \text{with} \quad (2.3)$$

$$\frac{1}{2} a_z = -a_x = -a_y = \frac{4eU_{\text{ax}}}{m\Omega_{\text{rf}}^2 r_0^2}, \quad (2.4)$$

$$q_x = -q_y = \frac{2eU_{\text{rf}}}{m\Omega_{\text{rf}}^2 r_0^2}, \quad q_z = 0 \quad \text{and} \quad (2.5)$$

$$\tau = \frac{\Omega_{\text{rf}} t}{2}. \quad (2.6)$$



A stable solution for the equations can be found for  $|a|, |q| \ll 1$  and to first order in  $q$ :

$$r_i(t) \cong r_{0,i} \cos(\omega_i t + \varphi_i) \left[ 1 + \frac{q_i}{2} \cos(\Omega_{\text{rf}} t) \right]. \quad (2.7)$$

From this it can be seen that the ion motion consists of an oscillation (*secular motion*) at frequency  $\omega$  in a pseudo-harmonic time-independent potential:

$$\Psi(x, y, z) = \frac{m}{2} (\omega_x^2 x^2 + \omega_y^2 y^2 + \omega_z^2 z^2) \quad \text{with} \quad \omega_i \cong \frac{\Omega_{\text{rf}}}{2} \sqrt{a_i + 0.5q_i^2}, \quad (2.8)$$

with a modulation at the rf frequency  $\Omega_{\text{rf}}$  (*micromotion*).

This potential is time independent, because the ion is too heavy to follow the rapidly varying rf potential. Thus, the ion “feels” a ponderomotive force due to the electric field gradient pointing towards the center when averaged over time. The ponderomotive energy is yielded by only looking on the time dependent part of the potential  $\phi_{\text{rf}}$  and integrating Eq. 2.2 over time:

$$\frac{dr_i(t)}{dt} = \frac{e}{m} \int E_{\text{rf}}(r_i, t) dt \quad \text{with} \quad E_{\text{rf}}(r_i, t) = -\frac{\partial \phi_{\text{rf}}}{\partial r_i}, \quad (2.9)$$

$$\frac{dr_i(t)}{dt} = \frac{eE_{\text{rf}}(r_i)}{m\Omega_{\text{rf}}} \sin(\Omega_{\text{rf}} t) \quad \text{with} \quad E_{\text{rf}}(r_i) = \frac{U_{\text{rf}}}{r_0^2} r_i. \quad (2.10)$$

Averaging over an oscillation period  $T_{\text{rf}} = 2\pi/\Omega_{\text{rf}}$  then yields the ponderomotive energy  $\phi_{\text{pond}}$ :

$$\frac{m\langle \dot{r}_i^2 \rangle}{2} = \frac{e^2 |E_{\text{rf}}(r_i)|^2}{4m\Omega_{\text{rf}}^2} = \phi_{\text{pond}}. \quad (2.11)$$

### 2.2.2 Excess micromotion

In a perfect trap, without external fields the ion is in average in the center of the ponderomotive potential at the node of the rf field. With the secular motion reduced by Doppler cooling the motional amplitude of the ion is approximated with the wavepacket extension of a harmonic oscillator in the ponderomotive potential and with ion mass  $m$ , which is usually on the order of tens of nanometer. With the rf electric field experienced by the ion the micromotion is negligible compared to the residual secular motion.

In the experiment, however, strayfields can have dramatic effects on the ion motion. A dc electric strayfield shifts the average position of the ion in the trap by  $r_{\text{s},i}$ :

$$r_{\text{s},i} = \frac{e\vec{E}_s \hat{r}_i}{m\omega_i^2}, \quad \hat{r}_i = \frac{r_i}{|r_i|}. \quad (2.12)$$

The equations of motion now read:

$$\frac{d^2 r_i}{d\tau^2} + [a_i + 2q_i \cos(2\tau)] r_i = \frac{e\vec{E}_s \hat{r}_i}{m\omega_i^2}, \quad (2.13)$$

yielding the modified solution:

$$r_i(t) = [r_{s,i} + r_{0,i} \cos(\omega_i t + \varphi_i)] \left[ 1 + \frac{q_i}{2} \cos(\Omega_{\text{rf}} t) \right]. \quad (2.14)$$

Here, the amplitude of the micromotion  $r_{\text{mm},i}$  is directly proportional to the strayfield and can grow significantly:

$$r_{\text{mm},i} = \frac{1}{2} r_{s,i} q_i. \quad (2.15)$$

### 2.2.3 Real traps

For practical reasons, such as access to the ion with lasers or efficient collection of fluorescence for detection, the electrodes of an ion trap usually do not have the ideal hyperbolic shape. For example, simply four rods with a circular cross section are used or four blades facing each other [21, 38]. Nevertheless, the equations of motion can be derived in the same way as for an ideal geometry, except for a modification of the trapping potential, which will be derived in the following section.

To analyze the shape of the rf potential it is sufficient to consider the spatial part  $\phi_{\text{rf}}(x, y)$ . In the center of a trap the potential usually can be well approximated with a quadrupole. However, when analyzing the potential in more detail, it is helpful to decompose it as a series expansion of harmonic functions. Considering the axial symmetry of a linear trap geometry, as shown in Fig. 3.2, cylindrical harmonics as used in Madsen *et al.* [21] are the functions of choice, yielding the expression for the radial potential in cylindrical coordinates:

$$\begin{aligned} \phi_{\text{rf}}(\rho, \theta) = \frac{U_{\text{rf}}}{2} & \left[ \sum_{m=0}^{\infty} c_m \left( \frac{\rho}{r_0} \right)^m \cos(m(\theta - \theta_0)) \right. \\ & \left. + \sum_{n=0}^{\infty} s_n \left( \frac{\rho}{r_0} \right)^n \sin(n(\theta - \theta_0)) \right], \end{aligned} \quad (2.16)$$

Here,  $c_n$  and  $s_n$  are the expansion coefficients and  $\theta_0$  is an offset accounting for the orientation of the trap electrodes in the used coordinate system. In Fig. 2.2  $\theta_0 = 0$  with respect to the x axis.

With the coefficient  $c_2$ , which characterizes the quadrupole term of the potential, the voltage loss factor  $L \equiv c_2^{-1}$  is introduced [48]. It tells how much the voltage has to be increased for the analyzed trap compared to an ideal quadrupole in order to obtain the same secular frequency ( $L = 1$  for an ideal quadrupole trap). Using this loss factor and assuming small motional amplitudes the Mathieu equations can be rewritten for non-ideal trap geometries:

$$\frac{d^2 r_i}{d\tau^2} + [\tilde{a}_i + 2\tilde{q}_i \cos(2\tau)] r_i = 0 \quad \text{with} \quad \tilde{a}_i = \frac{a_i}{L}, \quad \tilde{q}_i = \frac{q_i}{L}. \quad (2.17)$$

The trapping of ions in a Paul trap is based on dynamic confinement, which depends on the Mathieu parameters. When choosing the right values the ion will stay in principle

infinitely long in the trap. However, higher harmonic terms of the potential lead to instabilities of the ion motion in regions, that are otherwise stable in an ideal trap [46]. This is important in particular for efficient loading of ions, since ionized particles move initially on large radii in the trap before they are cooled.

## 2.3 Influence of Trap geometry on clock spectroscopy

### 2.3.1 Trap dimensions and heating rates

During interrogation of the atomic transition in a clock measurement, usually the cooling and repump lasers are switched off in order to avoid light shifts of the measured transition frequency. Thus, the trap design has to minimize heating rates of the ions. A typical source of heating is thermal electronic noise in the trap electrodes and the trap drive electronics, which scales with the temperature of the experimental apparatus  $T_a$  and the distance  $r_0$  from the ions to the electrodes. The heating rate  $\dot{n}$  then scales as:  $\dot{n} \propto T_a r_0^{-2}$  [30]. Another source of ion heating, that has been observed but not entirely explained, scales as  $\dot{n} \propto r_0^{-4}$  [30, 31]. Possible reasons for this “anomalous heating” are fluctuating patch potentials in the electrode material, coated spots from the atomic oven or charges migrating over the surface. In Daniilidis *et al.* [31] the measured heating rates of traps from several experiments with different properties are collected and plotted against the ion-electrode distance, supporting the overall heating rate dependence with  $d^{-4}$ . Nevertheless, a scatter of the data over up to two orders of magnitude at a fixed distance points to the complexity of the heating rate of an ion trap.

According to this, general guidelines for the trap design include the use of large dimensions for the electrode to ion distance. In Sec. 2.1 a conservative estimate for the heating rate was made using a comparably large ion-electrode distance of 0.7 mm. This distance was chosen following the trend given in Daniilidis *et al.* [31] and leads to a negligible systematic shift of the clock transition for the case of a single  $^{115}\text{In}^+$  ion.

Another reason to increase the trap size is the accessibility of the trap center for the required lasers. At the same beam diameter reduced stray light of the detection laser from the electrodes improves the signal to noise ratio.

A limitation for increasing the trap dimensions is of technical nature. From Eqs. 2.8 and 2.5 the dependency of the radial secular frequency on the trap parameters can be approximated to  $\omega_{\text{rad}} \propto U_{\text{rf}} \Omega_{\text{rf}}^{-1} r_0^{-2}$ . Thus, when increasing the ion-electrode distance  $r_0$  linearly the rf voltage amplitude has to be increased quadratically in order to maintain the same secular frequency at the same drive frequency. Simultaneously the power dissipated in the trap increases quadratically with the voltage and the risk of voltage breakthroughs between the opposite rf electrodes becomes larger.

The secular frequencies, however, need to be kept at a sufficiently high value in order to allow for recoil-free spectroscopy, i.e. the Lamb-Dicke parameter<sup>3</sup> should be much smaller than unity, to prevent systematic shifts due to the first order Doppler effect.

---

<sup>3</sup>Defined as:  $\eta = kx_0$ , with the wave vector  $k$  of the spectroscopy laser and the wavepacket extension of the ion ground state  $x_0 = \sqrt{\frac{\hbar}{2m\omega}}$ , with the secular frequency  $\omega$  in the direction of  $k$ .

When scaling up the ion number, this condition is even harder to fulfill. In order to minimize excess micromotion the ions are trapped in a linear configuration by providing strong radial confinement compared to the axial confinement. Because the rf voltage is practically limited the number of ions in a linear configuration can only be increased when decreasing the axial secular frequency, which in contrast is limited by the increasing Lamb-Dicke parameter.

This leads to the ansatz of using a segmented trap, in which small chains of ions are confined and controlled in an array of independent trap segments. The smaller crystals are easier to control, e.g. micromotion compensation and nulling of magnetic fields, and systematic shifts due to residual stray electric and magnetic fields can be estimated with higher accuracy. In principle, this geometry is scalable to many segments.

### 2.3.2 RF voltage configuration

For the application of the rf voltage two configurations are possible. In the symmetric case the signal is distributed to the electrodes as  $(+U_{\text{rf}}/2, -U_{\text{rf}}/2, +U_{\text{rf}}/2, -U_{\text{rf}}/2)$ . Due to the symmetry of this configuration, no axial field component is present on the symmetry axis in the center of the trap. In the asymmetric case the signal is distributed as  $(U_{\text{rf}}, 0, U_{\text{rf}}, 0)$ , which leads to a non-vanishing axial field component for several reasons, which will be discussed in detail in the next section.

Nevertheless, the asymmetric configuration can be realized more easily due to the following reason. For micromotion compensation in each segment additional dc voltages must be applied to the trap electrodes. Doing this on an electrode that carries several hundreds of volts rf signal, requires careful impedance matching of each electrode with respect to one another in order to avoid relative phase shifts, that otherwise can lead to non-vanishing rf fields in the trapping region. The rf signal is coupled to the electrodes via capacitors, which require very low tolerances in order to avoid phase mismatch between individual electrodes. At the same time they need to be operable at high voltages, which is not easy to fulfill<sup>4</sup>.

Therefore, it is easier to couple the additional dc voltages only to rf grounded electrodes, whereas the rf signal is provided by a common rf electrode for all segments to reduce relative phase shifts between individual rf electrodes, see Fig. 2.3. To obtain full control of the radial ion position additional electrodes are placed on top of the rf grounded electrodes, which will be explained in detail in Sec. 3.2.

### 2.3.3 RF phase shifts and residual rf fields

By using two common rf electrodes instead of many segments the relative phase shifts can be reduced significantly. However, the residual phase shifts in this geometry are estimated in the following, according to the dimensions of the prototype trap introduced in Ch. 3 and admissible tolerances are given in terms of the resulting second-order Doppler

---

<sup>4</sup>For this purpose non-magnetic SMD packages with sub millimeter size and a capacitance in the nanofarad range are required. For such elements the typical tolerances for the available capacitance are on the order of a few percent at voltages of a few hundred volts.

shift (to satisfy  $|\Delta\nu/\nu| \leq 10^{-18}$  for  $^{115}\text{In}^+$  an rf field amplitude of  $E_{\text{rf}} \leq 115 \text{ V m}^{-1}$  is allowed).

First, the rf field caused by a phase shift  $\varphi_{\text{ac}}$  between the signals of the two rf electrodes is estimated. Assume the potentials  $U_{\text{rf}} \cos(\Omega_{\text{rf}}t + \frac{1}{2}\varphi_{\text{ac}})$  and  $U_{\text{rf}} \cos(\Omega_{\text{rf}}t - \frac{1}{2}\varphi_{\text{ac}})$  each on one of the rf electrodes. According to [38] the phase shift  $\varphi_{\text{ac}}$  introduces an rf field  $E_{\text{ac}}$  in the trap center:

$$E_{\text{ac}}(x, y, t) = \frac{U_{\text{rf}}\varphi_{\text{ac}}}{2r_0} \alpha \sin \Omega_{\text{rf}}t \frac{(\hat{x} + \hat{y})}{2} \quad (2.18)$$

where  $\alpha$  is a geometrical correction factor, which allows to compare the field in the trap with and electric field between two parallel plates held at  $U_{\text{rf}}$  with distance  $2r_0/\alpha$ . From the FEM calculations introduced in the following section, the field  $E_0$  in the trap center is found to be  $E_0 = U_{\text{rf}} \alpha / (2r_0) \approx 850 \text{ V m}^{-1}$  at  $U_{\text{rf}} = 1 \text{ V}$ , yielding  $\alpha \approx 1.2$  for the prototype geometry. From the condition  $E_0 \varphi_{\text{ac}} < 115 \text{ V m}^{-1}$  a maximum tolerable phase shift of  $\varphi_{\text{ac}} = 0.6 \text{ mrad}$  between the rf electrodes is obtained for  $U_{\text{rf}} = 1500 \text{ V}$  when restricting the induced fractional frequency shift to  $1 \times 10^{-18}$ . This is easily obtained by using a common rf source for both electrodes and reducing the length difference and the difference in capacitance and inductance of the wires connecting the electrodes to a minimum.

Second, the relative phase shifts  $\varphi_{\text{rf},i}$  between the individual segments  $i$  on a common rf electrode are estimated using a lumped-circuit model of the trap, see Fig. 2.3b. For the

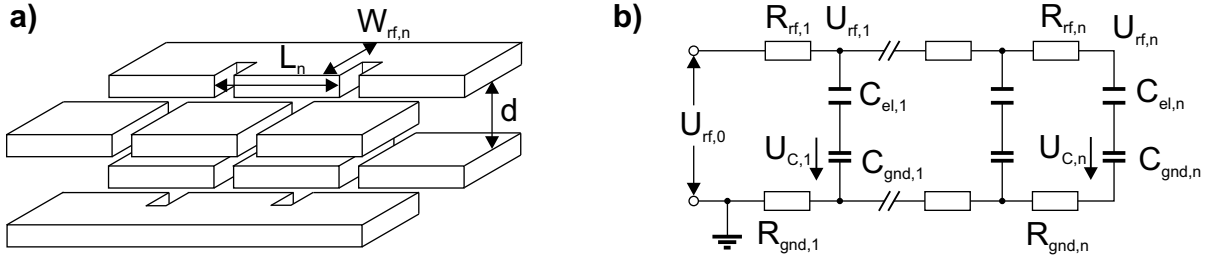


**Figure 2.3:** a) Schematic of the segmented linear Paul trap design. The rf potential is applied on an electrode rail in order to reduce relative phase shifts between the segments. For symmetry reasons slits are cut into the front edge facing the rf ground electrodes. The dimensions are  $W_{\text{rf},n} = 6 \text{ mm}$ ,  $L_n = 2.2 \text{ mm}$  and  $d = 1 \text{ mm}$ . b) Lumped-circuit model of the trap design. Included are capacitors coupling the rf ground signal to the electrodes from a common rail not shown in a). A detailed schematic of the signal connection on the prototype is given in Fig. 4.11.

electrodes a surface of thick-film gold as described in Sec. 3.3 is assumed. The dimensions of the electrodes are given in Fig. 2.3a. Here,  $R_{\text{rf},n}$  is the resistance of the rf electrode per segment with a length  $L_n$  and width  $W_{\text{rf},n}$ :

$$R_{\text{rf},n} = R_{\square} \frac{L_n}{W_{\text{rf},n}} \approx 8 \text{ m}\Omega. \quad (2.19)$$

The sheet resistance  $R_{\square} = \rho/\delta = 23 \text{ m}\Omega/\square$  is calculated from the skin depth  $\delta$  and the resistivity  $\rho$  for nickel as a conservative estimate<sup>5</sup>. The capacitance  $C_{\text{el},n}$  is the capacitance per segment length  $L_{\text{seg}}$  of the rf and the rf grounded electrode facing each other vertically and is evaluated from:

$$C_{\text{el},n} = \epsilon_0 \frac{L_n W_{\text{rf},n}}{d} \approx 0.13 \text{ pF}, \quad (2.20)$$

with the distance  $d = 1 \text{ mm}$  between the electrodes. With these values the phase shift between the rf voltages  $U_{\text{rf},i}$  can be estimated using the transfer function of a first order low-pass filter [49], which yields the expression:

$$\varphi_{\text{rf},i} = \arctan(-\Omega_{\text{rf}} R_{\text{rf},i} C_{\text{el},i}) \approx 0.2 \mu\text{rad}. \quad (2.21)$$

Therefore, the phase shifted voltages  $U_{\text{rf},i} = U_{\text{rf}} \cos(\Omega_{\text{rf}} t + \varphi_i)$  induce an axial rf field between the segments  $i$ , which can be neglected compared to the field induced by  $\varphi_{\text{ac}}$ .

For the capacitors  $C_{\text{gnd},i}$  the voltage  $U_C$  is estimated in order to evaluate a maximum tolerance of the specified capacitance. Looking at lumped circuit model of the trap in Fig. 2.3, each segment  $i$  consists of a series network of the electrode resistances  $R_{\text{rf},i}$  and  $R_{\text{gnd},i}$  and the capacitances  $C_{\text{el},i}$  and  $C_{\text{gnd},i}$  acting as voltage dividers. The impedances of the capacitances are:

$$|Z_{\text{gnd},i}| = \frac{1}{\Omega_{\text{rf}} C_{\text{gnd},i}} \approx 1.4 \Omega \quad \text{with} \quad C_{\text{gnd},i} = 4.7 \text{ nF}, \quad (2.22)$$

$$|Z_{\text{el},i}| = \frac{1}{\Omega_{\text{rf}} C_{\text{el},i}} \approx 49 \text{ k}\Omega \quad \text{with} \quad C_{\text{gnd},i} = 0.13 \text{ pF}. \quad (2.23)$$

The resistances of the electrodes are on the order of  $10 \text{ m}\Omega$  and are therefore neglected in this case. From the ratio of the impedances the voltage dropping at the capacitors can be estimated:

$$\frac{U_{\text{gnd},i}}{U_{\text{el},i}} = \frac{|Z_{\text{gnd},i}|}{|Z_{\text{el},i}|}. \quad (2.24)$$

Expressing the voltage between the electrodes as  $U_{\text{el},i} = U_{\text{rf}} - U_{\text{gnd},i}$  yields the voltage drop  $U_{\text{gnd},i}$ :

$$U_{\text{gnd},i} = U_{\text{rf}} \left( \frac{|Z_{\text{el},i}|}{|Z_{\text{gnd},i}|} + 1 \right)^{-1}, \quad (2.25)$$

$$\approx 41 \text{ mV} \quad \text{with} \quad C_{\text{gnd},i} = 4.7 \text{ nF}. \quad (2.26)$$

In practice, the capacitors are not identical, which leads to differential voltages between separate electrodes and non-vanishing rf fields. Two examples are given in Fig. 2.4.

---

<sup>5</sup>The Ni-Au coating of the prototype trap is about  $10 \mu\text{m}$  thick and contains about 70% nickel. With a skin depth  $\delta_{\text{Ni}} = \sqrt{\frac{2\rho}{\Omega_{\text{rf}}\mu}} \approx 3 \mu\text{m}$ , where  $\mu$  is the absolute permeability, the rf signal is mainly absorbed by nickel. For comparison, the skin depth of gold at this rf frequency is about  $15 \mu\text{m}$ .

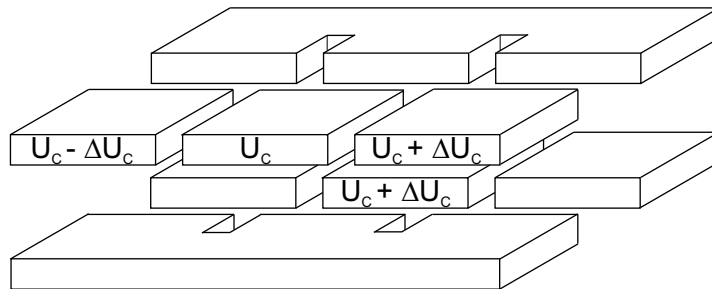


**Figure 2.4:** The same schematic as in Fig. 2.3a. Shown are examples for differential voltages  $\Delta U_C$  between the rf ground electrodes due to variations of the capacitors, that couple the rf ground signal to the electrodes. These differential voltages induce non-vanishing rf electric fields leading to excess micromotion that cannot be compensated.

For two opposing rf ground electrodes in the same segment  $i$  a radial field with an amplitude  $E_C^{(r)}$  is induced:

$$E_{C,i}^{(r)} = E_0^{(r)} \Delta U_{C,i}, \quad (2.27)$$

with  $E_0^{(r)} \approx 850 \text{ V m}^{-1}$  obtained from FEM calculations. A maximum field  $E_C^{(r)} \leq 115 \text{ V m}^{-1}$  corresponds to a differential voltage drop of  $\Delta U_C \leq 135 \text{ mV}$ .

In the case of an axial differential voltage as shown in Fig. 2.4 a field with an amplitude  $E_C^{(z)}$  is induced:

$$E_{C,i}^{(z)} = E_0^{(z)} \Delta U_{C,i}, \quad (2.28)$$

with  $E_0^{(z)} \approx 100 \text{ V m}^{-1}$ , obtained from FEM calculations. For  $E_{C,i}^{(z)} \leq 115 \text{ V m}^{-1}$  this yields a differential voltage of  $\Delta U_C \leq 115 \text{ mV}$ .

Comparing these upper boundaries with the estimated voltage drop  $U_{\text{gnd},i} \approx 41 \text{ mV}$ , it can be seen that for the given value of the capacitance  $C_{\text{gnd},i} = 4.7 \text{ nF}$  the tolerances for the capacitors (specified to 10%) are not critical in order to keep systematic frequency shifts below  $10^{-18}$  for the cases described above.

## 2.4 FEM calculations

### 2.4.1 Method

Since the trapping voltage is applied in an asymmetric configuration, an axial field component remains along the trap axis, which leads to micromotion-induced time dilation. In order to minimize the axial component and to understand how it is influenced by the trap geometry a finite element analysis has been carried out. Dimensions of the electrodes, as well as machining tolerances and alignment errors have been investigated [19].

The calculations of the rf field are reduced to an electrostatic problem by considering the field at a fixed phase. This is sufficient to determine the field evaluation within the

trap geometry and advantageous to separate these geometrical effects from dynamical changes like phase shifts in different regions of the trap as described in the preceding section. The calculations consist of finding the solution to the electrostatic Dirichlet problem, in which the electrode surfaces of the trap are the boundaries at fixed electric potentials. For this, commercially available software<sup>6</sup> is used. The software provides a discretization of the space between the electrodes (mesh) and then optimizes a system of linear equations with between  $10^6$  and  $8 \times 10^6$  degrees of freedom (mesh points). Further details on the method and used parameters are provided in [19].

The model used is similar to the one shown in Fig. 2.3a, with the exception that there is no common rf electrode. Instead, the same electrodes as for the ground potential are used in order to increase the symmetry of the model for a more efficient use of the available processor power. The electrodes each have an axial length  $L = 2$  mm, a width transverse to the trap axis  $W = 5$  mm and a thickness of 0.2 mm. The overall length of the trap, as well as the slit width between the electrodes, are varied for the calculations.

### 2.4.2 Influence of trap geometry on axial rf field

Two geometrical aspects of the segmented trap design are found to have the highest influence on the axial rf field. The first is the finite length of the trap, which leads to an increasing axial field component along the trap axis with a zero-crossing in the center of the trap. For the calculation a single segment with varied length was used in order to isolate the effect of this contribution. In Fig. 2.5 the calculated axial field is shown for different trap lengths at an rf amplitude of 1500 V. Looking at the region in which the field is smaller than  $115 \text{ V m}^{-1}$  corresponding to a fractional frequency shift of  $\leq 10^{-18}$ , the useable region is about half the overall trap length. This is accounted for in the trap design by increasing the length of the outer segments, which, because of their different geometry, cannot be used for clock spectroscopy anyway. If more trapping segments are required, the whole trap length must simply be increased. Due to this behaviour, a limitation is merely present in the overall trap size that can be realized within the experimental apparatus.

The second feature which leads to axial rf fields is the isolation gaps between the electrodes. These lead to a dispersion-shaped signal on the trap axis with the magnitude depending on the gap width, see Fig. 2.6. Here the effect of a single slit between two trap segments is shown. In order to isolate this contribution, the field obtained due to the finite trap length is subtracted, here, as well as in the following plots.

With a symmetric configuration for the rf voltage the contribution of each slit at the same axial position would cancel out. In the asymmetric configuration this happens only partially even for equal slit widths and perfectly aligned electrodes, so the slits are chosen to be as small as technically feasible.

Having more than two segments, the contributions of each slit add up independently and lead to an alternating axial rf field component, as shown in Fig. 2.7. In the center of each segment where the ions are trapped, the axial field exhibits a zero-crossing, thus

---

<sup>6</sup>COMSOL Multiphysics 3.5/3.5a



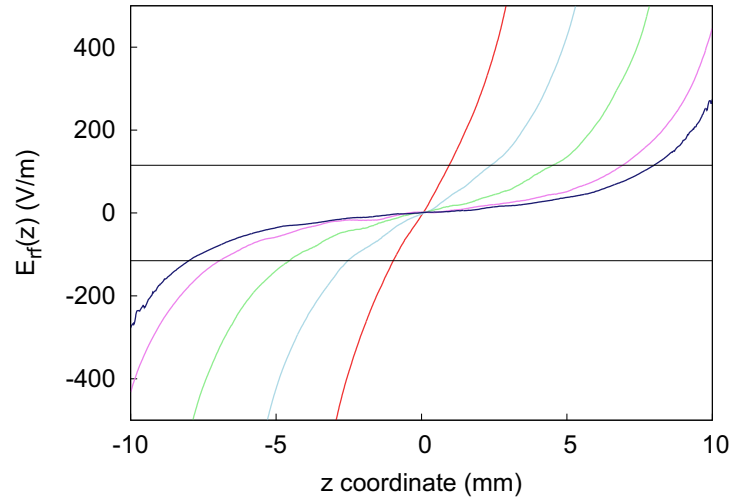


**Figure 2.5:** FEM calculations to evaluate axial rf fields due to the finite length of the trap. For this a single segment, consisting of four elongated quadrupole electrodes with varying length was used: 15 mm (red), 20 mm (light blue), 25 mm (green) and 30 mm (violet). For 30 mm length another calculation is made with additional ground electrodes at either end of the trap axis (dark blue). When cutting out the electrode structure of wafers, the end faces of the gap separating the rf and rf ground electrode arrays are metallized in order to prevent charge up of insulating surfaces in the line of sight of the ions, see Fig. 3.1. The black lines at  $\pm 115 \text{ V m}^{-1}$  indicate the amplitude at which rf induced time dilation is  $\Delta\nu/\nu = 10^{-18}$ .

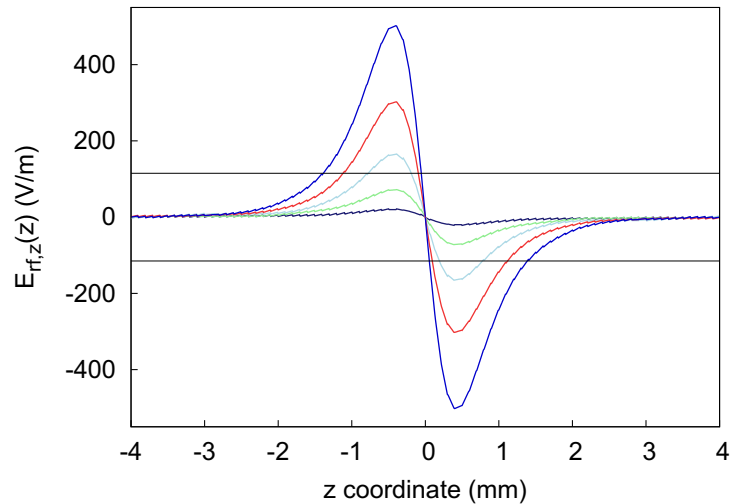


**Figure 2.6:** FEM calculations for different widths of the gaps between the trap segments:  $50 \mu\text{m}$  (dark blue),  $100 \mu\text{m}$  (green),  $150 \mu\text{m}$  (light blue),  $200 \mu\text{m}$  (red) and  $250 \mu\text{m}$  (medium blue). The black lines indicate the region of  $|\Delta\nu/\nu| \leq 10^{-18}$ .

providing a region within the trapping area with sufficiently small field amplitudes. In order to trap about ten ions in a linear configuration for clock spectroscopy, such a region is required to be on the order of  $100 \mu\text{m}$ .

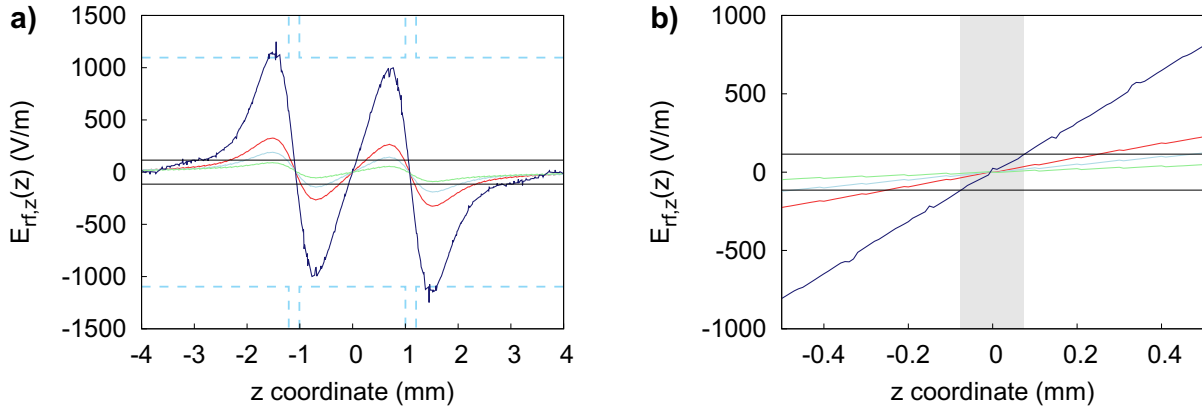


**Figure 2.7:** FEM calculations for a three segment trap geometry. The axial position of the electrodes is indicated by the light blue dashed lines. **a)** Shown is the axial rf field of two slits, calculated by adding two data sets of a single slit (Fig. 2.6) shifted in  $z$  direction with respect to each other. The slit width is varied between  $0.1 \text{ mm}$  (light green),  $0.15 \text{ mm}$  (light blue) and  $0.2 \text{ mm}$  (light red). Adding additional compensation electrodes on top of the rf ground electrodes in order to enable shifting the ions in the radial plane increases the axial field component (dark blue) by a factor of four for a slit width of  $0.2 \text{ mm}$ . **b)** Closeup of the plot in a) in the central trapping region. With the additional compensation electrodes it is possible to trap ions in a region of about  $150 \mu\text{m}$  (grey shaded area), where  $(\Delta\nu/\nu) \leq 1 \times 10^{-18}$ .

With laser cutting techniques slits of about  $50 \mu\text{m}$  or less can be realized limited mainly by the ratio of the slit width to the electrode thickness. While for machining the electrodes are preferred to be thin, the axial rf field component is proportional to the inverse of the thickness. Increasing the thickness by a factor of two reduces the axial field by about 50% [19]. Another limitation for increasing the thickness besides the machining is the decreasing detection efficiency due to the decreasing solid angle that can be captured by the detection optics.

In Fig. 2.7 the axial field in a three segment trap is shown for different slit widths. The plotted data are obtained by adding the data of two single slits, as shown in Fig. 2.6, between three electrodes of  $2 \text{ mm}$  length. They are compared with the data of a trap geometry that contains extra compensation electrodes on top of the rf ground electrodes. Although these additional layers increase the axial field about a factor of four, there is still a region of about  $150 \mu\text{m}$  with low enough time dilation due to the rf field.

### 2.4.3 Influence of machining and alignment

The requirements of the last sections are based on an ideal geometry without machining tolerances during fabrication or alignment errors during assembly, which can have signif-

icant impact on the quality of an assembled trap. Calculations were done to investigate the influence of these features and the most relevant are presented in the following.

From the machining tolerances a significant influence is due to variations of the slit width. In Fig. 2.8 the slit between two electrodes is changed with respect to the other three slits, which have all equal and fixed size. Here, the restrictions on the machining

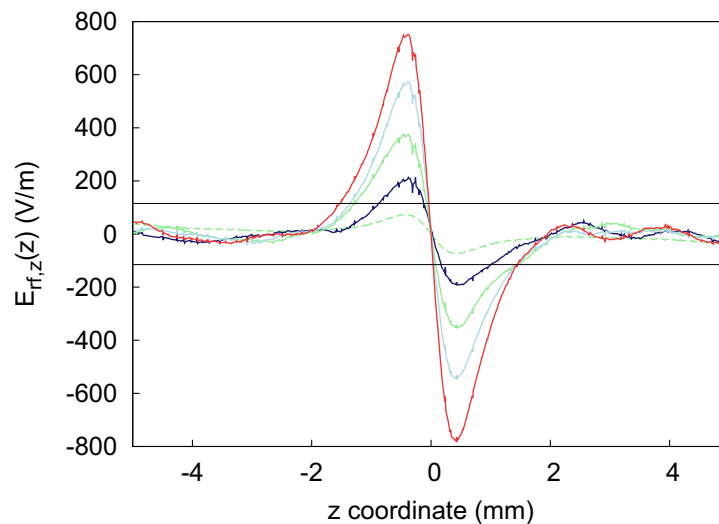


**Figure 2.8:** FEM calculations for increasing the width  $w$  of a single slit, while the other three slits have a constant width of  $w = 100 \mu\text{m}$  (dashed green line, taken from Fig. 2.7). The single slit is increased by  $\Delta w = 10 \mu\text{m}$  (dark blue),  $\Delta w = 20 \mu\text{m}$  (green),  $\Delta w = 30 \mu\text{m}$  (light blue) and  $\Delta w = 40 \mu\text{m}$  (red). To stay well within the region of  $|\Delta\nu/\nu| \leq 1 \times 10^{-18}$ , the slit width has to be machined with a tolerance of about  $5 \mu\text{m}$ .

tolerances for the slits are high. In order to stay well within the field amplitude of  $115 \text{ V m}^{-1}$ , without the extra compensation electrodes, a precision of the machining of about  $5 \mu\text{m}$  is required, see Fig. 2.8, which cannot be achieved by conventional techniques such as milling. Instead laser cutting exhibits more desirable parameters in terms of precision. Adding the extra compensation electrodes places a severe limit on the usable trapping region, which is on the order of  $150 \mu\text{m}$  for  $200 \mu\text{m}$  wide slits, no machining tolerances taken into account yet, see Fig. 2.7).

The highest sensitivity to alignment errors during assembly is found for rotational misalignment. When rotating two wafers with respect to each other about an axis normal to the wafer plane (x axis in Fig. 3.1) a homogenous axial rf field is found on the trap axis. This increases with the increasing amount of misalignment. Figure 2.9 shows the field amplitude calculated for different rotation angles.

At an rf voltage amplitude of  $1500 \text{ V}$  a maximum rotation of about  $0.15 \text{ mrad}$  is allowed in order to keep the axial field at  $115 \text{ V m}^{-1}$ .

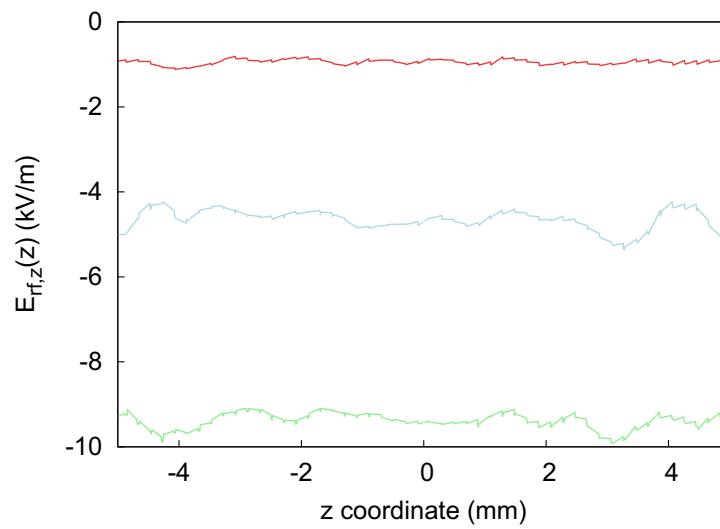


**Figure 2.9:** FEM calculations for rotational misalignment of the electrode arrays. The rotation angles are 1 mrad (red), 5 mrad (blue) and 10 mrad (green).

# Chapter 3

## Trap development

This chapter describes the different processes of the trap development from material considerations to the assembly of a fully operational prototype trap.

First, different materials are compared considering mechanical and electric properties.

Section 2 details on calculations done with the prototype geometry. The radial potentials due to the rf voltage and the dc voltages for radial asymmetry and axial confinement are analyzed and compared to an ideal quadrupole geometry. Higher order contributions to the trapping potential are evaluated to avoid dynamic trap instabilities. From the calculations the Mathieu parameters for all voltages are derived.

Focus of section 3 is the assembly of the prototype trap. The mounting of the electric filter components on the trap wafers is described, as well as the alignment and glueing procedure of the trap stack. After assembly the trap is measured again to determine misalignment during the setup.

In the last section the magnetization of the trap parts is investigated. Single components as well as the mounted trap stack are characterized in terms of residual magnetization.

### 3.1 Choice of materials – requirements on ion trap for clock operation

As shown in Ch. 2, a major challenge in the design of a multi-ion trap are residual axial rf fields due to geometrical imperfections or symmetry breaking design. This suggests a rigid trap design with laser machined electrode arrays, instead of aligning a set of individually machined electrodes manually. A way to realize this, is to use electrically insulating material as wafers with a metallic coating realizing the electrodes. This additionally opens the possibility of integrating electronic components such as noise filters directly on the wafers and therefore close to the electrodes.

For this, materials with low dissipative rf losses and high thermal conductivity are considered, in order to reduce heating of the trap. Furthermore, the distribution of dissipated thermal energy becomes more homogenous and allows for a more precise estimation of the temperature, which reduces the uncertainty of the frequency shift

due to BBR, see Sec. 2.1. Table 3.1 shows a list of possible materials<sup>1</sup> and their most important thermal and electric properties.

**Table 3.1:** Overview of thermal and electric properties of different materials considered for machining of the trap boards. The dissipation losses are specified for an rf frequency of 1 MHz.

	Rogers 4350B <sup>TM</sup>	AlN	Al <sub>2</sub> O <sub>3</sub>	sapphire	fused silica
therm. exp. [ $10^{-6} \text{ K}^{-1}$ ]	11...46	3.6...5.6	6.9...8.3	5.9...6.95	0.52
therm. cond. [ $\text{W m}^{-1} \text{ K}^{-1}$ ]	0.6	140...180	25	23...25.8	1.38
dielectric const. $\epsilon_r$	3.66	8.6	9.9	9.3...11.5	3.8
$\tan \delta$ [ $10^{-4}$ ]	31	1...10	5...10	3...8.6	0.15

Compared are aluminum ceramics with fused silica glass, sapphire and Rogers 4350B<sup>TM</sup>, a glass-reinforced thermoset laminate which is used for printed circuit boards for high-frequency electronics. All materials exhibit low outgassing rates in ultra-high vacuum environment. The ceramics and sapphire exhibit a high thermal conductivity, as well as comparably low rf losses of  $\tan \delta \leq 10^{-3}$ . Second, they provide a high mechanical stiffness, which allows for machining of wafers with thicknesses well below one millimeter without losing geometric stability.

However, a challenge is the machining of these materials. Techniques like laser cutting provide high precision, but require elaborate development of machining processes that have to be adjusted carefully to the material in use<sup>2</sup>. Sapphire is the most challenging material due to its transparency over a large wavelength range and its high refractive index. This can lead to reflections of the cutting laser inside the material and uncontrollable energy deposition, that prevents from structuring well defined geometries.

Rogers 4350B<sup>TM</sup> shows the lowest thermal conductivity and rf losses of a few  $10^{-3}$ , which is still sufficiently small in case only low rf power is required for the trap drive. In shape of thin wafers the material becomes flexible and can reduce the precision to which a trap is assembled compared to the design. The biggest advantage is, that Rogers is commercially available including mechanical structuring (milling as well as laser cutting) and metallic coating in flexible layouts.

Based on these informations, machining and coating processes for AlN are developed at PTB. In parallel, a prototype trap is set up from Rogers wafers, that are readily

<sup>1</sup>Sources of information:

Rogers 4350B<sup>TM</sup>:

<http://www.rogerscorp.com/documents/726/acm/R04000-Laminates---Data-sheet.aspx>

AlN: <http://www.anceram.de/pdf/DBALN.pdf>

Al<sub>2</sub>O<sub>3</sub>: <http://www.anceram.de/pdf/DBAL203.pdf>

sapphire and fused silica: [http://www.microcertec.com/pdf/Accumet\\$\\$\\$20substrates.pdf](http://www.microcertec.com/pdf/Accumet$$$20substrates.pdf).

<sup>2</sup>For example: Depending on the wavelength and pulse length of the used laser system, parameters like the scanning speed need to be optimized in order to minimize thermal stress in the wafer, which leads to cracking of the material. The use of inert process gases has to be optimized.

commercially available to test the trap design and the new experimental setup.

## 3.2 Prototype trap design and calculations

Based on the FEM calculations from Sec. 2.4 and the material considerations a design for a prototype trap made of Rogers has been developed with five independent segments, including a separate loading segment and a spectroscopy segment that is free from contamination from the atomic oven. A schematic drawing of the geometry is shown in figure 3.1, together with the electronic layout. The rf electrodes  $U_{\text{rf}}$  only carry the rf

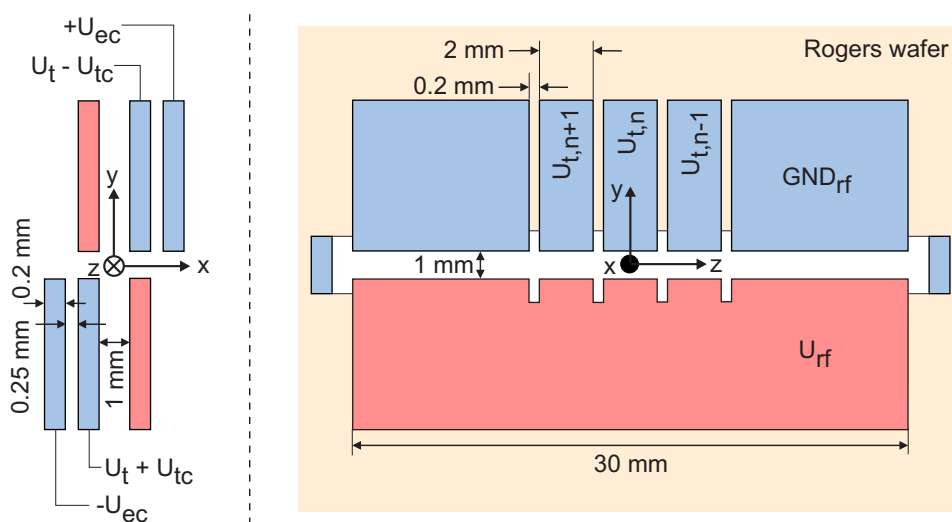


**Figure 3.1:** Trap geometry and electronic configuration. All rf ground electrode segments are dc isolated from each other. With individual voltages  $U_{\text{t},n}$  axial confinement is realized. A differential voltage  $U_{\text{tc},n}$  provides compensation fields in radially diagonal direction in each segment  $n$ . A differential voltage  $U_{\text{ec},n}$  on the outer compensation electrodes provides an independent second field vector to move the ions to any position in the  $xy$ -plane.

voltage for the radial confinement of the ions. The inner rf ground electrodes  $GND_{\text{rf}}$  opposite to the rf electrodes provide dc voltages for the axial confinement as well as for micromotion compensation, while the outer rf ground electrodes are used for micromotion compensation only.

For each wafer the ends of the cut out slit are coated and connected to  $GND_{\text{rf}}$ , to avoid charging of the surface lying in the line of sight to the trap center.

The prototype geometry is analyzed numerically to derive the relevant trap parameters. For this, the different voltages are applied to the electrodes and the electrostatic potentials are calculated using the FEM technique. To obtain the trap parameters analytical expressions derived in Sec. 2.2 are fitted to the numerical data.

The radial rf potential  $\phi_{\text{rf}}(x, y)$  is analyzed in detail. First, the electric potential is calculated for a simplified electrode scheme that consists of four rods with quadratic cross

section of  $200\ \mu\text{m}$  size, see Fig. 3.2. In a second step the electric potential is calculated for electrodes elongated in one direction to 5 mm to model the electrode shape of the prototype design. Then the extra compensation electrodes are added to model the prototype design. For all calculations  $U_{\text{rf}} = 1\ \text{V}$ . In a fourth calculation the prototype design is used and the electric potential is calculated for the dc voltage  $U_{\text{t}} = 1\ \text{V}$  that is used to introduce an asymmetry to the radial trap potential.

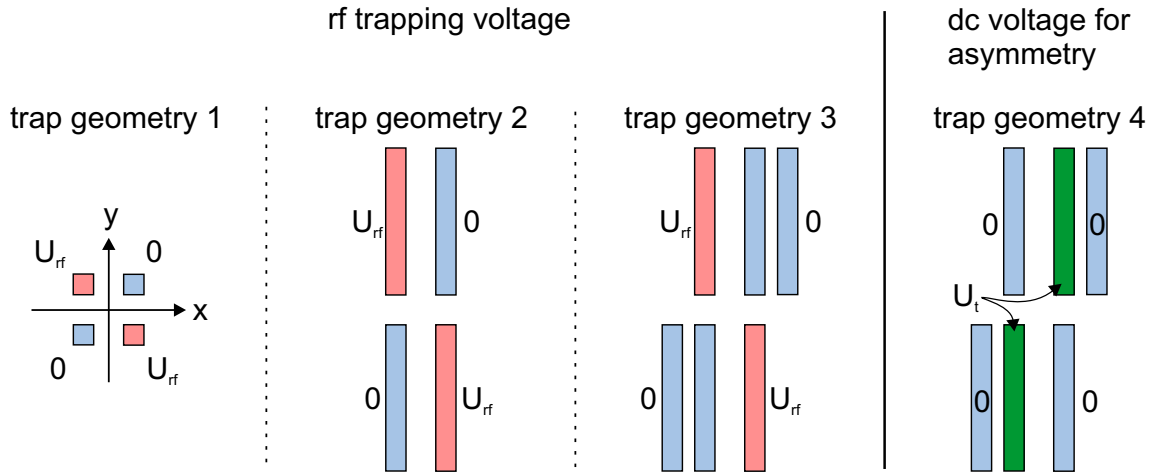


**Figure 3.2:** Trap geometries of which the electric potential is calculated for a voltage  $U_{\text{rf}} = 1\ \text{V}$  (left) and  $U_{\text{t}} = 1\ \text{V}$  (right) in order to analyze the influence of the characteristic changes in the prototype geometry compared to an ideal quadrupole trap. The trap length for all geometries is  $l_{\text{trap}} = 2\ \text{mm}$ . **Trap geometry 1:** Four rods with square shaped cross-sections of  $0.2\ \text{mm}$  size. The distance between the electrodes is  $1\ \text{mm}$  in both dimensions. **Trap geometry 2:** The electrodes are elongated in  $y$  direction to a length of  $5\ \text{mm}$ . **Trap geometry 3:** A pair of compensation electrodes as in the prototype geometry is added and the voltage is applied asymmetrically. **Trap geometry 4:** The prototype geometry is used applying  $U_{\text{t}}$  to the inner rf ground electrodes.

The potentials are fitted using Eq. 2.16 for  $0 \leq \rho \leq 0.7\ \text{mm}$ ,  $r_0 = 0.707\ \text{mm}$  and  $0^\circ \leq \theta < 360^\circ$ . The angle  $\theta$  in Eq. 2.16 is defined with respect to the  $x$  axis in Fig. 3.2 increasing for counter-clockwise rotation. The offset  $\theta_0$  added in Eq. 2.16 as a fit parameter accounts for the orientation of the potential with respect to the electrodes and defines the principle axes.

From symmetry considerations the number of expansion coefficients can be reduced significantly. In [21] it is stated that for geometries such as trap geometries 1 and 2 the potential is antisymmetric in  $x = 0$  and  $y = 0$  direction<sup>3</sup> and symmetric<sup>4</sup> in reflections about the origin and from this, the only non-zero coefficients left are:  $m = 2, 6, 10, \dots$  and  $n = 4, 8, 12, \dots$ , see Eq. 2.16. Important to note is, that this is true for a symmetric voltage configuration  $(U_{\text{rf}}, -U_{\text{rf}}, U_{\text{rf}}, -U_{\text{rf}})$ . In the case of an asymmetric configuration  $(U_{\text{rf}}, 0, U_{\text{rf}}, 0)$ , which is used in this work, additional coefficients contribute, as can be seen

<sup>3</sup>Translation from  $\mathbf{r}_1 = (\rho, \theta)$  to  $\mathbf{r}_2 = (\rho, -\theta)$  yields  $\phi(\mathbf{r}_1) = -\phi(\mathbf{r}_2)$ .

<sup>4</sup>Translation from  $\mathbf{r}_1 = (\rho, \theta)$  to  $\mathbf{r}_2 = (-\rho, \theta)$  yields  $\phi(\mathbf{r}_1) = \phi(\mathbf{r}_2)$ .



in Tab. 3.2. Here, the results of the fitting are presented and compared to each other.

In all three cases the quadrupole term is the dominant contribution to the rf potential and the loss factor (Sec. 2.2) of the prototype trap is estimated to  $L = c_2^{-1} \approx 1.3$  for determination of the Mathieu parameters  $\tilde{a}$  and  $\tilde{q}$ . The increase of  $c_2$  from geometry 1 to 2 and 3 is due to the increasing electrodes facing the trap center, hence being effectively closer to the ideal hyperbolic shape. Furthermore, the higher order terms converge faster to zero. For the highly symmetric trap geometry 1 only the  $c_m$  coefficients give relevant contributions to the potential, whereas for the geometries 2 and 3 the  $s_n$  coefficients contribute as well. The potential at the origin given by  $c_0$  is slightly reduced from the ideal value  $U_{\text{rf}}/2$  in a quadrupole trap due to the reduced screening of the electrodes, which is most apparent for geometry 1 with the smallest electrode surface.

**Table 3.2:** Overview of fitted coefficients of the multipole expansion for the trap geometries 1 to 4 defined in Fig. 3.2 with  $U_{\text{rf}} = 1 \text{ V}$  and  $U_1 = 1 \text{ V}$ . The fit errors are well below the resolution of the last digit for all parameters. Only coefficients with an absolute value of 0.01 or higher are shown. Due to the strong radial dependence of the higher order terms reliable values are only obtained when fitting over the full distance  $r_0$ . The precision of the quadrupole coefficient  $c_2$  is not affected by this.

fit parameters	trap geometry 1	trap geometry 2	trap geometry 3	trap geometry 4
$\theta_0$	$-45^\circ$	$-45^\circ$	$-47^\circ$	$50^\circ$
$c_0$	0.9393	0.9891	0.9577	0.789
$c_2$	0.7279	0.7649	0.7735	0.755
$c_4$	0.0398	–	0.0215	0.092
$c_6$	0.1228	0.0977	0.0862	0.109
$c_8$	–	–	–	0.026
$c_{10}$	0.0393	0.0343	0.0273	0.035
$c_{14}$	0.0132	0.0135	–	0.012
$s_4$	–	$-0.0282$	$-0.0263$	0.085
$s_6$	–	–	$-0.0337$	0.041
$s_{10}$	–	–	$-0.0194$	0.017

Calculations with a symmetric voltage configuration were carried out, to distinguish contributions to the electric potential from the electrode shape and the voltage configuration. The  $c_4$  term for geometry 1 only contributes in the asymmetric case and is attributed to the finite axial trap length. The calculations show, that the value of  $c_4$  grows with decreasing trap length, enhancing the finite length effect.

For trap geometry 2  $c_4$  is much smaller (less than 0.01 and not listed in Tab. 3.2). Another term,  $s_4$ , contributes more and a comparison between the two voltage configurations shows no difference for its value. This suggests, that this term accounts for the

elongated shape of the electrodes.

In geometry 3 more terms contribute due to the more complex electrode structure, in particular the  $s_6$  term accounting for the six electrodes.

In Fig. 3.3 the square of the radial electric field, which is proportional to the ponderomotive potential, is plotted in the center of the trap.

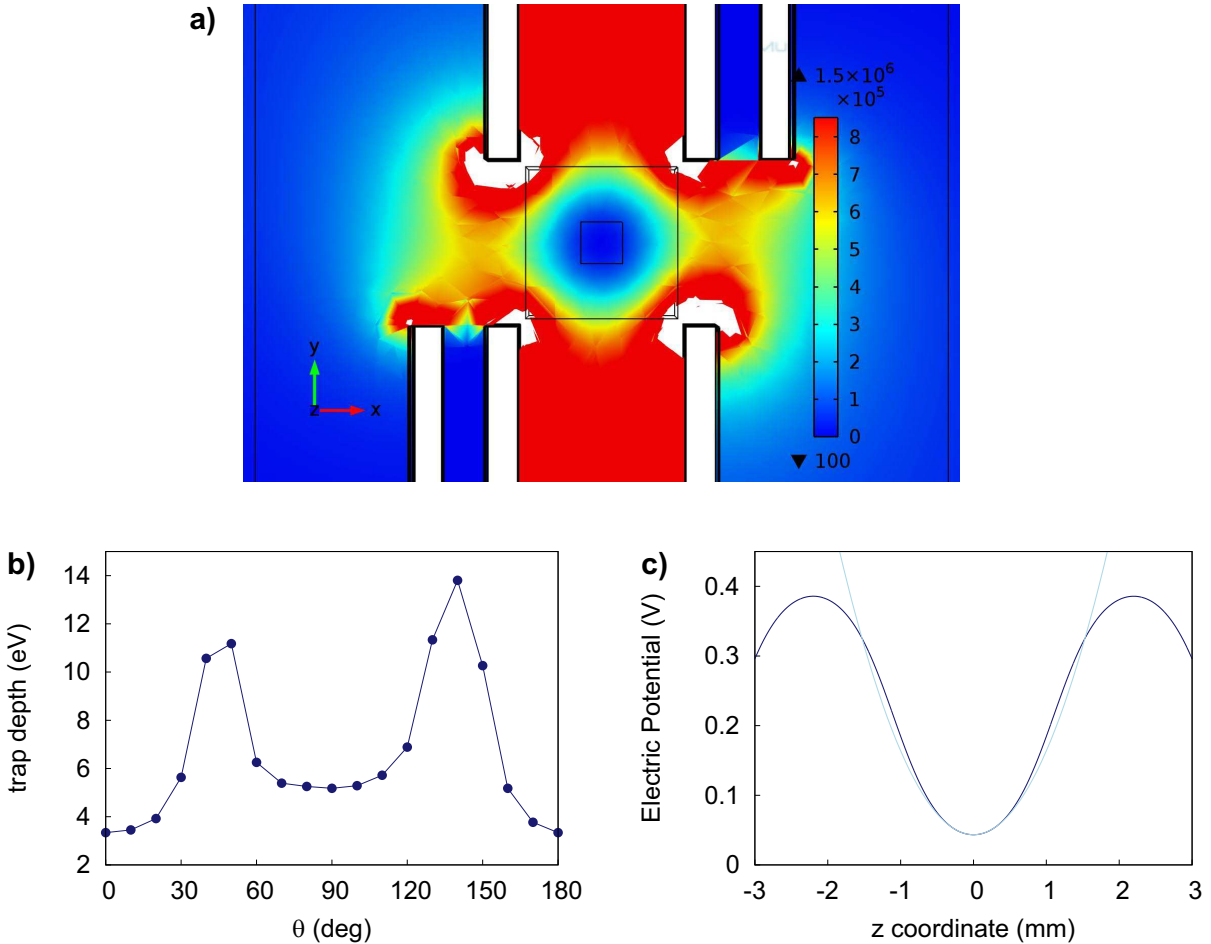


**Figure 3.3:** **a)** Plotted is the squared radial electric field  $|E_{\text{rf}}(\rho, \theta)|^2 \propto \phi_{\text{pond}}$  to indicate the shape of the ponderomotive potential in the prototype geometry for  $U_{\text{rf}} = 1$  V. In the center the dominant contribution of the quadrupole term is visible. With larger distance the higher order term increase and deform the pseudo-potential. Also visible is the local potential maximum in x direction determining the trap depth, which is plotted in **b)** as a function of  $\theta$ . Here, only a region of  $180^\circ$  is plotted, which is sufficient due to the symmetry. **c)** Here, the electric potential due to the axial voltage  $U_{\text{ax}} = 1$  V plotted. A fit (light blue) in  $-250 \mu\text{m} \leq z \leq 250 \mu\text{m}$  yields the axial confinement to a good approximation. From the potential well the axial trap  $\varphi_{\text{ax}}$  depth is estimated.

The rotation of the quadrupole term, see Tab. 3.2 does not affect the ponderomotive potential, since this is rotationally symmetric. The higher order terms, however, modulate the ponderomotive potential and lead to resonances that make the ion motion

unstable. The largest contributions to the rf potential are from the  $c_6$  and  $s_4$  coefficients. Taking into account the radial dependence as well, the contributions of these terms are about a factor of  $1 \times 10^{-3}$  or less compared to the quadrupole term<sup>5</sup> in a trap region of about  $35 \mu\text{m}$  for  $c_6$  and  $120 \mu\text{m}$  for  $s_4$ .

The modulation of the ponderomotive potential due to higher order contributions is visualized in Fig. 3.4. Here, the ponderomotive potential is plotted as a function of  $\theta$  at varying distance to the trap center. The modulation of about one percent close to the center is caused numerically by the interpolation algorithm of the FEM software used during data readout. From  $\rho \sim 100 \mu\text{m}$  on a modulation with increasing structure and strength is visible.

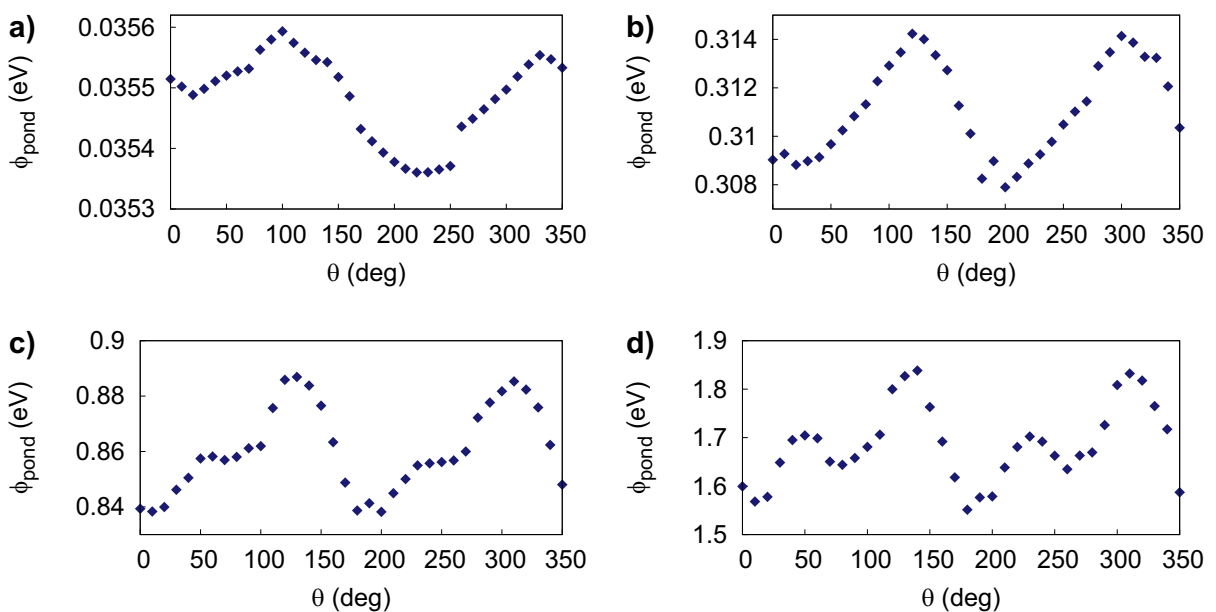


**Figure 3.4:** Ponderomotive potential as a function of  $\theta$  at various distance to the trap center. The values are from a) to d):  $50 \mu\text{m}$ ,  $150 \mu\text{m}$ ,  $250 \mu\text{m}$  and  $350 \mu\text{m}$ .

In practice, the high symmetry of the trap potential has consequences concerning efficient laser cooling. Since, there are no preferred principal axes in which the ion motion can be decomposed two orthogonal laser beams are required in order to cool all radial degrees of freedom. An alternative is the application of an asymmetry to the radial potential to define principal axes, that allow to use only one cooling laser beam with projections in both directions.

To introduce a radial asymmetry in the prototype trap the dc voltage  $U_t$  is applied on the inner rf ground electrodes, as indicated in Fig. 3.2. For an asymmetric voltage configuration the electric potential has been calculated and fitted at  $U_t = 1 \text{ V}$ , analogue to the rf potential, and the expansion coefficients are presented in Tab. 3.2.

<sup>5</sup>Calculated is the ratio of the higher order terms to the quadrupole term:  $\frac{\phi_4}{\phi_2} \leq \frac{s_4(\rho/r_0)^4}{c_2(\rho/r_0)^2} = 10^{-3}$  and  $\frac{\phi_6}{\phi_2} \leq \frac{c_6(\rho/r_0)^6}{c_2(\rho/r_0)^2} = 10^{-3}$ . From this the radius is calculated within which the ratio of the contributions is smaller than the given value.

Here, the geometry is less symmetric than in the case of the rf voltage, which is clearly visible in the larger number of expansion coefficients. Due to the higher screening of the electrodes at potential  $U_t$  by the extra compensation electrodes on potential zero the potential of the saddle point is clearly reduced with  $c_0 \approx 0.79$  compared to trap geometries 1 to 3.

The axis in the direction of the potential maxima is rotated by an angle of  $\theta_t \approx 50^\circ$  with respect to the x axis, from which the principal trap axes 1 and 2 may be defined at angles  $\theta_1 = 50^\circ$  and  $\theta_2 = 140^\circ$  for application of  $U_t$ . Due to the asymmetric voltage configuration the radial Mathieu parameters due to  $U_t$  cannot be calculated with the loss factor. Instead, they can be deduced by directly fitting quadratic functions to the potential close to the trap center in the direction of the principal axes. Doing so for  $0 \leq \rho \leq 50 \mu\text{m}$  yields curvatures of  $8.14 \times 10^5 \text{ V m}^{-1} U_t^{-1}$  and  $-6.92 \times 10^5 \text{ V m}^{-1} U_t^{-1}$  for  $50^\circ$  and  $140^\circ$ . The fitted curvature as a function of  $\theta$  is plotted in Fig. 3.5. The corresponding Mathieu parameters, which contribute to the radial secular frequencies, are shown in Tab. 3.3.

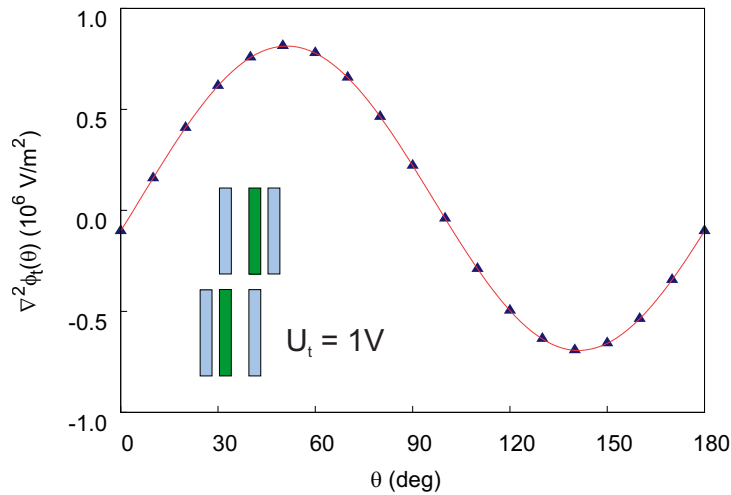


**Figure 3.5:** Fitted curvature of the electric potential  $\nabla^2\phi_t(\theta)$  due to  $U_t = 1 \text{ V}$  as a function of  $\theta$ . The principal trap axes are given by the maximum and minimum of this function, which is at about  $\theta_1 \approx 50^\circ$  and  $\theta_2 \approx 140^\circ$ . The fitted sine function (red line) indicates the quadrupole shape of the potential.

For a good estimate of the radial secular frequencies, the radial contribution of the potential  $\phi_{\text{ax}}$  (see Eq. 2.1), which provides axial confinement in the first place, cannot be neglected. For this, FEM calculations are done using the prototype geometry with application of  $U_{\text{ax}} = 1 \text{ V}$  to the rf ground electrodes of the segments adjacent to the central segment. A quadratic fit to the data in the direction of the principal axes yields the curvatures  $-5.58 \times 10^4 \text{ V m}^{-1} U_{\text{ax}}^{-1}$  and  $-6.28 \times 10^4 \text{ V m}^{-1} U_{\text{ax}}^{-1}$ . The corresponding Mathieu parameters are shown in Tab. 3.3.

With the derived mathieu parameters the radial secular frequencies  $\omega_{\text{rad},i}$  can be

calculated including all contributions from the rf voltage and dc voltages:

$$\omega_{\text{rad},i} = \frac{\Omega_{\text{rf}}}{2} \sqrt{\tilde{a}_{\text{ax},i}(U_{\text{ax}}) + \tilde{a}_{\text{t},i}(U_{\text{t}}) + 0.5 \tilde{q}_i^2(U_{\text{rf}})}, \quad \text{with } i = 1, 2. \quad (3.1)$$

The axial confinement is given by the potential due to  $U_{\text{ax}}$  with a fitted curvature of  $1.192 \times 10^5 \text{ V m}^{-2}$  for  $U_{\text{ax}} = 1 \text{ V}$ , see Fig. 3.3, which results in an axial trap frequency of  $58 \text{ kHz } U_{\text{ax}}^{-1/2}$ .

The dc voltage  $U_{\text{t}}$ , that changes the asymmetry of the radial potential leads to a repulsive potential in axial direction which amounts to a curvature of  $-1.213 \times 10^5 \text{ V m}^{-2}$  for  $U_{\text{t}} = 1 \text{ V}$ . The axial secular frequency is then calculated with the corresponding mathieu parameters (see Tab. 3.3):

$$\omega_{\text{ax}} = \frac{\Omega_{\text{rf}}}{2} \sqrt{\tilde{a}_{\text{ax}}(U_{\text{ax}}) + \tilde{a}_{\text{t}}(U_{\text{t}})}. \quad (3.2)$$

Looking for the maximum ponderomotive potential as a function of  $\theta$  the radial trap depth has been estimated. Figure 3.3a shows the ponderomotive potential with a minimum value in x direction of about 3.3 eV for an rf voltage of  $U_{\text{rf}} = 1 \text{ kV}$ .

The axial trap depth is estimated from the potential well introduced by the axial trap voltage to about 0.35 eV at  $U_{\text{ax}} = 1 \text{ V}$ , see Fig. 3.3b.

To summarize the contribution of the rf voltages and dc voltages to the secular frequencies, the corresponding mathieu parameters are presented in Tab. 3.3, normalized to applied voltages of 1 V. Here, the parameters are given in the directions x and y as well, as they are frame of reference for the trap characterization in terms of the rf field introduced in Sec. 5.3.

**Table 3.3:** List of calculated Mathieu parameters in direction of the radial principal axes, as well as the geometric axes defined in Fig. 3.1. All parameters are normalized to an applied voltage of 1 V. A comparison with the parameters measured in the prototype trap is presented in Tabs. 5.1 and 5.2.

axis	x	y	$\theta_1$	$\theta_2$	z
$\tilde{q}$	$6.69 \times 10^{-5}$	$-6.69 \times 10^{-5}$	$6.68 \times 10^{-5}$	$-6.69 \times 10^{-5}$	$\approx 10^{-3} q_{\text{rad}}$
$\tilde{a}_{\text{t}}$	$-1.76 \times 10^{-5}$	$3.82 \times 10^{-5}$	$1.41 \times 10^{-4}$	$-1.19 \times 10^{-4}$	$-2.09 \times 10^{-5}$
$\tilde{a}_{\text{ax}}$	$-1.07 \times 10^{-5}$	$-9.0 \times 10^{-6}$	$-9.64 \times 10^{-6}$	$-1.08 \times 10^{-5}$	$2.05 \times 10^{-5}$

Table 3.4 shows the dc voltages that can be applied, together with their resolution and the corresponding dc electric field calculated at the position of the ion.

**Table 3.4:** DC voltages for radial trap asymmetry ( $U_t$ ) and micromotion compensation ( $U_{tc}$  and  $U_{ec}$ ). The corresponding maximum electric field at the position of the ions and its resolution is given along the specified trap axis.

	trap axis	$\Delta U_{dc}$	$U_{dc,range}$	$\Delta E_{dc}$	$E_{dc,range}$
$U_{tc}$	x	0.6 mV	2.5 V	0.32 V/m	1325 V/m
	y			0.40 V/m	1650 V/m
$U_{ec}$	x	2.9 mV	$\pm 12$ V	0.45 V/m	1860 V/m
	y			0.05 V/m	204 V/m
$U_t$	z	2.9 mV	$\pm 12$ V	0.30 V/m	612 V/m

### 3.3 Trap fabrication

To test the trap design introduced and optimized in the preceding sections a prototype is built based on Rogers 4350B wafers. For this, two sets of wafers were machined one by laser cutting and the other by milling, both with a size of  $50 \text{ mm} \times 50 \text{ mm}$ . The thickness of the laser cut boards is  $200 \mu\text{m}$  and  $500 \mu\text{m}$  for the milled boards. The electrode design for both sets is according to Fig. 3.1 with the exception of the size of the gaps between the electrodes. In the case of the laser cut electrodes the gap size is about  $220 \mu\text{m}$  and about  $340 \mu\text{m}$  for the milled wafers.

The electrode surface consists of a  $35 \mu\text{m}$  thick copper conductive layer and a thick-film gold layer on top. The gold layer has a thickness between  $0.3 \mu\text{m}$  and  $3 \mu\text{m}$  and is on top of a  $0.7 \mu\text{m}$  to  $7 \mu\text{m}$  thick nickel layer used as adhesion promoter.

In Fig. 3.6 a closeup on the electrodes of two trap boards are shown, one of which is laser cut and the other is milled. The segment length, slit width and gap between the electrode array were measured with a calibrated microscope<sup>6</sup>. Visible is the difference between the two machining techniques. The corners of the milled electrodes are less defined and give rise to a higher uncertainty in the slit width, which varies in the measured sample of about  $40 \mu\text{m}$ , compared to a scatter of  $20 \mu\text{m}$  for the laser machined sample. Furthermore, the edges are rippled on the front side, possibly leading to distortions of the trapping potential. The laser cut structures have a higher precision with a lower uncertainty in the corners. Here a difference in quality is visible between the separated ground electrodes of the front and back side (left and right in Fig. 3.6). Due to the higher quality of the edges and corners machined by both techniques on the back side of the wafers, the design is adjusted, such that the back side of the wafers is facing the ions.

The trap consists of a stack of four wafers that carry the electrodes and are glued on a  $1.5 \text{ mm}$  thick carrier board, which provides mechanical stability and the electrical connections to the trap, see figure 3.7.

Two identical boards (1), one of which is rotated by  $180^\circ$  around the trap axis relative

<sup>6</sup>Courtesy: A. Ruhz, Dep. 5, PTB

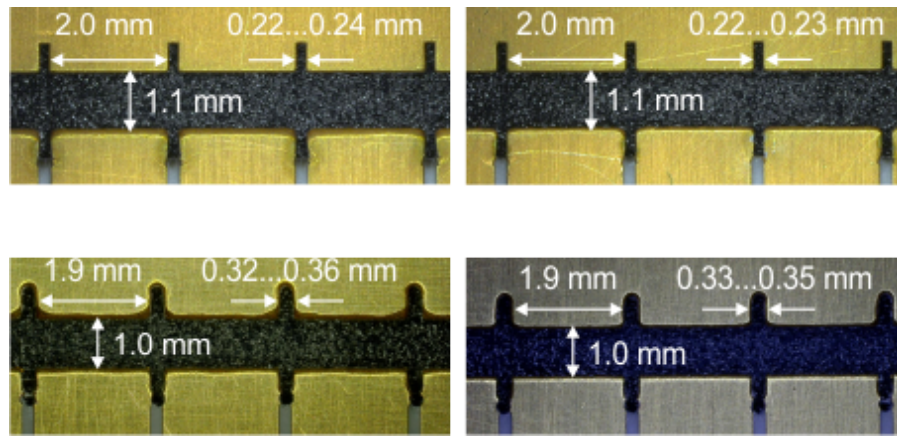


**Figure 3.6:** Closeup on the electrode region of the machined Rogers wafers. **Top:** A trap board ((1) see Fig. 3.7) with laser cut electrodes on front and back side (from left to right). **Bottom:** A trap board with milled electrodes on front and back side (left to right). The back sides face the ions in the assembled trap stack due to the higher machining quality, indicated by the measured distances.

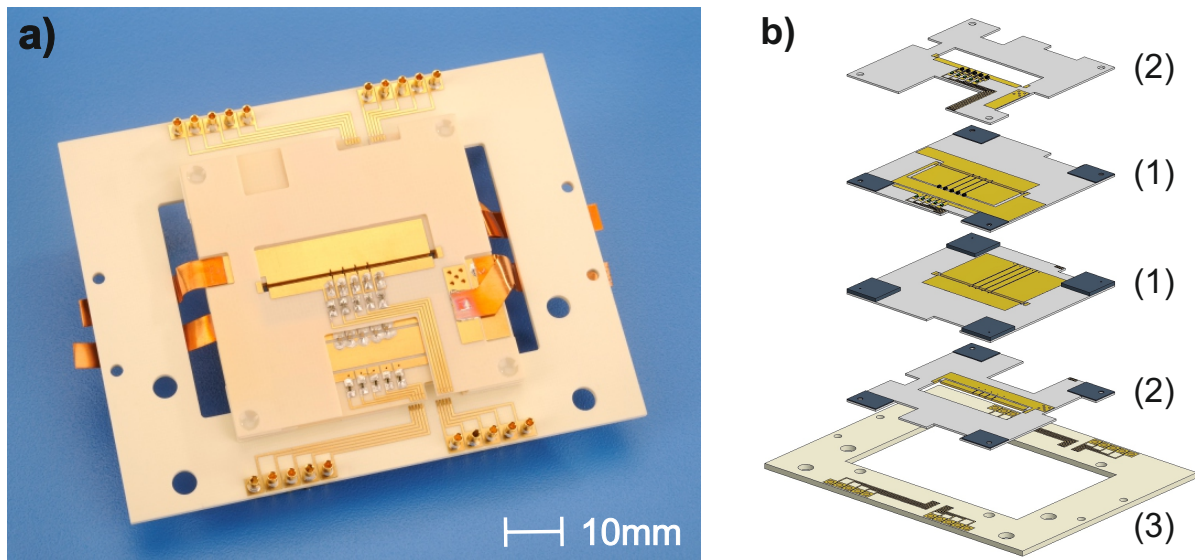


**Figure 3.7:** a) Photograph of the assembled trap stack with on-board filter electronics, connector pins for dc voltages on the carrier board and rf feed copper strips. b) Scheme of the trap assembly with two trap (1) and two compensation (2) boards with spacers (dark grey) on the corners to provide optical access for the laser beams.

to the other, form the quadrupole trap. They are separated by four 1 mm thick spacers placed in the corners. An additional board (2) is attached on top of each of the trap boards, with spacers of 0.25 mm thickness. With the spacers in the corners there is various access for laser beams to the trapping region. The carrier board provides gold pins for the dc voltage connections and a mount for the rf connection. The rf lead is a 0.1 mm thick, oxygen-free copper foil cut into 5 mm wide stripes of equal length to avoid phase shifts on the rf electrodes.

To prevent coupling of rf power into the dc voltage sources as well as coupling of high-frequency noise onto the trap electrodes, low-pass filters are soldered directly on the trap boards close to the electrodes. Resistors<sup>7</sup> with  $R = 300 \text{ k}\Omega$  and capacitors<sup>8</sup> with  $C = 4.7 \text{ nF}$  are connected as a first order low-pass with a cutoff-frequency of  $\nu_{\text{cutoff}} = 113 \text{ Hz}$ . The dc connections from the individual trap boards to the carrier boards are provided by bonding gold wires.

The assembly of both traps is done in four steps. First, the SMD parts and rf leads are soldered with vacuum compatible solder<sup>9</sup> manually. A solder iron with an SMD suitable tip<sup>10</sup> is used in connection with an infrared heating plate, which is held at a temperature between 150 °C and 180 °C, to compensate thermal losses of the conductive layers and the copper foil. The temperature of the iron is limited to 275 °C to protect the terminations of the SMD parts. The resistors have shown to be more sensitive than the capacitors and heating times of several seconds lead to destruction of the terminations.

For the copper foil stripes a bigger tip is used to provide enough heating power at the soldered spot. The SMD parts need to be fixed with a tweezer when soldered, because the surface tension of the liquified solder in connection with the low weight of the parts leads to standing up of the parts when melting the solder. Remaining flux is cleaned, with propanole and acetone.

In the second step, the wafers are aligned and glued together. The alignment of the trap boards is done under a microscope<sup>11</sup>, that has two translation stages with a scale of 1  $\mu\text{m}$  and a rotation stage with a scale of 10", which corresponds to 0.05 mrad. After aligning one board with the moving stages to a cross hairs the focus of the image is changed to the other board and the alignment repeated, with the first board being fixed on the table.

After alignment the wafers are glued together with a vacuum compatible glue<sup>12</sup>, that can be cured either thermally or by UV-light. This has the advantage of glueing the wafers one after another with a UV lamp, instead of having to move the whole stack to bring it from the microscope to the oven and risk misalignment. The glue is applied with a thin and elastic copper wire in order to avoid misalignment of the loose wafer, which is additionally fixed by putting some weight on top. Another reason to do this is to avoid creeping of glue between the wafers and therefore causing misalignment. The

---

<sup>7</sup>company: Barry industries, part number: RP0402BA-3003 JN-91

<sup>8</sup> $C = 4.7 \text{ nF}$ , company: Novacap, part number: 0402 C472 J500 PH-HB

<sup>9</sup>Kester: 80Sn19Ag1Cu

<sup>10</sup>iron: Weller, 80 W heating power, tip: chisel with (0.15 × 0.4) mm

<sup>11</sup>UWM, company: Leitz. Designed for precise characterization of mechanical parts.

<sup>12</sup>Optocast 3410 Gen2, see <http://outgassing.nasa.gov>



glue is cured with a broadband UV lamp<sup>13</sup> with 1 W of optical power held at a distance of about two centimeters above the glue for 200 s.

Figure 3.8 shows, in which order the trap boards are glued. In the beginning the

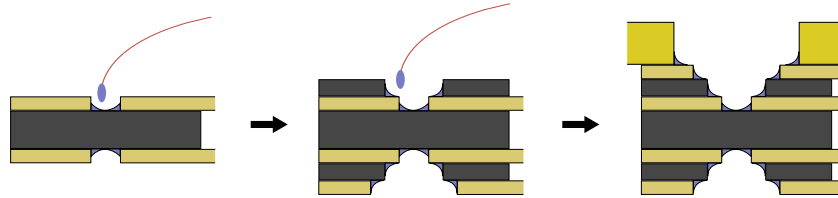


**Figure 3.8:** Scheme of the glueing of the trap stack. Starting from the thick spacers in the middle, first the trap boards are aligned and glued, followed by the thin spacers and the compensation boards. Finally, the stack is glued to the carrierboard. The glue is applied with a thin copper wire with high flexibility in order not to push the wafers after the alignment procedure.

thick spacers are glued to one trap board and stacked with the other trap board to align and glue them, as well. After fixing the thin spacers to the trap boards, the compensation boards are aligned and glue one after another. Finally, the stack is glued to the carrierboard. To make sure, that all glue is cured to avoid outgassing in the vacuum chamber, the trap is put in an oven and baked at 130 °C for half an hour.

After glueing the parts together the complete stack is inspected under the microscope again, to look for misalignment during the thermal cure. Looking from the top onto the stack only partly allows evaluation of the wafer positions relative to each other. In axial direction the upper compensation board covers the electrodes of the upper trap boards, as well as the lower trap board is covered on both sides by the upper trap and compensation board together. To investigate a rotational misalignment of the trap boards the stack is tilted a bit parallel to the trap axis. Like this the edges of both the upper rf electrodes and the rf ground electrodes below are visible. By aligning the cross hairs to both electrode arrays one after another the rotation is measured to be as big as the resolution of the rotation stage of 0.05 mrad or below. The relative axial position of the trap boards was evaluated by looking at the short edges within the electrode slits. Like this a displacement between the upper and lower trap board of about 20  $\mu\text{m}$  was observed.

In order to avoid mechanical stress on the wafers the dc connections are provided by bonding thin wires to the carrier board, to which the wires are plugged, that connect the trap with the dc feedthrough of the vacuum chamber. Gold wires with 30  $\mu\text{m}$  diameter are used for ball bonding. Because the height difference of the top compensation board to the carrier board cannot be taken by the bond device, a lifting platform was constructed to compensate for this. For an optimized bonding result, the trap is mounted on a heating device controlled by the bond machine and heated to 80 °C. Since the heat conductivity of Rogers is very low, the heating is inefficient and the wedges do not provide sufficient

<sup>13</sup>company: Dr. Hönle, model: Blue Point. Power: 1.5 W for (290...550) nm.

connectivity, which is why the bond wires are fixed at the end with a second ball.

In the last step gold pins are soldered to the carrier board. Kapton<sup>®</sup> wires plugged to the pins provide connection to the dc voltage feedthrough.

### 3.4 Magnetization of trap parts

The magnetization has been measured for each of the trap parts separately, as well as for the assembled trap stack, in order to investigate the magnetic properties of the materials. For this, the measured sample and the field probe are put in a box made of  $\mu$ -metal<sup>®</sup> to reduce background fields. The probe is fixed to a bar, that can reproducibly be translated with a precision of about half a millimeter. The measurement is carried out by shifting the probe across the sample and to look at different field components, either the probe is rotated on its mount, or the sample is rotated on the table relative to the mount.

Since the samples have to be exchanged or their position needs to be changed, the box has to be opened and closed several times between the measurements. It is observed, that this leads to scatter of the measured field. To estimate the repeatability of the measured field, the empty box is repeatedly opened and closed and the field inside the box measured for a fixed probe position. For this configuration a repeatability of the measured field of  $\sigma_B = 25$  nT is obtained. The probe used is a fluxgate<sup>14</sup> with a sensitivity of 10 nT. Another reference measurement has been carried out in order to obtain the magnetic field along the scan axis of the probe without a sample, see Fig. 3.9.

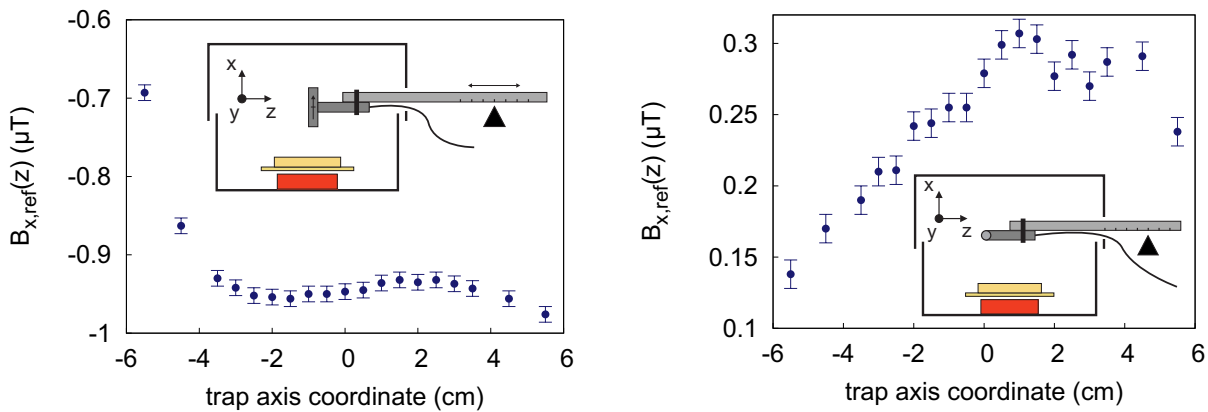


**Figure 3.9:** Reference measurement of B-field in the box without a sample. This background field is subtracted from every measurement with a sample in order to improve the precision. The errorbars show the resolution of the probe of 10 nT.

The probe is rotated such, that the vertical and the horizontal field component transverse to the scan direction can be measured. To measure the second horizontal field component, the investigated sample is rotated relative to the probe by  $90^\circ$  around the

<sup>14</sup>type: MAG02

x axis, see Fig. 3.9. The used coordinate system is the same as used for the trap, with the x axis pointing in the vertical direction in the lab frame.

First, the magnetization of the different parts, of which the trap is built of, was measured. The SMD parts show no measurable effect, as well as surprisingly the trap boards, despite a considerable part of the metal coating consists of nickel. As the boards stick to a strong permanent magnet while lifting it, so the conclusion of the measurement is, that the magnetization of the Rogers boards is less than 25 nT, most likely negligible for clock operation.

The gold pins used as dc connectors show a magnetization of  $B_x = 1.1 \mu\text{T}$  and  $B_y = 0.5 \mu\text{T}$  for a probe distance to the sample of 2.5 mm and 7 mm respectively.

Based on this result, the magnetization was measured with a complete trap stack to make a conservative estimate of the field at the trap center. The probe was scanned across the trap and all three field components have been measured. The probe distance to the trap was 3.5 mm for the vertical field component and 8 mm for the horizontal components. The results are shown in figure 3.10.

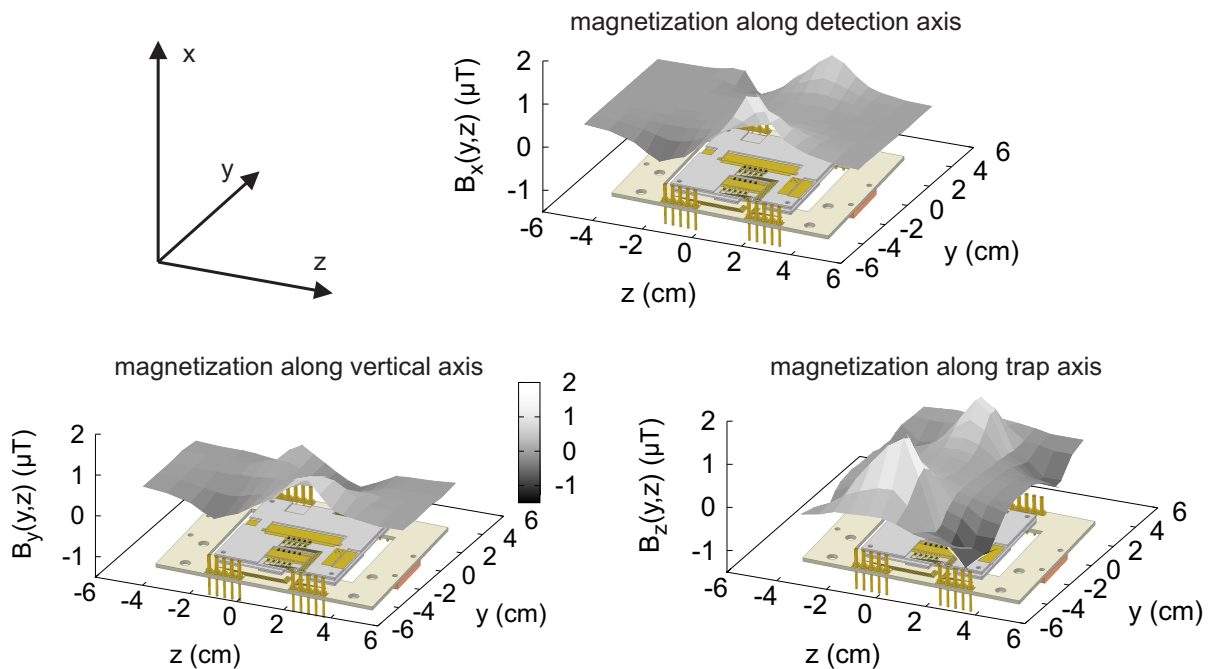


**Figure 3.10:** Measurement of magnetization of the milled Rogers trap. Shown are the three components of the B-field measured by scanning the probe above the trap.

Above the trap axis the maximal field is  $\vec{B} = (0.4, 0.3, 0.5) \mu\text{T}$ . Since the probe can only be scanned above the trap, this measurement only can give a rough estimation on the residual magnetic field in the trap center due to the pins.

# Chapter 4

## Experimental setup

Within this work, the experimental apparatus was set up, that allows to test different trap designs. This chapter details on the individual steps. A schematic overview of the vacuum chamber and the imaging system is given in Fig. 4.1, including the atomic ovens and the ion trap.

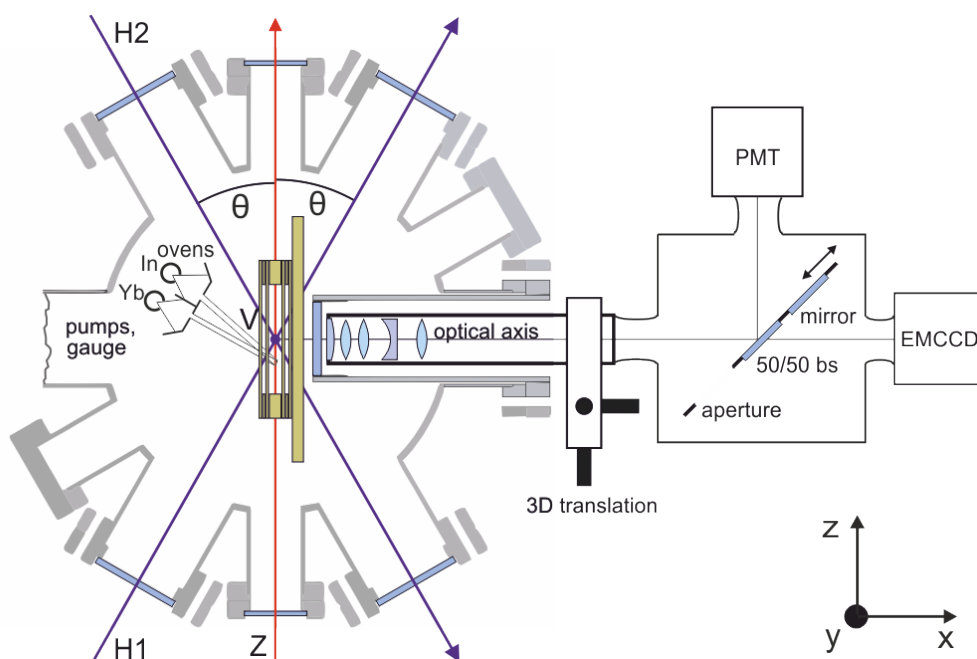


**Figure 4.1:** Schematic drawing of the vacuum chamber including the ion trap, atomic ovens for ytterbium and indium and the detection optics. The laser beams are indicated: Cooling and detection in three dimensions H1,H2 and V, repump lasers along the trap axis Z and photoionization orthogonal to the atomic beams in V (perpendicular to the paper plane). An aperture with  $\approx 1$  mm wide slits protects the trap from atomic contamination outside of the loading segment. The detection is done either with a photomultiplier tube (PMT) or an electron-multiplying charge-coupled device (EMCCD) camera or in a combination of both devices.

First, a short review of the atomic structure of the test system  $^{172}\text{Yb}^+$  is given to introduce the relevant transitions. This is followed by a description of the lasers used to drive transitions for Doppler cooling, spectroscopy and repumping of metastable states, as well as photoionization.

Second, the methods for photoionization of ytterbium and indium, as well as the design of the atomic ovens are explained. The performance of the ovens is demonstrated by frequency scans of the ionization lasers over the atomic resonances used for photoionization.

The vacuum system containing the ion trap and the ovens is introduced and the electrical and mechanical components are explained.

The control of the ion trap by rf and dc voltages is the focus of the Sec. 4.5. The helical resonator used to provide high voltage at low power is introduced. The system to control the different dc voltages for axial confinement and micromotion compensation is explained and a scheme for calibrating the voltages is presented.

Finally, the detection scheme providing a combination of high sensitivity to fluorescence of a single ion with a photomultiplier tube (PMT), as well as a high spatial resolution for Coulomb crystal characterization by an electron multiplying charge-coupled device (EMCCD) camera is explained.

## 4.1 Laser system

### 4.1.1 Level scheme of $^{172}\text{Yb}^+$

The advantage of the even isotope  $^{172}\text{Yb}^+$ , used to characterize the ion trap is the absence of a hyperfine structure and thus a low number of states that have to be addressed. An overview of the relevant energy levels is given in Fig. 4.2.

For efficient Doppler cooling the  $^2\text{S}_{1/2} \leftrightarrow ^2\text{P}_{1/2}$  transition with a natural linewidth of  $\Gamma \approx 2\pi \times 20$  MHz [50] at a wavelength of  $\lambda \approx 369.5$  nm is used. The saturation intensity  $s_0$  is given by

$$s_0 = \frac{\pi hc\Gamma}{3\lambda^3}, \quad (4.1)$$

which results to  $s_0 \approx 510$  W m<sup>-2</sup> for the given parameters. Furthermore, this wavelength is used for detection and photoionization of ytterbium, see Sec. 4.3.

Due to the decay channel from the  $^2\text{P}_{1/2}$  state to the long-lived  $^2\text{D}_{3/2}$  state with a branching ratio of 0.5 % [50], constant cooling of the ion is only possible by depleting the population of this dark state. Light with a wavelength of 935 nm excites the ion to the  $^3[3/2]_{1/2}$  state from where the population decays to the ground state, which closes the cooling cycle. In order to avoid optical pumping in the  $^2\text{D}_{3/2}$  state, an external magnetic field of about 200  $\mu\text{T}$  is applied. Additionally, the fluorescence is optimized by aligning the polarization of the repumping light with respect to the quantization axis given by the magnetic field.

Collisions with the background gas in the vacuum chamber can populate the metastable  $^2\text{F}_{7/2}$  state by a combination of non-radiative and radiative decays [51]. This state

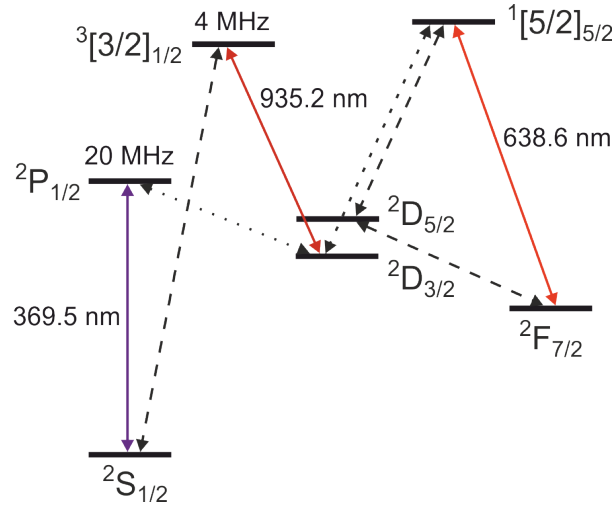


**Figure 4.2:** Partial level-scheme of  $^{172}\text{Yb}^+$  with atomic transitions used for Doppler cooling and detection at 369 nm and repumping at 935 nm. A second repumper depopulates the metastable  $^2\text{F}_{7/2}$  state, which can be populated by a combination of non-radiative and radiative decays due to background gas collisions in the vacuum chamber.

has an estimated lifetime of several years [18, 50], so the ion is lost for the experimental sequence and the decoupling from the cooling-cycle leads to heating and eventual loss from the trap. The state population is depleted with a laser at 639 nm. Also, quenching of the metastable state population via collisions with heavier background molecules such as  $\text{H}_2\text{O}$  is observed.

### 4.1.2 Lasers

Four different diode lasers are used for photoionization, cooling and detection, and repumping of  $^{172}\text{Yb}^+$ . Four fibers guide the different lasers to the trap, three of which carry the UV light for cooling and detection and photoionization and one of which carries the red and near infrared (NIR) light for repumping. The setup for all lasers is shown in Fig. 4.3. Included in this setup is the photoionization laser for indium, which for completeness is described here. Testing of the indium oven and successful loading of  $^{172}\text{Yb}^+ / ^{115}\text{In}^+$  Coulomb crystals is demonstrated later in this work.

For Doppler cooling and detection of  $^{172}\text{Yb}^+$  an optically amplified and frequency-doubled diode laser system<sup>1</sup> (extended cavity diode laser (ECDL)) with a maximum output power of  $P_{369\text{nm}} = 55 \text{ mW}$  is used. Over time a decrease in UV power of the system has been observed, mainly due to aging of the tapered amplifier (TA), whose power dropped from initially 320 mW to 170 mW within three years. After this time the UV power available after optimization of the incoupling into TA and doubling cavity is about 10 mW. By moving the doubling crystal within the cavity a few percent of the power can be recovered, which indicates damage of the anti-reflection coating of

<sup>1</sup>Toptica TA SHG pro, with DL pro

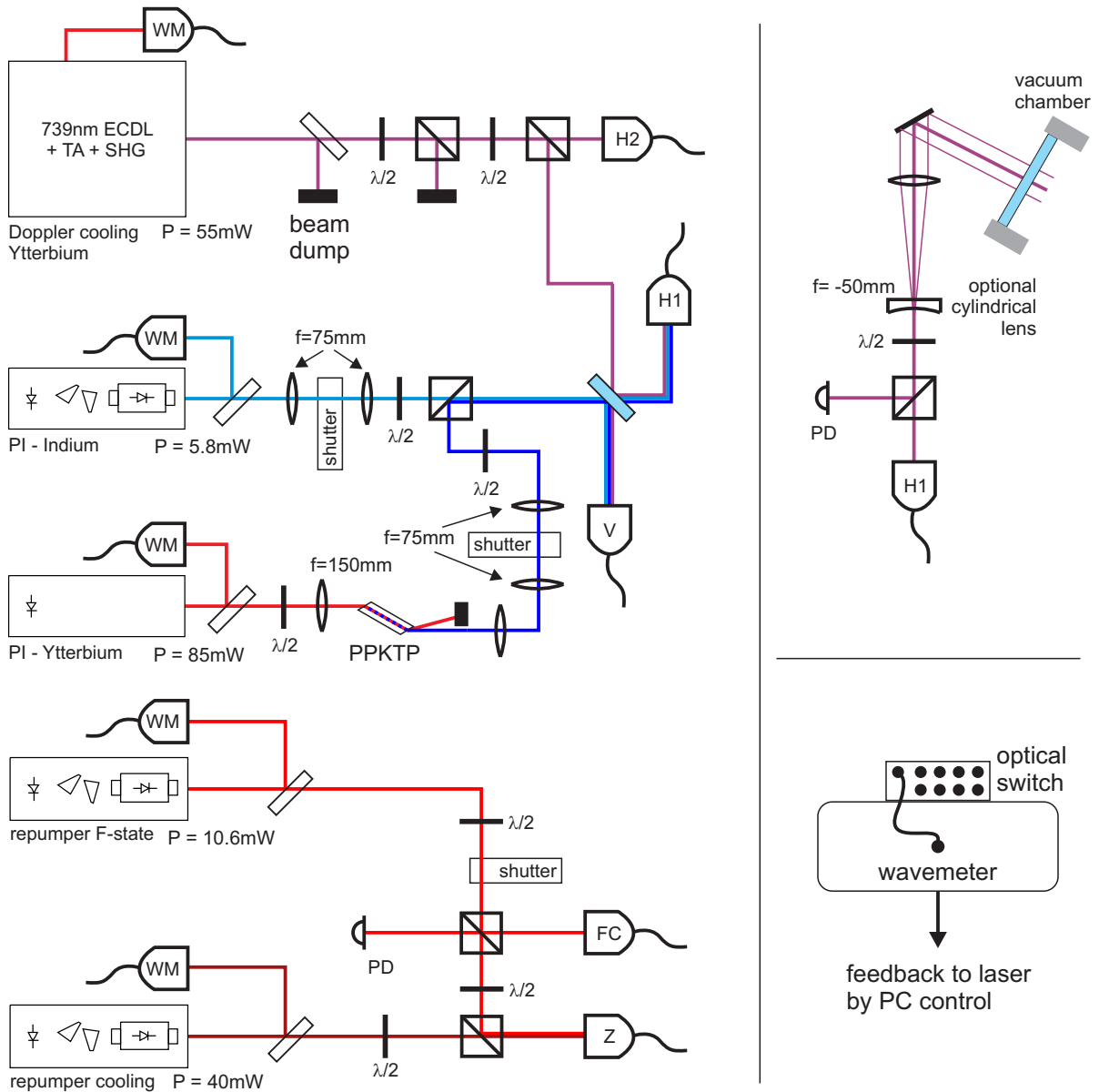


**Figure 4.3:** **Left:** Schematic setup of the lasers used for  $^{172}\text{Yb}^+$ , including the photoionization lasers for ytterbium and indium. The cooling and detection laser is split into three separate beams that are guided by polarization maintaining fibers to the experiment. Additionally, the photoionization beams are overlapped with the vertical cooling beam. The ionization light for ytterbium is obtained by frequency doubling of light at 798 nm in a PPKTP crystal in single pass configuration. The indium photoionization laser can also be detuned to the  $^2\text{S}_{1/2} \leftrightarrow ^2\text{D}_{5/2}$  transition of ytterbium in order to populate the  $^2\text{F}_{7/2}$  state for spectroscopy of the 639 nm transition. The two repump lasers are overlapped and coupled into a polarization maintaining fiber. An additional fiber coupling for the 639 nm laser provides connection with a frequency comb (FC) in order to perform absolute frequency measurements. **Right, Top:** Next to the vacuum chamber all lasers are focused with  $f = 500\text{mm}$  lenses. The beam H1 additionally provides a power detector. With a cylindrical lens the beams can be expanded in the horizontal direction for spectroscopy of linear Coulomb crystals or in more than one segment. **Right, Bottom:** All lasers are monitored with a wavemeter. Part of them are stabilized by software lock.

the endfaces of the crystal over time. However, this power is still enough to perform spectroscopy on single ions or Coulomb crystals.

The laser is divided into three beams, all sent to the trap via polarization-maintaining optical fibers. After the fibers, each beam is collimated and imaged into the trap with a waist of  $w_{369\text{nm}} \approx 80 \mu\text{m}$  using spherical lenses with an effective focal length of 500 mm. The fiber collimators<sup>2</sup> are equipped with achromatic lenses, in order to be able to overlap the Doppler cooling laser with the photoionization laser in the vertical direction, as well as with the stable laser at 411 nm. This laser is being set up in parallel to this work and will be used for precision spectroscopy and sideband cooling.

The power used for Doppler cooling and detection of a single ion is  $\approx 3 \mu\text{W}$ , which gives a saturation parameter of  $s_{369\text{nm}} \approx 0.6$  for each beam. In order to perform spectroscopy on Coulomb crystals in more than one segment, the beams can be expanded along the trap axis using additional cylindrical lenses, that act as a telescope together with the spherical lenses in the horizontal direction, see Fig. 4.3.

A second ECDL system<sup>3</sup> is used as a repumper in the cooling cycle. It provides an output power of about 40 mW at a wavelength of 935.2 nm. This light is guided to the ions by a polarization-maintaining single mode fiber and focused with a spherical lens of  $f = 500 \text{ mm}$  into the trap along the trap axis Z, see Fig. 4.1. Like this, about 20 mW are imaged with a waist of  $w_{935\text{nm}} \approx 125 \mu\text{m}$  in the trap.

For a deterministic clean-out of the  $^2\text{F}_{7/2}$  state, a second repump laser, at 638.6 nm is used in the experiment with an output power of  $P_{639\text{nm}} \approx 10.6 \text{ mW}$ . About 5.5 mW of this light is overlapped with the 935.2 nm laser beam, having a waist of  $w_{639\text{nm}} \approx 125 \mu\text{m}$  in the trap.

The overlapping of the two repump lasers leads to the problem of the single mode transmission of light of the used fiber, since the two wavelengths are about 300 nm apart from each other. The single mode cutoff wavelength is chosen to about 890 nm which means, that the repumper for the  $^2\text{F}_{7/2}$  state is not guided single mode anymore. Instead, the transverse mode of the laser can take a double peak shape, see Fig. 4.4.

Shown is the shape of the laser beam and its position relative to the Gaussian mode of the 935 nm repumper. It is recorded with a beam profile camera at the focus of the beams, which is imaged to the ion position. After adjusting the 935 nm laser only little intensity of the other repumper will be exposed to the ions because of this mode structure, making this laser inefficient. However, by adjusting the coupling of the 639 nm laser into the fiber the shape of the output can be adjusted to a Gaussian like shape with a considerable overlap with the 935 nm laser, see Fig. 4.4. Due to the sensitivity of this effect to the shape of the fiber, which can be changed by thermal fluctuations in the lab or moving of the fiber, the coupling needs to be checked weekly in order to maintain overlap of the two beam profiles.

For photoionization of ytterbium, a frequency-doubled ECDL system is used to resonantly excite neutral  $^{172}\text{Yb}$  to its  $^1\text{P}_1$  state. An infrared power of 80 mW is guided single pass through a Brewster-cut periodically-poled potassium titanyl phosphate (PPKTP)

---

<sup>2</sup>Schäfter & Kirchoff: for UV: 60FC-4-M10-01 with anti-reflection coating for 400 – 700 nm. for IR: 60FC-4-M12-NIR-10 with anti-reflection coating for 630 – 980 nm.

<sup>3</sup>DL 100, Toptica



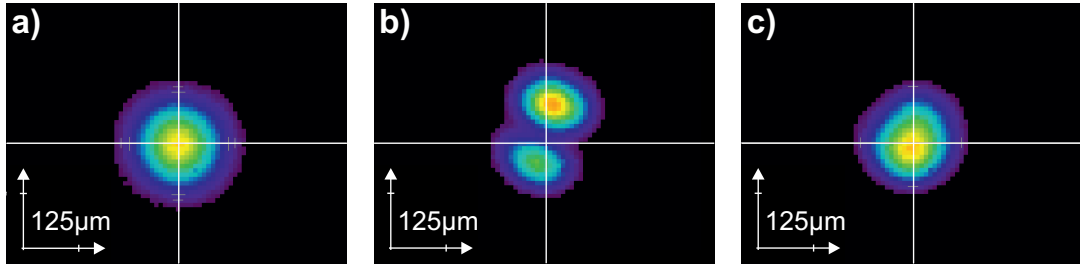


**Figure 4.4:** Images of the intensity profiles of the two repump lasers at the focus of the imaging lens in the axial beam ( $Z$ ), which is imaged in the trap. **a)** Image of the single-mode output of the optical fiber for the repump laser at 935 nm. The center of the beam is marked with a cross-hairs, which is kept at the same position in all pictures for comparison. **b)** Image of the repump laser at 639 nm for non-optimized fiber coupling. Almost no intensity of the laser is present in the center of the other repump laser, because the laser light is not guided single-mode through the fiber. **c)** Image of the 639 nm laser after optimizing the fiber coupling with the intensity maximum showing good overlap with the other repump laser. Both lasers have a measured radius of about  $125\ \mu\text{m}$  when overlapped.

crystal, which generates a power of  $P_{399\text{nm}} \approx 80\ \mu\text{W}$  in the second harmonic wave after optimized phase matching. The crystal is heated to a temperature of about  $51.4^\circ\text{C}$ , which is provided by a heat resistor. A power of  $7\ \mu\text{W}$  is sent to the atoms through the same fiber as the vertical cooling beam with an imaged waist of about  $80\ \mu\text{m}$ .

A second photoionization laser, resonantly exciting neutral  $^{115}\text{In}$ , is installed as well, delivering an output power of about  $5.8\ \text{mW}$  at a wavelength of about  $410.3\ \text{nm}$ . The beam is overlapped with the ytterbium photoionization laser and sent vertically through the trap as well. The photoionization schemes and the oven design will be explained in detail in Sec. 4.3

## 4.2 Laser stabilization

A wavelength meter based on a Fizeau interferometer<sup>4</sup> with an 8-channel multi-mode fiber switch is used to stabilize all lasers. This is realized by a self-written software lock, that compares the wavemeter readout to a set value and applies corrections as a feedback to the piezo voltage of the laser system as well as the diode current<sup>5</sup>. Depending on the exposure time of each channel, the fiber switch allows for a maximal readout rate of about  $1\ \text{ms}$  per channel, therefore giving a maximal bandwidth of the lock of  $1\ \text{kHz}$ , if only one channel is used. Because there are always four to five channels in use and some of them require a higher exposure time due to the lower available laser power, the bandwidth is reduced significantly to values in a range of  $10\ \dots\ 100\ \text{Hz}$ .

<sup>4</sup>High Finesse, WS-7

<sup>5</sup>Simultaneous modulation of piezo voltage and diode current is provided by the feedforward function of the Toptica control unit.

This stabilization scheme is sufficient to prevent the lasers from slow drifts and is only limited by the instability of the wavemeter. The latter was investigated by measuring the wavelength of a stable laser with the wavemeter and calculating the Allan deviation. The laser used is a diode laser system stabilized to an ULE cavity, which leads to a sub-hertz linewidth and a linear drift of  $\sim 100 \text{ mHz s}^{-1}$ , which can be neglected on time scales of several days. Figure 4.5a shows the Allan deviation of a measurement over 20 minutes exhibiting a drift of the wavemeter of about 3 MHz per hour.

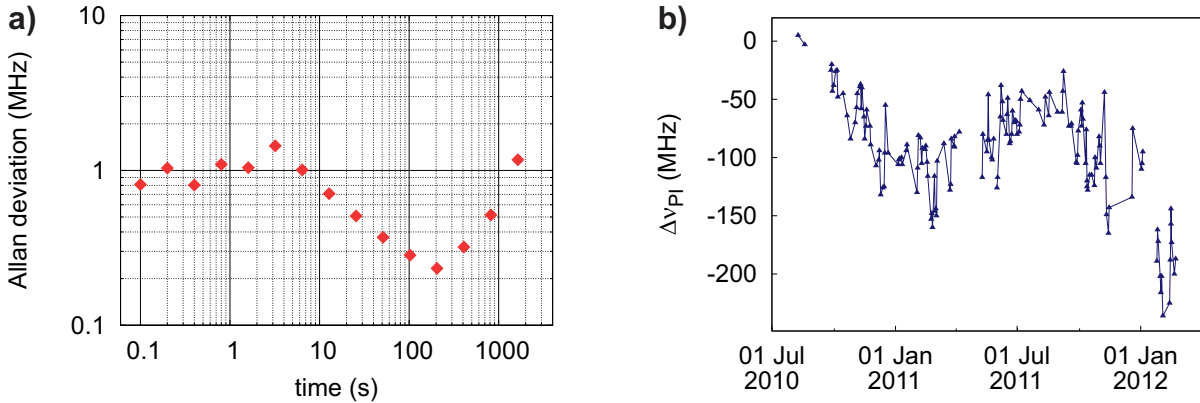


**Figure 4.5:** **a)** Allan deviation of the wavemeter readout from the stable laser at 822 nm over a measuring time of 20 minutes. A drift of  $\sim 3 \text{ MHz h}^{-1}$  is deduced. **b)** The atomic resonance of ytterbium measured over more than one year. The frequency of the 798 nm laser is given as the difference of the measured resonance to the set value of the laser stabilization. The overall drift is in agreement with the specified absolute accuracy of 200 MHz of the wavemeter. A change from day to day of about up to 50 MHz is in accordance with the drift derived from the measurement of the stable laser.

On the timescale of seconds the stability is about 1 MHz, which is sufficient to prevent the lasers from drifting within typical measurement time scales of seconds to minutes. For example, during photon-correlation spectroscopy the acquisition time of a single measurement event is 30 s, see Sec. 5.2.

To evaluate the instability on longer time scales a measurement of the atomic resonance at 399 nm as a function of time is plotted over a period of more than one year, see Fig. 4.5b. The measured deviation is in agreement with the specified absolute accuracy of 200 MHz in multi-channel switch operation. A day to day drift of about 50 MHz is consistent with the drift estimated from the Allan deviation.

Recording the wavelength of this laser over several days together with the ambient temperature of the wavemeter reveals a clear dependence of the wavemeter readout with the temperature, with a proportionality factor of  $15 \text{ MHz K}^{-1}$ .

In order to correct this drift on the different laser wavelengths, the atomic resonances and the resonance of the cooling transition have been measured repeatedly and compared to the frequency of the stable laser. Figure 4.6 shows the correlation of the different lasers, giving a linear function with characteristic slope for each laser  $l$ :  $\nu^{(l)}(t) = s^{(l)} \cdot \nu_{822}(t)$ . With this correlation it is now possible to correct the set values for the individual lasers

$\nu_{\text{set}}^{(l)}$  by monitoring the drift of the wavemeter output of the stable laser  $\nu_{822}(t + \Delta t)$  after time  $\Delta t$ . Multiplying the drift with the individual slope a correction can be applied to the set value for the lock of each laser in order to compensate for the wavemeter drift:  $\nu_{\text{set}}^{(l)}(t + \Delta t) = s^{(l)} \cdot \nu_{822}(t + \Delta t)$ .

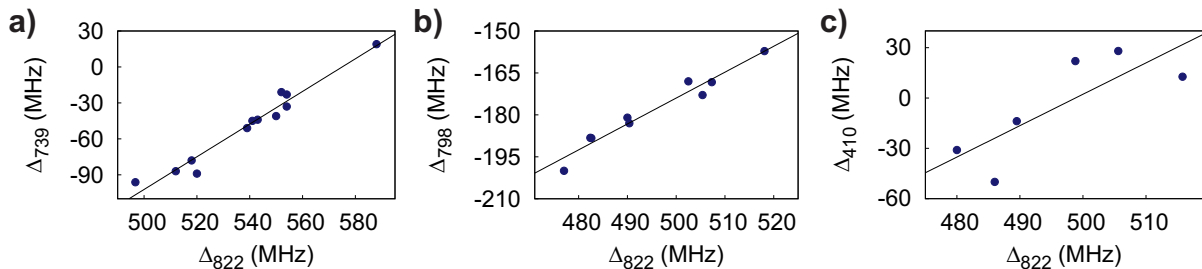


**Figure 4.6:** Correlation of measured frequency of the stable laser  $\Delta^{(822)} = \nu^{(822)} - 364\,738\,000$  MHz with the wavelength of the other lasers, in order to compensate wavemeter drifts based on the stable laser as a reference. For each laser  $l$  a linear function  $\nu^{(l)}(t) = s^{(l)} \cdot \nu_{822}(t)$  is fitted in order to correct the set values of the laser stabilization after a drift of the wavemeter measured with the stable laser. The frequencies plotted are relative to the according set values:  $\Delta^{(l)} = \nu^{(l)} - \nu_{\text{set}}^{(l)}$ . The set values and fitted slopes are **a)**  $\nu_{\text{set}}^{(739)} = 405\,646\,363$  MHz,  $s^{(739)} = 1.36 \pm 0.09$ , **b)**  $\nu_{\text{set}}^{(798)} = 375\,763\,584$  MHz,  $s^{(798)} = 0.93 \pm 0.08$  and **c)**  $\nu_{\text{set}}^{(410)} = 730\,692\,762$  MHz,  $s^{(410)} = 1.9 \pm 0.7$ .

Worthwhile mentioning is the fact, that the repeatability of the wavemeter decreases in the range of short wavelengths, which can be seen in the higher scatter of the measured neutral indium resonance compared to the ytterbium resonances. For ytterbium all monitored wavelengths are in the red and near infrared (NIR) range.

### 4.3 Atomic oven design and photoionization of Yb and In

In the experiment  $^{172}\text{Yb}^+$  and  $^{115}\text{In}^+$  ions are created by photoionization of atoms in the trapping region.

Both ionization schemes consist of a two-step excitation, in which the atoms are first excited resonantly to an intermediate state with the photoionization lasers described in Sec. 4.1. To reach the ionization threshold in the case of ytterbium the energy of two photons at 399 nm is not sufficient. For this the cooling laser is used. In the case of indium the ionization threshold is lower than the energy of two photons at 410 nm, thus one laser is sufficient. Both schemes are visualized in Fig. 4.7 and Fig. 4.8.

The oven design consists of a vertical tantalum tube with an outer diameter of 1.02 mm and an inner diameter of 0.86 mm. On both ends, copper wires are spot-welded to provide the heating current, see Fig. 4.7. A 0.4 mm diameter hole on the side of the tantalum tube generates a cone of atomic vapour. To collimate the atomic beams of

both ovens, a copper shield with two slits of  $\approx 1$  mm in the horizontal direction is placed between the ovens and the trap, assuring atomic flux through the loading segment, while the spectroscopy segments do not get contaminated, see Fig. 4.1.

Because the collimated atomic beams pass horizontally through the trap and the photoionization light is guided vertically, Doppler shifts and broadening of the atomic lines are avoided.

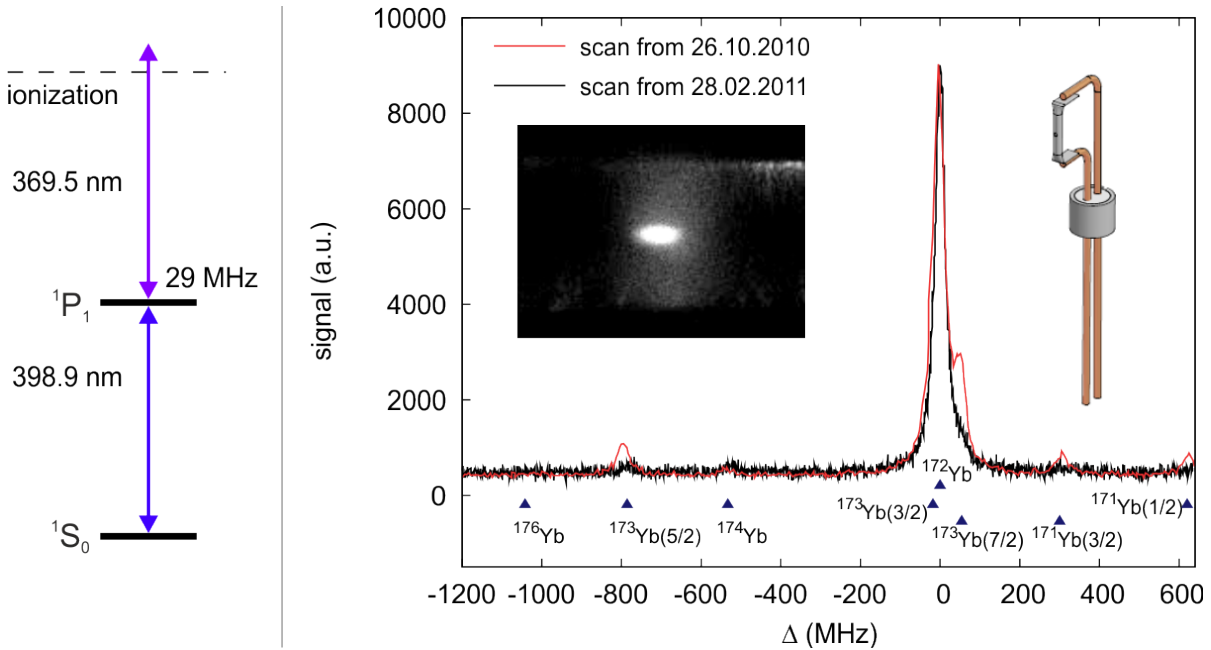


**Figure 4.7:** **Left:** The ionization scheme for ytterbium as a two-step excitation. **Right:** Scan of the 399 nm laser with isotope enriched  $^{172}\text{Yb}$  sample. The expected resonances of the various isotopes [52] are indicated by triangles. The left inset shows a picture of the loading trap segment with atoms fluorescing in the trace of the vertical photoionization laser. The bright spot is a cloud of laser cooled  $^{172}\text{Yb}^+$  ions. The right inset shows a drawing of the oven. At the ends of the tantalum tube copper wires are spot-welded, which are separated by a macor spacer held together by a steel ring.

For ytterbium an isotopically-enriched sample is used, as the natural abundance of the isotopes  $^{172}\text{Yb}$  and  $^{173}\text{Yb}$  are 22 % and 16 %, respectively. Their photoionization resonances are separated by only 55 MHz and exhibit considerable overlap, which is why it is important to avoid broadening effects. Two frequency scans of the photoionization laser are shown in Fig. 4.7. The earlier one displays the dominant peak for the isotope  $^{172}\text{Yb}$ , but also a residual abundance of other isotopes, in particular  $^{173}\text{Yb}$ . The full-width half maximum is measured as about 35 MHz at a saturation parameter of  $s = 2\Omega^2/\Gamma^2 \lesssim 1$ , where  $\Omega$  is the Rabi-frequency and  $\Gamma$  the decay rate of the excited state. Within about four months a depletion of the other isotopes occurred without recovering again, which is shown in the later scan.

Furthermore, an image of the loading segment is shown in Fig. 4.7. Neutral ytterbium atoms are visible in the trace of the photoionization laser passing vertically through the

trap. The bright spot in the middle of the trapping region is a cloud of laser cooled  $^{172}\text{Yb}^+$  ions. The collimation of the atomic beam could be verified by scanning the laser beam through all trapping segments and detecting fluorescence only in the loading segment. A beam width of about less than two millimeters was observed positioned in the center of the loading segment.

The indium oven has been tested as well. Because the natural abundance of  $^{115}\text{In}$  is about 95 % an enriched sample is not necessary. As a source a piece of a wire of 99.999 % pure indium that fits in the tube is used. In the case of indium the only material suitable for the oven is tantalum, since it is the only metal that does not alloy with indium.

By detecting an atomic signal with the same beam alignment as for the ytterbium laser, the adjustment of the indium oven to the loading segment was confirmed. In Fig. 4.8 a frequency scan of the photoionization laser is shown. The resonances are

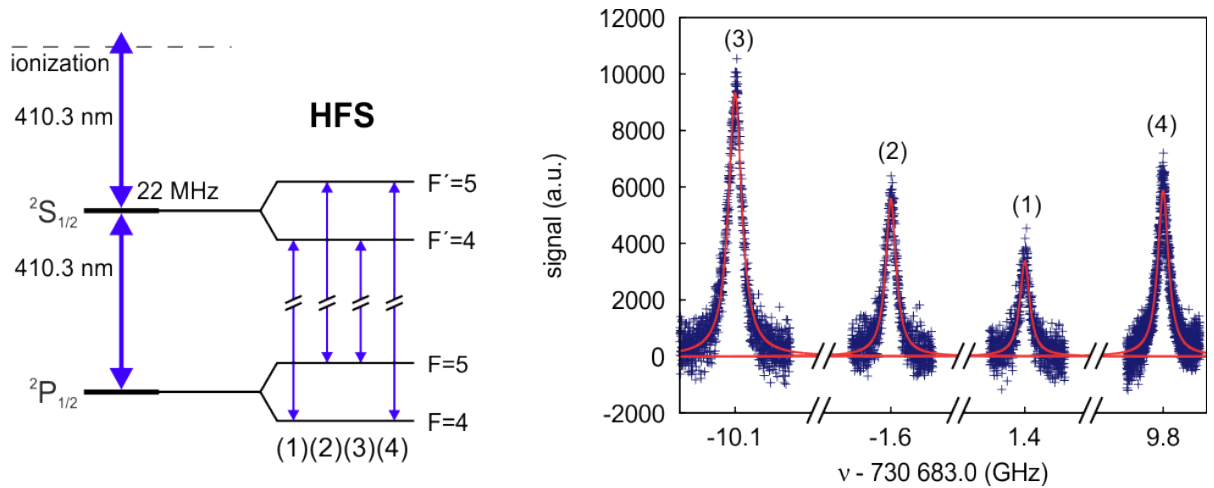


**Figure 4.8:** **Left:** The ionization scheme for indium as a two-step excitation with a single laser. Because of the hyperfine structure (HFS) four lines are visible in the scan. **Right:** Scan of the 410 nm over the resonance. The signals are fitted with Lorentzian function giving linewidths between 50 MHz and 70 MHz for a saturation of  $s \approx 6$ . The highest relative intensity of line (3) suggests most efficient ionization with this line. The relative strengths of the individual lines show good agreement with previous measurements [53].

fitted with a Lorentzian function and the obtained linewidths are between 50 MHz and 70 MHz due to a saturation of  $s \approx 6$ . From the relative signal strengths the most efficient ionization can be achieved with resonance (3).

## 4.4 Vacuum system

The vacuum chamber is based on a DN250 tube with flanges on the side to connect various windows. A horizontal cut through the chamber including all relevant components of the system is shown in Fig. 4.1. At the bottom flange all electrical feedthroughs and a window for the vertical beam axis (V) are located. An 8 pole high current feedthrough

provides connection with the ovens, a coaxial high voltage<sup>6</sup> connector provides the rf feed for the trap. A 41 multipole connector provides the dc voltages for axial confinement and micromotion compensation.

The windows on the side of the chamber have an anti reflection coating in the ultraviolet (UV) range with a local minimum at 230 nm for the indium spectroscopy laser. For the detection a reentrant window with a non-magnetic seal is mounted with a distance of 23 mm to the trap in order to obtain higher collection efficiency of the ion fluorescence. Two horizontal beam axes (H1 and H2) are provided by four windows, aligned under 25° to a third axis (Z), which is in the direction of the trap axis.

Opposite to the reentrant window the vacuum pumps and an angle valve for connection of a turbo molecular pump for initial pumping are mounted. After that the vacuum is maintained by an ion getter pump<sup>7</sup>, having a nominal pumping speed of 20 mbar l s<sup>-1</sup> for air and a titanium sublimation pump<sup>8</sup> in a DN63 tube, with a calculated pumping speed of 490 mbar l s<sup>-1</sup> for hydrogen.

After closing the chamber for the first time, a bake out was done with every component built in except for the ion trap. The temperature was kept between 190...200 °C for two weeks in order to clean the system and to reduce desorption of hydrogen from the chamber walls. After this, the chamber was reopened to insert the trap contaminating the chamber with water vapour from the air. From this conditions a residual pressure of  $\sim 1.5 \times 10^{-9}$  mbar was obtained after pumping. Within a few months and by repeatedly firing the titanium sublimation pump<sup>9</sup> the pressure could be reduced to  $\sim 4 \times 10^{-10}$  mbar.

With the trap built in a modest bake out was done in order to further reduce the water in the chamber. For two weeks the temperature was kept between 60...100 °C leading to a reduced pressure of  $\sim 1.5 \times 10^{-10}$  mbar.

After changing the laser cut ion trap with the milled trap a third bake out was done. The temperature was kept between 100...125 °C for five days resulting in an end pressure of  $\sim 8 \times 10^{-11}$  mbar.

## 4.5 Trap drive

### 4.5.1 RF voltage drive

For the application of the rf voltage to the ion trap a helical resonator is used. One reason for this is to match the impedances of the amplifier output and the trap in order to reduce the power necessary for a given voltage. Another reason is the filtering of amplifier noise by the resonator due to its small bandwidth at a high Q factor.

According to MacAlpine *et al.* [54] the resonator was designed for an unloaded resonance frequency of about 45 MHz. Given the capacitance of the ion trap (see Ch. 2) the resonance frequency of the trap – resonator system is expected to drop to about 25 MHz,

---

<sup>6</sup>HN-type

<sup>7</sup>Varian starcell

<sup>8</sup>Varian TSP filament

<sup>9</sup>For this a current of 47 A is applied for one minute.

the designated trap drive frequency. A schematic of the resonator design is shown in Fig. 4.9.

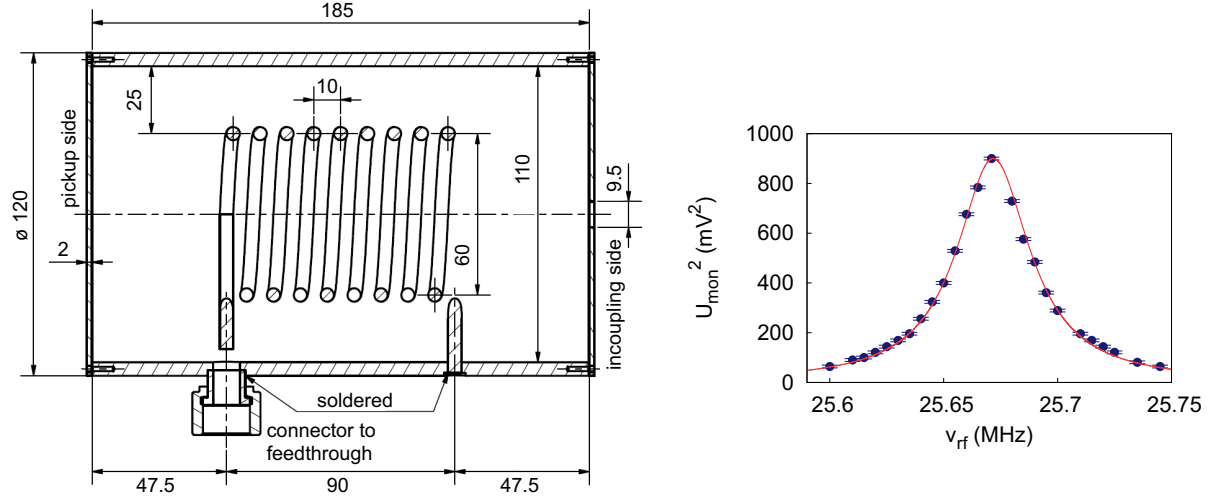


**Figure 4.9:** **Left:** Schematic drawing of the helical resonator for rf voltage generation, the dimensions are given in mm. A pickup not drawn here is mounted on the left cover. The incoupling coil is mounted on the right side. **Right:** Measurement of the resonance when connected to the milled trap. The fitted Lorentzian function has a full width at half maximum of  $\Delta\nu = (39.0 \pm 0.7)$  kHz and a maximum at  $\nu = 25.67$  MHz, which gives a Q factor of  $Q_1 = \nu/\Delta\nu \approx 640$ .

On the incoupling side a single winding coil is mounted next to the resonator coil to inductively transmit the power into the circuit. The coupling is optimized by altering the distance between the two coils for impedance matching.

After setting the distance to the optimized point an unloaded Q factor of  $Q_u \approx 1050$  was reached. Connecting the resonator to the trap a loaded Q factor of  $Q_1 \approx 640$  was obtained in the case of the laser cut trap with a resonance frequency of  $\Omega_{\text{rf}} = 2\pi \times (25.67 \pm 0.01)$  MHz. For the milled trap, which was built in at a later time, the Q factor amounts to  $Q_1 \approx 590$  at a resonance frequency of  $\Omega_{\text{rf}} = 2\pi \times (25.42 \pm 0.01)$  MHz. The loss in the Q factor compared to the laser cut trap is possibly due to the thicker wafers of the milled trap, in which more rf power is dissipated.

A schematic of the rf electronics is shown in Fig. 4.10. The rf signal from a frequency generator<sup>10</sup> is split into two paths one of which is used for the trap drive, whereas the other one is used as a trigger for the photon-correlation spectroscopy, see Sec. 5.2. A mixer<sup>11</sup> is used to add modulation signals, e.g. for parametric heating of the ions to measure secular frequencies. The modulated signal is amplified<sup>12</sup> and coupled into the helical resonator, which is connected to the trap. The attenuator before the mixer reduces the signal by 3 dB to optimize the working range of the rf generator, in which no internal switching occurs that otherwise leads to the loss of the ions.

<sup>10</sup>Marconi: 2024

<sup>11</sup>minicircuits: ZAD-6+

<sup>12</sup>minicircuits: ZHL-5W-1, amplification: 46 dB

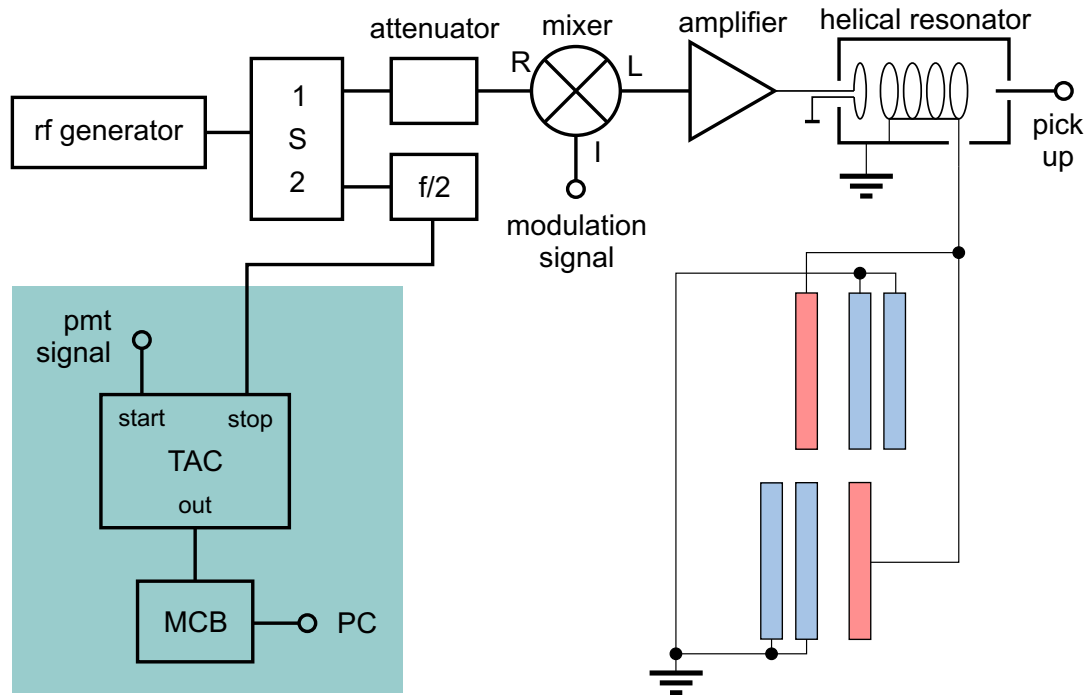


**Figure 4.10:** Schematic of the rf circuit for the trapping rf voltage. The rf signal is split into two paths, one of which used for photon-correlation measurements (setup in the green box, a detailed description is given in Sec. 5.2). The other part is amplified and coupled to the helical resonator for impedance matching of the amplifier with the resonator. The rf mixer in between can be used to modulate the signal, e.g. for parametric excitation of secular ion motion or as a controlled switch of the trapping potential amplitude. The rf electrodes are connected directly with the output of the resonator via copper foil leads and the coaxial feedthrough. The  $GND_{\text{rf}}$  electrodes are connected with the vacuum chamber as is the resonator shield. The rf signal coupled inductively into the resonator has an independent ground connection from the resonator. From the pickup the monitor voltage  $U_{\text{mon}}$  is read out with an oscilloscope.



In order to monitor the rf voltage on the trap electrodes a thin copper wire is placed inside the helical resonator sensing a monitor voltage  $U_{\text{mon}}$ . The monitor voltage is calibrated by measuring the output voltage of the coil with a low capacitance field probe yielding a calibration factor  $\kappa = 5400 \pm 340$ .

### 4.5.2 DC voltages

The dc voltages are generated by an analog output PCI card<sup>13</sup> and software controlled. The outputs are connected to a self-built control unit, in which the trapping voltage  $U_t$  and the compensation voltages  $U_{tc}$  and  $U_{ec}$  are added up and scaled appropriately, which will be discussed in the following. The control unit is then connected directly with the feedthrough of the vacuum chamber by a pairwise shielded multi-core cable in order to reduce coupling of high-frequency noise.

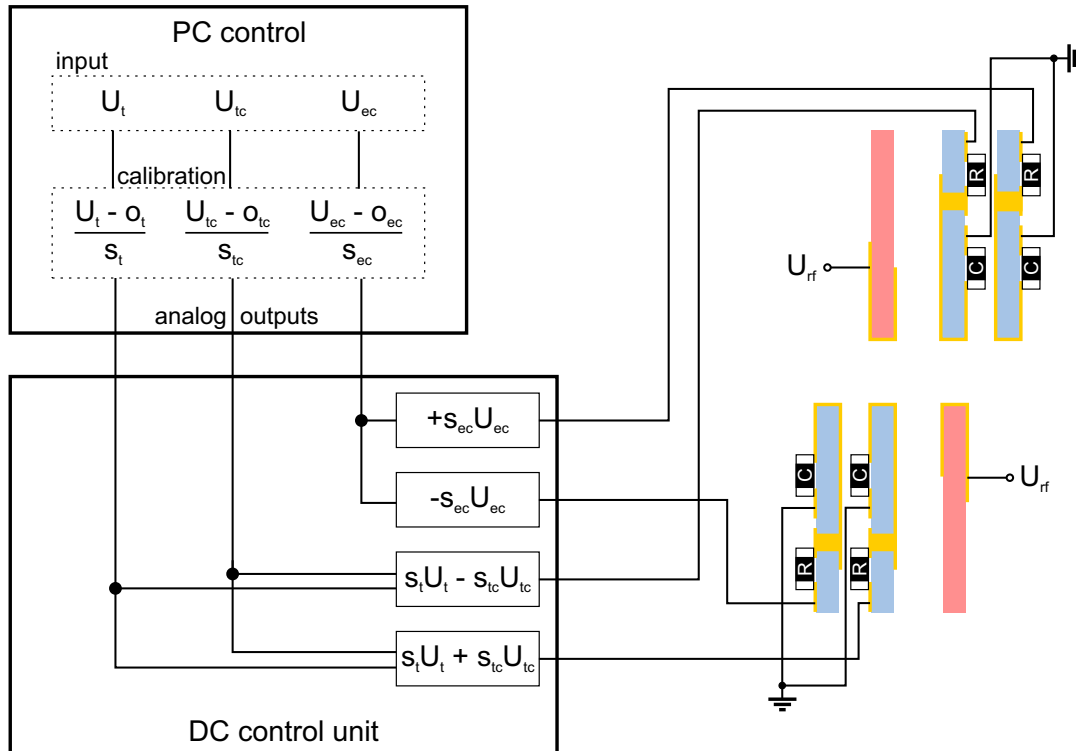


**Figure 4.11:** Schematic drawing of the dc voltage control. The voltages are generated with the AO card and distributed in the DC control unit. On the trap wafers the voltages are connected to the electrodes in series with a resistor in order to avoid currents back to the control unit. The capacitors connect the electrodes to rf ground, simultaneously shorting high-frequency noise to rf ground. The signals are calibrated within the PC control software, but split up and added (subtracted) by independent electric circuits within the DC control unit. Due to this, the calibration can be done with a precision given by the tolerances of the electric components in the different circuits.

As shown in Fig. 3.1,  $U_t$  is applied to both  $GND_{rf}$  electrodes of a trap segment for providing axial confinement or squeezing of the radial trapping potential.  $U_{tc}$  is added on one electrode but subtracted on the other in order to create an electric field for micromotion compensation. This is realized in the control unit by two independent electric circuits, whose outputs are directly connected with one of the electrodes for each

<sup>13</sup>National Instruments: NI 6723 with 32 analog outputs

trap segment. Another two circuits provide the compensation voltage  $U_{ec}$ , one with positive and the other one with negative sign. A schematic of the dc voltage generation and connection is shown in Fig. 4.11

The circuits provide low pass filtering and scaling of the voltages as well. The compensation voltage  $U_{tc}$  is divided down by a factor of four in order to improve the resolution. For the extra compensation electrodes  $U_{ec}$  is multiplied by 1.2. First, because the distance to the ions is larger and the applied field therefore becomes smaller for the same voltage and secondly to use the full range of the operational amplifiers used. The analog outputs of the PCI card have a range of  $\pm 10$  V and a resolution of 13 bit, yielding a step size of 2.44 mV. The obtained resolution for the different dc electric fields is given in Tab. 3.4.

The whole system is calibrated by measuring the output voltages for given input values and applying corrections to the input values within the control software. For this the output values are plotted against the input values and a linear function  $U_{out} = o_c + s_c \cdot U_{in}$  is fitted, Fig. 4.12a shows a measurement of  $U_t$  on the  $GND_{rf}$  electrodes of segment 2. The obtained calibration parameters  $o_c$  and  $s_c$  are applied to the input values in the control software:  $U_{cal} = (U_{in} - o_c)/s_c$ . As a cross-check  $U_t$  is measured again after calibration, see Fig. 4.12b.

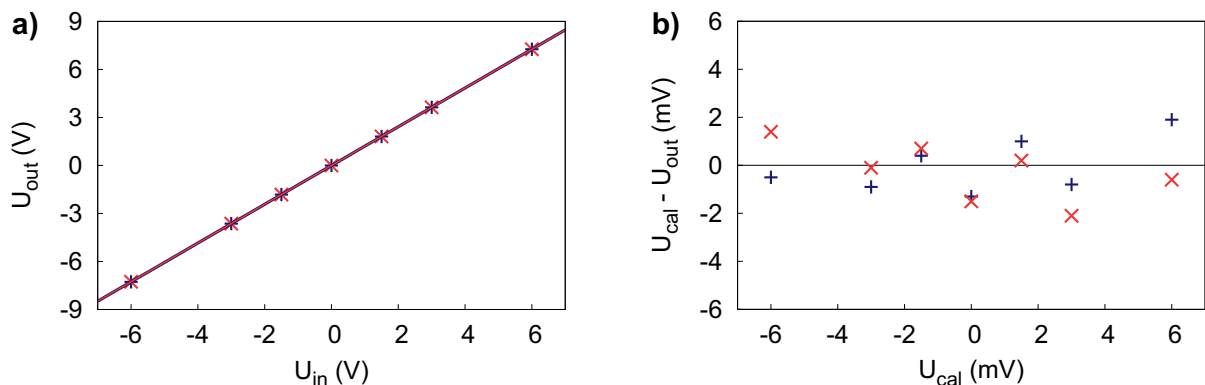


**Figure 4.12:** Example for the calibration of the dc voltages, shown is a measurement of  $U_t$  on both  $GND_{rf}$  electrodes 1 (blue cross) and 2 (red x) of trap segment 2. **a)** Output voltage measured before calibration showing the scale factor of 1.2. A linear function is fitted to obtain the calibration factors:  $o_c^{(1)} = (-4.5 \pm 0.3)$  mV,  $s_c^{(1)} = 1.2110 \pm 0.0001$ ,  $o_c^{(2)} = (-3.5 \pm 0.3)$  mV and  $s_c^{(2)} = 1.2106 \pm 0.0001$ . **b)** Output voltage measured after calibration with the applied corrections  $o_c^{(1)} = -4.5$  mV,  $o_c^{(2)} = -3.5$  mV and  $s_c = (s_c^{(1)} + s_c^{(2)})/2 = 1.2108$ . The residual error due to the two different scalings is  $\leq 10^{-3}$  for all dc electrodes.

The output voltages for the two electrodes providing  $U_t + U_{tc}$  and  $U_t - U_{tc}$  are not perfectly balanced, because they are provided by independent circuits, that operate with independent voltage dividers. The latter are matched only within their specification and can therefore not deliver equal outputs for a common input signal. The residual error in the scaling is  $\leq 10^{-3}$ . For the correction the average value of both measured scale factors is chosen.

The measured offset of a few millivolt stems from the PCI card, whose analog outputs have a specified absolute accuracy of 10.78 mV at full range ( $\pm 10$  V).

## 4.6 Detection

The detection scheme, as shown in Fig. 4.1, is twofold: it is possible to either detect with the EMCCD camera<sup>14</sup> or with a photomultiplier<sup>15</sup>. Also, it is possible to detect ions with both devices simultaneously using a 50/50 beam splitter. Figure 4.13 shows a schematic of the lenses.

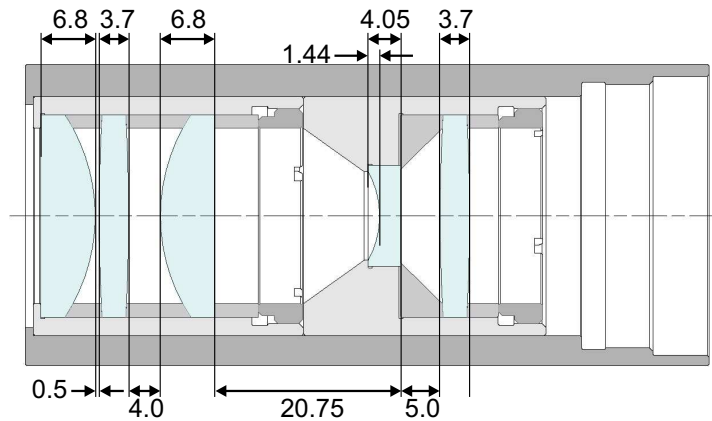


**Figure 4.13:** Schematic drawing of the self-built retro focus optics for single ion detection using five spherical lenses with one inch diameter. The focal lengths are from left to right: 50 mm, 250 mm, 50 mm,  $-25$  mm and 250 mm. The dimensions are given in mm. The optimal distances between the lenses was calculated with commercial ray tracing software. For diffraction limited imaging, tolerances of 0.1 mm to 0.01 mm need to be adhered to.

The optics is a five lens retro focus system optimized with commercial ray tracing software<sup>16</sup>. The distances of the lenses are optimized for a wavefront error of less than  $\lambda/4$ . The lens has a working distance of 31 mm and a numerical aperture of  $NA \approx 0.27$ , which allows for a collection efficiency of about 2% of solid angle. The lenses have a broadband UV anti-reflection coating including the detection light of  $^{115}\text{In}^+$ . The optics is mounted on a three-axis translation stage.

The whole optical path is encapsulated in order to avoid stray light. In the box containing the mirror and beam splitter a filter is protecting camera and photomultiplier transmitting only the wavelength of the detected light. Different filters are exchanged manually in order to detect the atomic signals of indium and ytterbium or the fluorescence of ytterbium ions.

<sup>14</sup>Andor: DU-897, 512 px  $\times$  512 px, quantum efficiency  $QE = 35\%$  for 200 nm – 370 nm

<sup>15</sup>Hamamatsu: R7207-01, Bialkali window,  $QE \geq 20\%$  for 160 nm – 650 nm

<sup>16</sup>Oslo

In this setup a magnification of  $V \approx 25$  is designed, yielding with the pixel size of the camera of  $16 \mu\text{m}$  a theoretical resolution of about  $600 \text{ nm}$ . At the wavelength  $\lambda_{\text{Yb}^+} = 370 \text{ nm}$  the diffraction limit is estimated to be  $dx_{\text{min}} = \lambda/(2NA) \approx 570 \text{ nm}$ . The resolution achieved in the experiment is about  $1.5 \mu\text{m}$ . This was evaluated by measuring the half width at full maximum of a fluorescence spot of a single ion. An estimation of the wavepacket extension  $x_x$  of the harmonic oscillator at the Doppler limit for  $^{172}\text{Yb}^+$  of  $T_{\text{D}} \approx 0.5 \text{ mK}$  yields  $x_{\text{D}} = \sqrt{\frac{k_{\text{B}}T_{\text{D}}}{2m\omega_z^2}} \approx 175 \text{ nm}$ , with an axial secular frequency of  $\omega_z = 2\pi \times 100 \text{ kHz}$ .

# Chapter 5

## Characterization of prototype trap

In this chapter measurements are shown to characterize the prototype trap and compare the experimental results with the calculations presented in Ch. 2 and 3.

First, the controlled loading of  $^{172}\text{Yb}^+$  ions into the laser cut trap is demonstrated and the optimized parameters for a controlled loading process are presented. Furthermore, the capability of trapping and Doppler cooling Coulomb crystals is demonstrated. Secondly, the secular frequencies of a single ion are measured in both traps by parametric excitation of the ion motion and the Mathieu parameters are derived. These are compared to the estimated values presented in Sec. 3.2.

Residual rf electric fields are measured in both traps using photon-correlation spectroscopy. The method is explained in detail, as well as the evaluation of rf electric fields from the obtained data. Particular effort is put into the quantitative analysis of the data and the determination of the sensitivity of the spectroscopy method.

With this, excess micromotion is measured in all dimensions in the trap and compared to the FEM calculations presented in Sec. 2.4 and 3.2. The radial electric field components are used to calibrate the spectroscopy, because the numerical estimation gives reliable results within a few percents. The axial field component, which is about three orders of magnitude smaller than the radial component, is also measured and compared to the calculations. From this measurement, a deviation from an idealized geometry to the built prototype trap can be estimated. For the axial rf field both the laser cut trap and the milled trap have been investigated and compared with each other.

Using the photon-correlation spectroscopy, other properties of the laser cut trap are characterized. By compensating the micromotion in the loading segment as well as in the adjacent central segment over several loading cycles, the influence of atomic contamination from the oven is investigated. Longterm measurements on different time scales demonstrate the stability of micromotion compensation, a particular requirement for ion traps in a clock. The crosstalk of the compensation voltages to neighbouring trap segments has been measured and compared with the theoretical values.

## 5.1 Loading and trapping ions

### 5.1.1 Deterministic loading of $^{172}\text{Yb}^+$ ions

For a first test to trap ions, a single lens was used to observe the whole trapping region. The photoionization laser was sent through the trap vertically and aligned along the trap axis until fluorescence of neutral ytterbium was observed while scanning the laser frequency. Both lasers were scanned in frequency over the estimated resonances until fluorescence was observed, after which the parameters could be optimized and the resonances could be measured.

To test functionality of all trap electrodes, ions were loaded and shuttled into all segments. Figure 5.1 shows two ion clouds trapped simultaneously and each illuminated by one of the horizontal beams H1 and H2.

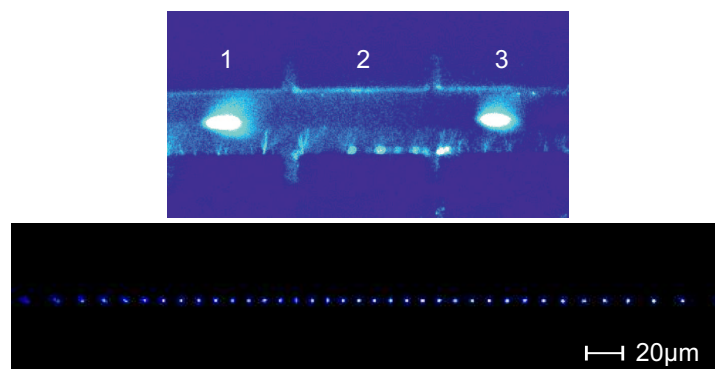


**Figure 5.1:** **Top:** Trapping of clouds of  $^{172}\text{Yb}^+$  ions in segments 1 and 3, illuminated by beams of the cooling laser along H1 and H2. The stray light of the laser beams makes the segmented trap structure visible. **Bottom:** Picture of a linear Coulomb crystal of 37  $^{172}\text{Yb}^+$  ions, trapped in segment 3 and imaged with the self-built lens.

The detection lens described in Sec. 4.6 was initially aligned by imaging the stray light of a laser pointer with a wavelength of 410 nm and power of 1 mW illuminating the trap electrodes. The position of the lens when imaging the corners of the electrodes was recorded to interpolate the lens positions for the trapping region. For positioning along the optical axis, a correction due to chromatic aberration was applied taking into account the different wavelengths of the laser pointer and the cooling laser.

The conditions for controlled loading of single ions were investigated by varying the power of the photoionization laser as well as the oven current. The optimal compromise for both parameters was found by looking at the probability to generate reliably not more than a single ion within a loading period of about one second or longer. The optimal parameters found are about  $P_{399} \approx 5 \mu\text{W}$  and  $I_{\text{oven}} \approx 5.5 \text{ A}$ . In Fig. 5.2 the fluorescence of ions loaded with a continuously running photoionization laser is shown. Visible are the typical steps of the signal as each new ion appears and the Coulomb crystal is rearranged. Also visible is the drop in fluorescence at the time of ionization due to the heating of the crystal by the initially “hot” new ion.

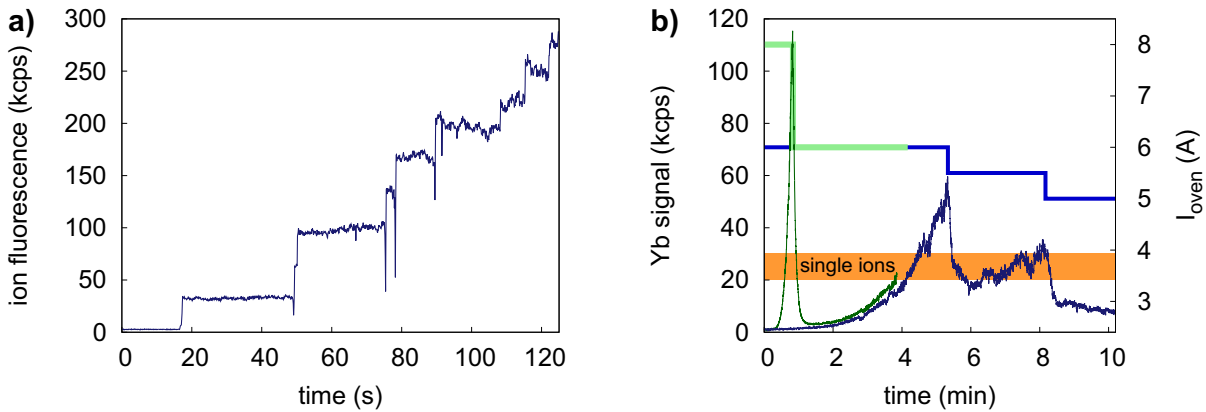


**Figure 5.2:** **a)** Loading of ions into the laser cut trap, with the arrival of each new ion indicated by a step-like increase of the fluorescence. The drop of fluorescence at some of the steps is caused by heating and temporary melting of the crystal when a new ion arrives with high kinetic energy. **b)** Fluorescence of neutral ytterbium for different oven currents. The blue (green) curve is recorded with a starting current of  $I_{\text{oven}} = 6$  A ( $I_{\text{oven}} = 8$  A). The power of the photoionization laser is about  $7 \mu\text{W}$ . The lower current is by experience the optimal compromise of fast heating and low rate of increase of atomic flux in order to reliably load single ions. When starting with a too high current, the atomic flux increases within only a few seconds to values much higher than required for distinguished ionization of single atoms. When using a current less than 6 A the longer warm-up period increases the dead-time of the experiment. However, for experiments containing long loading periods a lower current yields a stationary atomic flux suitable for single-ion loading. The attempt to start with a higher current to accelerate heating and then turn down the current to lower values that gives a low enough rate of increase of atomic flux is not successful due to the heat capacity of the oven.



For an optimum cooling efficiency of trapped ions the intensity of the cooling laser is rather low,  $s < 1$ , [55]. Within the optimization of the loading process it has been observed, that the initial cooling of ionized atoms and therefore the recrystallization happens faster for higher laser intensities, e.g.  $s \approx 5$  in Fig. 5.2a. With low intensity it is possible, that ionized particles stay in higher radial orbits for several seconds or longer without being cooled and detected due to the high Doppler shift with respect to the cooling laser and are therefore not recognized as a trapped ion. Sometimes the ion only can be cooled by detuning the cooling laser further away from the resonance to the red and chirping it back. Thus, for loading single or only few ( $\sim 1 \dots 10$ ) ions, it is helpful to increase the cooling laser power. For an increasing number of ions the initial cooling becomes more efficient even with low laser power due to the sympathetic cooling of the present ions.

In order to characterize the thermal behaviour of the oven, the fluorescence of neutral ytterbium was recorded for different currents, see Fig. 5.2b. Operating the oven at 6 A the first ion appeared after 4-5 minutes almost exclusively as a single ion, while at a higher current the probability of having two ions or more would increase dramatically. Starting with 8 A reduced the time of heating up considerably, while making it very difficult to load single ions due to the fast increase of atomic flux above the optimal region. Reducing the current after about one minute down to 6 A decreased the atomic flux to the value reached by starting at 6 A, due to the limited heat capacity of the oven.

One way to reduce the warm-up time of the oven while sustaining a low enough ionization probability for controlled reloading of single ions is to not turn down the oven current completely after loading but to keep it in a “standby mode” at lower current. Another possibility could be to control the oven with a function that starts at a high current and slowly ramps down to a stable value with optimized atomic flux.

### 5.1.2 Measured secular frequencies

For both traps the Mathieu parameters, as introduced in Ch. 2, were experimentally determined by measuring the secular frequencies of a single trapped ion. This was done using parametric excitation of the ion motion by modulating the trapping potentials at the eigenfrequencies of that motion. First, the results for the radial parameters of both traps are presented and compared to the values estimated in Sec. 3.2. Second, the results for the axial parameters of the milled trap are presented.

The excitation of the ion motion is detected by imaging the fluorescence onto the camera. When the modulation frequency approaches the resonance frequency the initially cooled ion will gain kinetic energy and start moving in a higher orbit of the trapping potential, visualized by smearing out of the fluorescence spot, see Fig. 5.3.

The modulation of the rf signal is achieved by modulating the output of the rf mixer with an additional signal generator<sup>1</sup>, as described in Sec. 4.5. Typical parameters of the modulation signal  $U_{\text{mod}}(t) = U_0 + \Delta U_{\text{mod}} \sin(\omega_{\text{mod}} t)$  are  $U_0 = 135\text{mV}$  and  $\Delta U_{\text{mod}} = 5 \dots 30\text{mV}$ , which yields a relative modulation depth of  $m_{\text{rf}} = \Delta U_{\text{mod}}/U_0 \cdot T_{\text{hel}} \sim 10^{-4}$

---

<sup>1</sup>Hameg, HMF 2550

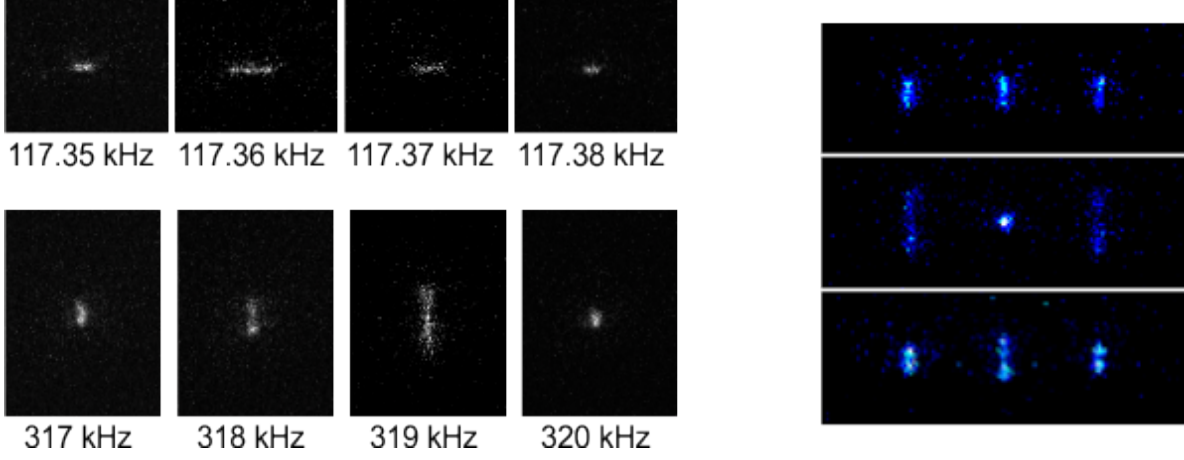


**Figure 5.3:** **Left:** Image of a single ion while scanning the frequency of the axial modulation signal (Top) and the radial modulation signal (Bottom). The heating of the ion motion is visible when modulating the trapping potentials at the secular frequencies. The resolution for this method is given as the minimum frequency step that leads to a visible change in motional amplitude. In the case of the radial excitation the pictures do not reflect the highest resolution obtained. **Right:** Parametric heating of the radial eigenmodes of a three ion crystal, distinguishable by the amplitude of the individual ions (from top to bottom: center of mass mode, “stretched” mode, “egyptian” mode).

of the trapping potential including the transmission  $T_{\text{hel}}$  of the helical resonator<sup>2</sup>. The achieved resolution for the measured resonances is between  $\sigma_\nu = 0.2 \dots 1$  kHz, depending mainly on the laser cooling efficiency and the micromotion compensation in connection with the modulation depth.

After measuring the secular frequencies as a function of the dc voltages and the rf voltage, the Mathieu parameters of the traps are obtained by fitting a function to the data having the same form as Eq. 2.4 in Sec. 2.2:

$$\omega_{\text{rad}}(U_t) = \frac{\Omega_{\text{rf}}}{2} \sqrt{p_{1,t} \cdot U_t + p_{2,t}}, \quad \text{with } p_{1,t} = \tilde{a}_t / U_t \quad (5.1)$$

and  $p_{2,t} = \tilde{a}_{\text{ax}} + 0.5 \tilde{q}^2$

$$\omega_{\text{rad}}(U_{\text{ax}}) = \frac{\Omega_{\text{rf}}}{2} \sqrt{p_{1,\text{ax}} \cdot U_{\text{ax}} + p_{2,\text{ax}}}, \quad \text{with } p_{1,\text{ax}} = \tilde{a}_{\text{ax}} / U_{\text{ax}} \quad (5.2)$$

and  $p_{2,\text{ax}} = \tilde{a}_t + 0.5 \tilde{q}^2$

$$\omega_{\text{rad}}(U_{\text{mon}}) = \frac{\Omega_{\text{rf}}}{2} \sqrt{0.5 p_{1,\text{rf}}^2 \cdot U_{\text{mon}}^2 + p_{2,\text{rf}}}, \quad \text{with } p_{1,\text{rf}} = \tilde{q} / U_{\text{mon}} \quad (5.3)$$

and  $p_{2,\text{rf}} = \tilde{a}_t + \tilde{a}_{\text{ax}}$ .

Here,  $\Omega_{\text{rf}}$  is the rf frequency and the fit parameter  $p_1$  is a function of the varied voltage and directly proportional to the corresponding Mathieu parameter. The fit parameter  $p_2$

<sup>2</sup>The helical resonator acts as a bandpass filter and the transmission  $T_{\text{hel}} = \mathcal{L}_{\text{hel}}(\nu, U_{\text{rf}}) / U_{\text{rf}}$  can be estimated with evaluating the Lorentzian function  $\mathcal{L}_{\text{hel}}(\nu, U_{\text{rf}})$ , that is fitted to the resonance of the resonator in Fig. 4.9, at the frequency  $\nu = \nu_{\text{rf}} + \nu_{\text{mod}}$ , with  $\nu_{\text{mod}} \sim 500$  kHz.

**Table 5.1:** Radial Mathieu parameters measured in the laser cut and milled traps in principle axes 1 and 2 are compared with calculated values. The values for the laser cut trap are presented in Tab. 3.3. The values for  $\tilde{q}$ , which are measured with an error of one percent, are normalized with the calibration factor  $\kappa$  of the rf pickup in order to be compared with the calculation:  $\tilde{q}/U_{\text{rf}} = \tilde{q}/U_{\text{mon}} \cdot 1/\kappa$ . This causes the uncertainty to rise to about ten percent. All parameters, measured as well as calculated are normalized with respect to the corresponding voltage.

		laser cut trap		milled trap	
		measured	calculated	measured	calculated
$\tilde{q}$	1	$(6.7 \pm 0.4) \times 10^{-5}$	$6.68 \times 10^{-5}$	$(6.5 \pm 0.5) \times 10^{-5}$	$6.94 \times 10^{-5}$
	2	$(6.6 \pm 0.4) \times 10^{-5}$	$-6.69 \times 10^{-5}$	$(6.5 \pm 0.5) \times 10^{-5}$	$-6.94 \times 10^{-5}$
$\tilde{a}_t$	1	$(1.62 \pm 0.04) \times 10^{-4}$	$1.41 \times 10^{-4}$	$(1.57 \pm 0.06) \times 10^{-4}$	$1.49 \times 10^{-4}$
	2	$(-1.51 \pm 0.04) \times 10^{-4}$	$-1.19 \times 10^{-4}$	$(-1.37 \pm 0.06) \times 10^{-4}$	$-1.26 \times 10^{-4}$
$\tilde{a}_{\text{ax}}$	1	$(-1.07 \pm 0.03) \times 10^{-5}$	$-9.64 \times 10^{-6}$	$(-8.6 \pm 0.5) \times 10^{-6}$	$-1.15 \times 10^{-5}$
	2	$(-9.99 \pm 0.02) \times 10^{-6}$	$-1.08 \times 10^{-5}$	$(-1.44 \pm 0.05) \times 10^{-5}$	$-1.27 \times 10^{-5}$

contains the Mathieu parameters corresponding to the voltages that are not changed in the measurement. The results are plotted in Fig. 5.4 and a comparison of the measured Mathieu parameters of both traps with the theoretical values is presented in Tab. 5.1.

The axial secular frequency has been measured in the milled trap. For this the modulation signal was applied directly on the central  $GND_{\text{rf}}$  electrodes<sup>3</sup>. In this way, the axial potential could be modulated in all three trapping segments without modifying the electronic configuration. Typical parameters were  $\Delta U_{\text{mod}} = 10 \dots 100$  mV and  $U_0 = 0.5 \dots 9$  V. Here, the relative modulation depth was on the order of  $10^{-4}$  as well, in this case due to the low-pass filter on the trap boards. Above axial trap frequencies of  $\approx 190$  kHz an excitation of the ion motion could not be observed. The achieved resolution of the measured frequency is  $\sigma_\nu = 20$  Hz.

The axial secular frequencies have been measured as a function of the dc voltages  $U_{\text{ax}}$  and  $U_t$  and the trap parameters have been derived from:

$$\omega_{\text{ax}}(U_{\text{ax}}) = \frac{\Omega_{\text{rf}}}{2} \sqrt{p_1 \cdot U_{\text{ax}} + p_2} \quad \text{with} \quad p_1 = \tilde{a}_{\text{ax}}/U_{\text{ax}}, \quad p_2 = a_{\text{stray}}, \quad (5.4)$$

$$\omega_{\text{ax}}(U_t) = \frac{\Omega_{\text{rf}}}{2} \sqrt{p_1 \cdot U_t + p_2} \quad \text{with} \quad p_1 = \tilde{a}_t/U_t, \quad p_2 = \tilde{a}_{\text{ax}} + a_{\text{stray}}. \quad (5.5)$$

Here, the Mathieu parameters are derived in the same way as for the radial frequencies. In the case of the axial voltage two fits are applied, one with the second parameter fixed at zero and the other one with  $p_2 = a_{\text{stray}}$  as a free parameter accounting for possible stray fields. With  $U_t = 0$  no other contribution to the axial trapping potential

<sup>3</sup>The connection with the dc control unit was cut and an adapter was built to directly connect the signal generator with the multi-core cable.

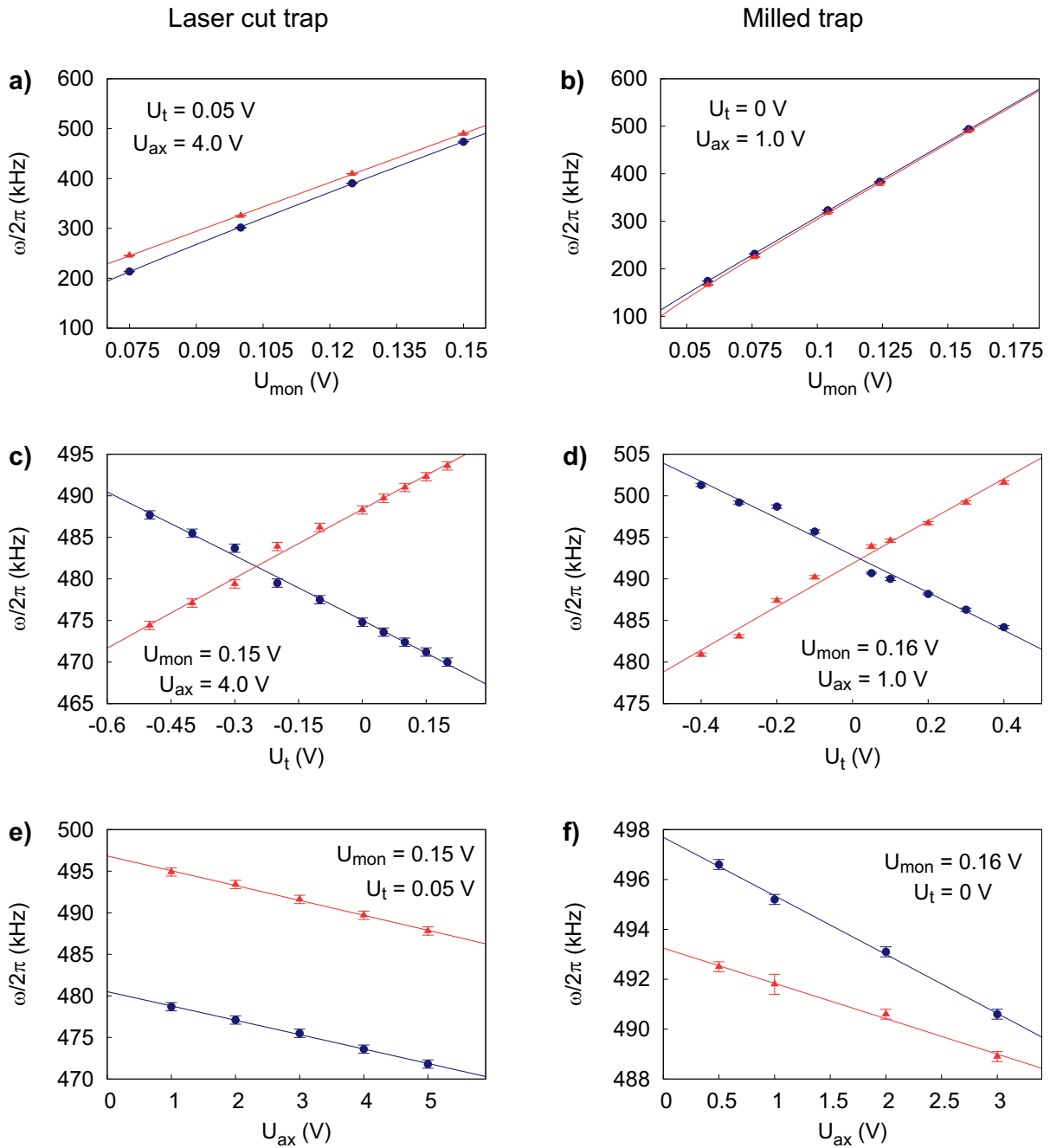


**Figure 5.4:** Secular frequencies of a single  $^{172}\text{Yb}^+$  ion measured in the laser cut trap (left) and the milled trap (right) by modulation of the rf potential. Both dc voltages as well as the rf voltage are varied to directly determine the corresponding Mathieu parameters. Shown are the measured resonances in both radial axes (red triangles and blue circles) as well as the fitted functions given in Eqs. 5.1 to 5.3. The rf frequencies are  $\Omega_{\text{rf}} \approx 2\pi \times 25.66$  MHz for the laser cut trap and  $\Omega_{\text{rf}} \approx 2\pi \times 25.42$  MHz for the milled trap.

**Table 5.2:** Axial Mathieu parameters measured in the milled trap are compared with the calculated values presented in Tab. 3.3.

	milled trap	calculated
$\tilde{a}_{\text{ax}}$	$(2.461 \pm 0.004) \times 10^{-5}$	$2.05 \times 10^{-5}$
$\tilde{a}_{\text{t}}$	$(-2.4218 \pm 0.0007) \times 10^{-5}$	$-2.09 \times 10^{-5}$

is expected. However, the better agreement of the data with the function with two parameters indicates the presence of an additional dc potential with negative curvature in the direction of the trap axis<sup>4</sup>. The fit yields a value of  $a_{\text{stray}} = (-9.00 \pm 0.08) \times 10^{-6}$ .

The results are shown in Fig. 5.5 and compared with the calculated values in Tab. 5.2.

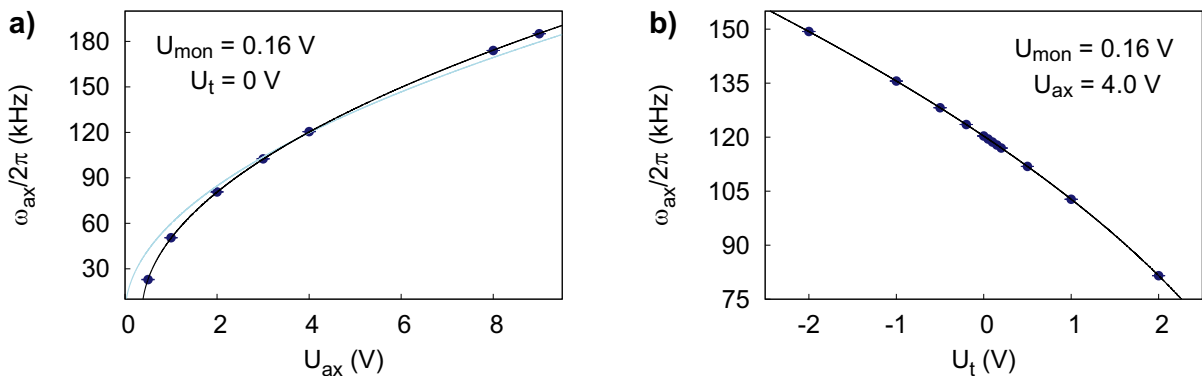


**Figure 5.5:** Measured axial secular frequencies as a function of  $U_{\text{ax}}$  and  $U_{\text{t}}$ . **a)** A fit to the data using Eq. 5.4 yields  $\tilde{a}_{\text{ax}}/U_{\text{ax}}$ . The fit including the second parameter  $a_{\text{stray}} = (-9.00 \pm 0.08) \times 10^{-6}$  (black) matches the data, in contrast to the fit without an assumed extra contribution (light blue). **b)** A fit to the data (black) using Eq. 5.5 yields  $\tilde{a}_{\text{t}}/U_{\text{t}}$ . The second fit parameter amounts to  $p_2 = (8.957 \pm 0.001) \times 10^{-5}$ .

## 5.2 Photon-correlation spectroscopy

### 5.2.1 Method

A single  $^{172}\text{Yb}^+$  ion is loaded into the trap to measure residual micromotion by photon-correlation spectroscopy [38]. This technique measures the rf field induced motion of the ion via its 1st order Doppler-shift on a broad atomic line with natural linewidth  $\Gamma_{\text{nat}}$ , see Fig. 5.6.

<sup>4</sup>In principal, the residual axial rf field gives an additional contribution as well. But the corresponding ponderomotive potential has a positive curvature, unlike the fitted value. Furthermore, according to the measured axial field, see Sec. 5.3, this contribution is  $\nu_{\text{ax}}(U_{\text{rf}}) \approx 0.6$  kHz

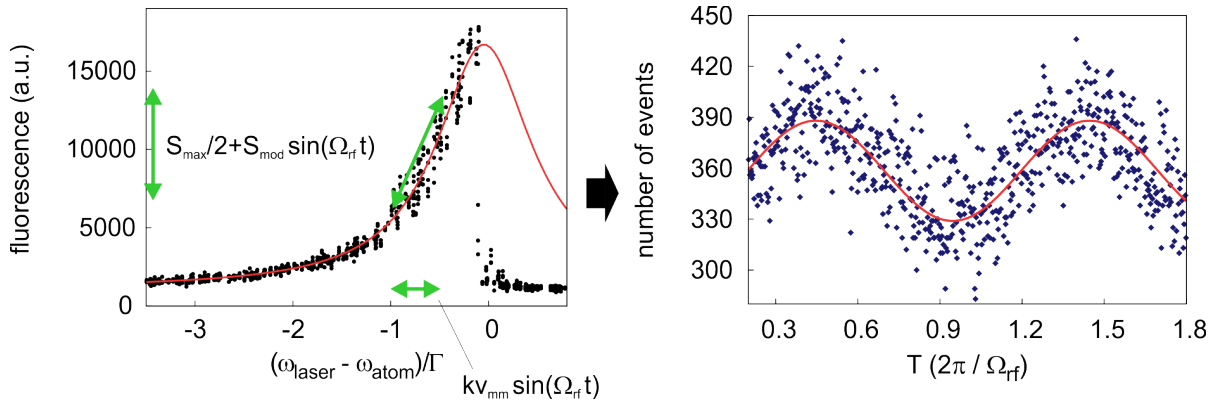


**Figure 5.6:** Intuitive schematic of the photon-correlation technique. **Left:** A scan of the cooling laser (black dots) on a broad atomic line, fitted with a Lorentzian function (red line) to determine the width  $\Gamma$ . The rf field induced micromotion  $v_{\text{mm}}$  modulates the fluorescence  $S_{\text{det}}$  of a trapped ion on this atomic line due to the first-order Doppler shift. The modulation of the signal  $S_{\text{mod}}$  is directly proportional to the slope of the atomic line. In the case of half of the maximum fluorescence the slope is  $1/\Gamma$ . **Right:** The scattered photons are sorted by relative phase to the rf signal and counted in a histogram (blue dots). The modulation is obtained from fitting a harmonic function (red line) to the data.

In order to resolve the weak modulation of the ion fluorescence at the trap drive frequency, its scattering rate is correlated with the phase of the rf trap voltage. A time-to-amplitude-converter (TAC) generates pulses with a height dependent on the time  $T$  between a START-signal, triggered by the detection of a photon by the PMT, and a STOP-signal triggered by the rf voltage of the trap. A multi-channel-analyzer yields a histogram of these pulses sorted by height and thus, by time difference  $T$ , see an example in Fig. 5.6b. Thereby, the modulation amplitude of the ion's fluorescence at the trap frequency  $\Omega_{\text{rf}}$  is observed. A detailed description of the method can be found in [38].

For each measurement, the data acquisition time is 30 s. The average photon count rate at a detuning of  $\omega_{\text{laser}} - \omega_{\text{ion}} = -\Gamma/2$  is about  $10\,800\text{ s}^{-1}$ , including a background of about  $1800\text{ s}^{-1}$ .

Using the laser beams in H1, H2 and V, respectively, the micromotion can be measured in all dimensions. The velocity amplitude of rf induced ion motion  $v_{\text{mm}}$  is evaluated using the linearization of the line profile around  $\omega_{\text{laser}} - \omega_{\text{ion}} = -\Gamma/2$ , which is a valid approximation for  $k v_{\text{mm}} \ll \Gamma$ , with the wave vector  $k$ . In this case, the signal contribution  $S_{\text{det},i}$  of each beam  $i$  can be written as

$$S_{\text{det},i} = \frac{S_{\text{max},i}}{2} + S_{\text{mod},i} \sin(\Omega_{\text{rf}}t + \varphi_i), \quad \text{with } i=\text{H1,H2,V}, \quad (5.6)$$

where  $S_{\text{max},i}/2$  is the ion's fluorescence at  $\omega_{\text{laser}} - \omega_{\text{ion}} = -\Gamma/2$ , which corresponds to half of the maximum fluorescence for a (saturation-broadened) Lorentzian probability distribution.  $S_{\text{mod},i}$  is the fluorescence modulation amplitude and  $\varphi_i$  is the phase of the signal relative to the rf voltage. To improve the fit of the data, the frequency of the rf

trigger signal is  $\Omega_{\text{rf}}/2$ , so that the data set spans two rf periods, i.e.  $T = 0 \dots 4\pi/\Omega_{\text{rf}}$ . From the individual measurements along laser beams H1, H2 and V, the velocity components along the trap axes are extracted using:

$$\frac{k v_{\text{mm},y}}{\Gamma_{\text{nat}}} = \frac{S_{\text{mod},V} \sqrt{1 + s_V}}{(S_{\text{max},V} - S_{\text{b},V}) f_c}, \quad (5.7)$$

$$\frac{k v_{\text{mm},x}}{\Gamma_{\text{nat}}} = C_x \sqrt{A^2 + B^2 + 2AB \cos(\varphi_{\text{H2}} - \varphi_{\text{H1}})}, \quad (5.8)$$

$$\frac{k v_{\text{mm},z}}{\Gamma_{\text{nat}}} = C_z \sqrt{A^2 + B^2 - 2AB \cos(\varphi_{\text{H2}} - \varphi_{\text{H1}})}, \quad (5.9)$$

$$\text{with } C_{x,z} = \frac{1}{2 \cos \theta_{x,z} f_c} \quad \text{and} \quad A, B = \frac{S_{\text{mod},\text{H1,H2}} \cdot \sqrt{1 + s_{\text{H1,H2}}}}{S_{\text{max},\text{H1,H2}} - S_{\text{b},\text{H1,H2}}}.$$

Here,  $k = 2\pi/369.5 \text{ nm}$  and  $\theta_x = 65^\circ$  and  $\theta_z = 25^\circ$  are the projection angles of the laser beams H1 and H2 to the trap axes x and z, respectively. Saturation broadening of the atomic line is taken into account by the individual saturation parameters  $s_i$  of each laser beam. The background  $S_{\text{b},i}$  due to stray light of the detection laser is accounted for as well.

In addition, the amplitude of the measured signal is corrected by a factor  $f_c$ , due to the finite lifetime of the excited state of the ion. Only when the lifetime of the excited state is much shorter than the modulation period of the signal ( $\tau \ll T_{\text{rf}}$ ), the full signal modulation  $m_0 = S_{\text{mod}}^{(0)}/S_0$  is observed. In general, the fluorescence of an ion, when excited by a periodic signal, obeys the differential equation  $\dot{S}(t) = \tau^{-1} S(t) + S_{\text{drive}}(t)$ , with a periodic term  $S_{\text{drive}}(t)$  [56]. The general solution to this equation is:

$$S(t) = e^{-t/\tau} \left( c_1 + \int_{-\infty}^t S_{\text{drive}}(t') e^{t'/\tau} dt' \right), \quad (5.10)$$

which consists of a fast exponential decay and the damped response to the modulation. For the fluorescence of a laser-cooled ion with micromotion, this modulation is  $S_{\text{drive}}(t) = S_0 + S_{\text{mod}}^{(0)} \sin(\Omega_{\text{rf}} t)$ , with  $S_{\text{mod}}^{(0)} \propto |\vec{k} \cdot \vec{v}_{\text{mm}}|$ . For times larger than the natural decay time  $\tau$ , (5.10) gives:

$$\begin{aligned} S(t) &= \tau S_0 + S_{\text{mod}}^{(0)} \cdot \frac{\tau^{-1} \sin(\Omega_{\text{rf}} t) - \Omega_{\text{rf}} \cos(\Omega_{\text{rf}} t)}{\tau^{-2} + \Omega_{\text{rf}}^2}, \\ &= \tau S_0 + S_{\text{mod}}^{(0)} \cdot (\tau^{-2} + \Omega_{\text{rf}}^2)^{-1/2} \cdot \sin(\Omega_{\text{rf}} t + \varphi_i). \end{aligned} \quad (5.11)$$

From this the modulation  $m_{\text{det}}$  of the detected fluorescence is derived to be

$$m_{\text{det}} = \frac{S_{\text{mod}}^{(0)} \cdot (\tau^{-2} + \Omega_{\text{rf}}^2)^{-1/2}}{\tau S_0} = m_0 \cdot f_c, \quad (5.12)$$

giving a reduction in contrast compared to the modulation  $m_0$  of

$$f_c = \frac{1}{\sqrt{1 + (\Omega_{\text{rf}} \tau)^2}}. \quad (5.13)$$

With a lifetime  $\tau = 8 \text{ ns}$  [50], this correction term amounts to  $f_c = 0.61$  for our system.

The finite saturation parameter  $s_i \approx 0.6$  of each laser beam leads to a reduction of the measured micromotion velocity amplitude of about 26%. It is evaluated before the measurement by scanning the cooling laser over the resonance for each beam and fitting a Lorentzian profile to the scan. The fit gives the effective linewidth  $\Gamma$  and hence the saturation parameter for each laser beam with a systematic relative uncertainty of about 8%, which is the major contribution to the systematic uncertainty of the micromotion amplitude  $v_{\text{mm},i}$ . In comparison, the uncertainty in the angles of the laser beams to the trap axes are negligible and are therefore ignored.

Great care is taken to correctly subtract the background signal due to laser stray light from the fitted offset  $S_{\text{max},i}/2$ . The detection laser itself contributes about 5 – 10% to the background. In the case of measuring micromotion along V, laser beam H1 is present during the measurement to compensate axial heating of the ion. For this purpose the power in beam H1 is reduced by a factor of 14 and makes no detectable contribution to the modulation amplitude. A constant offset is subtracted from  $S_{\text{max},V}/2$  to account for the additional background from H1.

### 5.2.2 Sensitivity of the method

Another error contribution to the measured micromotion is found to be due to frequency and intensity fluctuations. The latter contribute as well, since the line shape and therefore the slope depend on the saturation parameter. These fluctuations occur on a time scale of minutes and cause a scatter of separate measurements, which usually happen in an acquisition time of 30 s. The corresponding error is estimated by repeatedly measuring the micromotion at fixed experimental parameters and evaluating the scatter of the data as the standard deviation. The results are shown in Fig. 5.7 for H1, in which the data are plotted against the average PMT signal.

From the measured signal alone it cannot be distinguished clearly between frequency and intensity fluctuations, since both lead to different average ion fluorescence. Monitoring the power of the cooling laser shows, that the intensity usually stays constant well within ten percent over a measurement period of several hours. Besides that, as the laser frequency slowly drifts with the wavemeter, the average fluorescence and therefore the fitted offset changes for individual measurements. On longterm scale these drifts are compensated by adjusting the set value of the wavemeter, such that the monitored fluorescence returns to the right value<sup>5</sup>.

From this measurement a standard deviation of  $\sigma_{\text{laser}} = 0.01$  accounting for the relative amplitude fluctuations is determined. This value is added quadratically to the error of the measured micromotion velocity as a statistical uncertainty that appears due to the statistical nature of the underlying systematic fluctuations. It is also a conservative estimate and not adjusted each time the performance of the laser or the wavemeter changes. In the case of the vertical laser beam this value is added directly.

---

<sup>5</sup>The characterization of the wavemeter has been shown in Sec. 4.2. With the stable laser being continuously available, it is also possible to monitor the wavemeter drift directly instead of through the fluorescence.



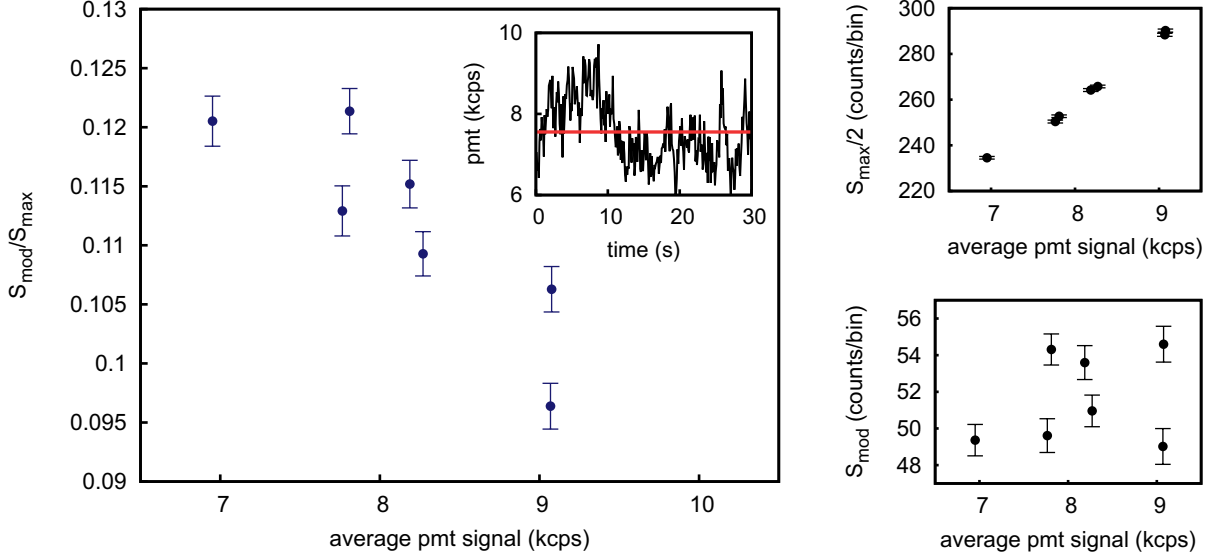


**Figure 5.7:** **Left:** Repeated micromotion measurement in H1 correlated with the average fluorescence (inset). The trap parameters are  $U_{\text{rf}} \approx 810 \text{ V}$ ,  $U_{\text{ax}} \approx 4 \text{ V}$  and  $U_{\text{t}} \approx 0.05 \text{ V}$ . The laser power is  $P_{\text{H1}} \approx 3 \mu\text{W}$ . **Right:** The fitted offset  $S_{\text{max}}/2$  exhibits a linear dependence, whereas the modulation  $S_{\text{mod}}$  is constant within the error. The uncertainty of the measurement is evaluated as the sample standard deviation and amounts to 0.01, which is added as an independent contribution to the error of the measured micromotion velocity  $v_{\text{mm}}$ .

For the horizontal beams the projection on the corresponding coordinate axis is taken into account. The total error  $\sigma_{\text{tot},i}$  is then:

$$\sigma_{\text{tot},i} = \sqrt{(\sigma_{v_{\text{mm},i}})^2 + \left(\frac{\sigma_{\text{laser}}}{\cos \theta_i}\right)^2}. \quad (5.14)$$

The error  $\sigma_{v_{\text{mm},i}}$  is evaluated with Gaussian error propagation from Eqs. (5.7) to (5.9) and includes the uncertainty of the effective linewidth  $\Gamma$ , described in the preceding section, as well as the fit error.

### 5.2.3 Evaluation of the rf field and resolution

The amplitude of the rf trapping field is calculated from the measured micromotion by comparing the kinetic energy<sup>6</sup> of the micromotion with the potential energy of the ion in the rf trapping potential:

$$\frac{1}{4}mv_{\text{mm},i}^2 = \frac{e^2 E_{\text{rf},i}^2}{4m\Omega_{\text{rf}}^2} \quad \text{with } i = x, y, z \quad (5.15)$$

$$\Rightarrow E_{\text{rf},i} = \frac{v_{\text{mm},i} m \Omega_{\text{rf}}}{e}. \quad (5.16)$$

<sup>6</sup>The kinetic energy of the micromotion is given by the time averaged squared velocity, which is half the measured squared velocity amplitude  $v_{\text{mm}}$ :  $\langle v^2 \rangle = \int_0^{T_{\text{rf}}} v_{\text{mm}}^2 \cos^2(\Omega_{\text{rf}} t) dt = \frac{1}{2} v_{\text{mm}}^2$

In the same way the error for the rf field is obtained.

Summarizing, the resolution of the photon-correlation spectroscopy is evaluated in units of the rf electric field. The highest resolution is obtained for the micromotion y component measured along laser beam V with a scatter of  $\sigma_{\text{rf},y} = 21 \text{ V/m}$  due to the uncertainty  $\sigma_{\text{laser}}$ . For the measurements along the trap axis this uncertainty is  $22 \text{ V/m}$ . The lowest resolution is obtained in x direction with  $\sigma_{\text{rf},x} = 49 \text{ V/m}$ . The fit to the data contributes an additional statistical uncertainty of  $8 \text{ V/m}$ .

As an example, Fig. 5.8 shows the histograms of two measurements of the radial micromotion component along the y-axis of a single ion as measured by the laser beam along V.

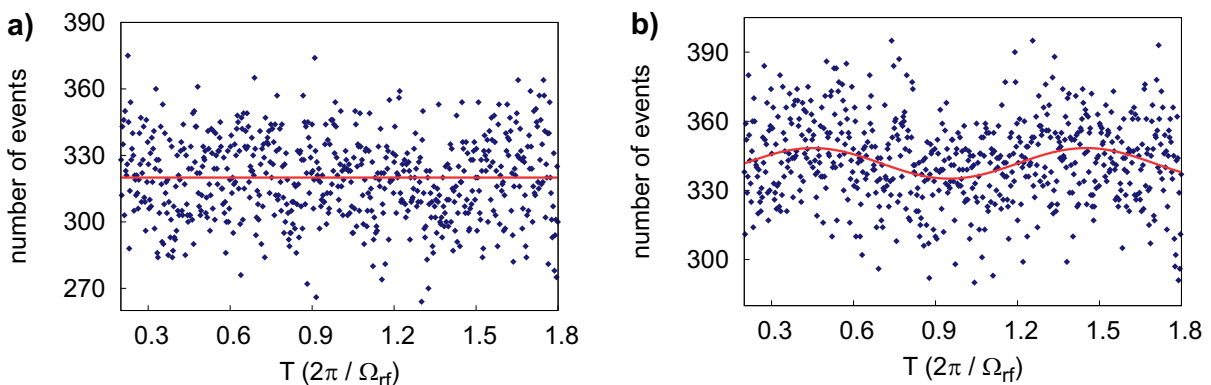


**Figure 5.8:** Photon-correlation signal of micromotion along y direction as measured with vertical laser beam (V). The acquisition time is 30 s. a) Ion with optimized micromotion. Restricting the phase to  $-\pi/2 < \varphi_i < \pi/2$  the fit yields  $S_{\text{mod}}/S_{\text{max}} = 0 \pm 0.0017$ . b) Ion shifted by  $\Delta U_{\text{ec}} = 5.8 \text{ mV}$  (corresponding to  $\Delta x = 57 \text{ nm}$ ) in x direction. The red line is a sine fit to the data with  $S_{\text{mod}}/S_{\text{max}} = 0.011 \pm 0.0016$ .

As shown in Fig. 5.8, an electric field of  $\Delta E_x = 0.9 \text{ V/m}$ , corresponding to  $\Delta U_{\text{ec}} = 5.8 \text{ mV}$ , has to be applied to produce a detectable micromotion along the y-axis. This corresponds to an rf field amplitude of  $E_{\text{rf},x} = (51 \pm 23) \text{ V/m}$ , or an excess micromotion amplitude of  $1.1 \text{ nm}$ . With  $(\Delta\nu/\nu)_{\text{mm}} = -\langle v_{\text{mm}}^2 \rangle / 2c^2$ , this gives a relative frequency shift due to time dilation of  $-8.5 \times 10^{-20}$ . Here, the resolved rf field is limited only by the resolution of the dc voltage control on the electrodes that move the ion radially. It is worthwhile mentioning that the rf field induced Stark shift is about an order of magnitude smaller than the shift due to time dilation, as shown in [19], and therefore negligible in this work.

## 5.3 Micromotion in the trap

### 5.3.1 Radial micromotion

To characterize and test the photon-correlation method quantitatively, a single ion was first shifted in both radial directions of the trap, where the strong rf quadrupole potential

dominates and its field gradients can be determined accurately from the measurements of the secular frequencies. In Fig. 5.9a the micromotion measurement is shown for an ion shifted along the  $y$  direction and in Fig. 5.9b for an ion shifted along the  $x$  direction.

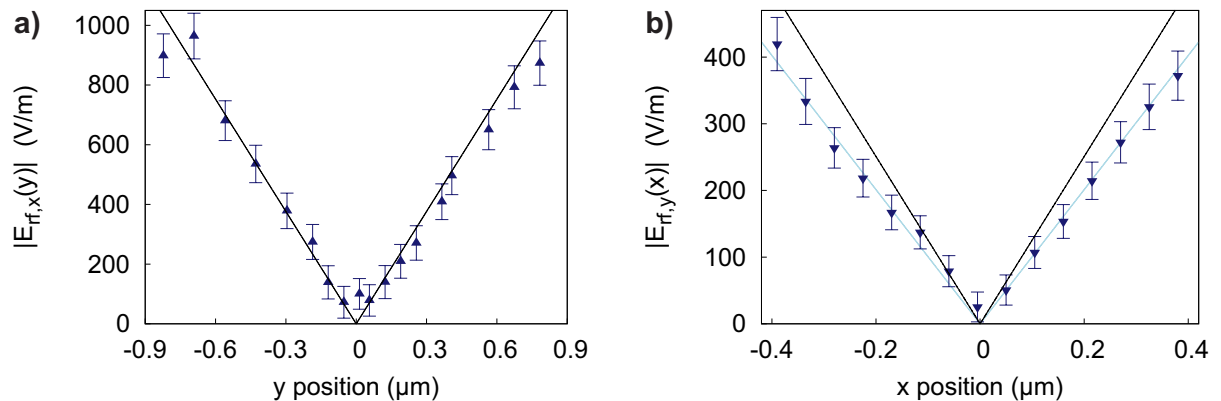


**Figure 5.9:** RF field as function of ion displacement in radial directions  $x$  and  $y$ . To check the consistency of the measured micromotion amplitudes, expected rf field amplitudes have been calculated from the measured radial secular frequencies (solid lines). In b) the measured field gradient is obtained by a linear fit (light blue line) to estimate the deviation from the calculated value.

The graphs show the measured rf electric field component perpendicular to the direction of the ion shift as a function of the ion position in the trap. The position of the ion is calculated according to Eq. 2.12 using the measured radial secular frequencies  $\omega_i$  and the calculated dc electric fields  $E_i$  applied by changing  $U_{tc}$  and  $U_{ec}$ , see Tab. 3.4. The secular frequencies have been measured in Sec. 5.1.2 in the direction of the principal axes. Taking the average of these frequencies leads to a good approximation for the actual frequency in  $x$  and  $y$  direction used here, which amounts to  $\omega_{x,y} \approx 2\pi \times 482$  kHz.

For comparison, the rf electric field obtained by the FEM calculations is plotted together with the measured data as a function of the ion position. The measurement of the  $x$  component of the field is in good agreement with the calculation. However, the  $y$  component shows a deviation, which is evaluated by fitting the function  $|E_{rf,y}(x)| = \nabla E_{rf,y} |x|$  to the data, yielding a field gradient of  $\nabla E_{rf,y} = (1.01 \pm 0.01) \times 10^9$  V m $^{-2}$ , which gives a deviation of about 25 % from the calculated value.

This discrepancy can be explained by the fact that the Rogers 4350B<sup>TM</sup> boards are elastic. Pictures taken from the assembled trap stack show that the outer compensation boards slightly bend away from the rf trap boards in the center and therefore have a larger distance to the trap center in the  $x$  direction. This leads to a decreased static electric field at a given compensation voltage  $U_{ec}$ . An FEM calculation, in which the distance between the compensation and trap boards is varied, shows a decrease of the dc field in  $x$  direction of about 30 % for an increase of the electrode distance from the spacer thickness  $t_{sp} = 250$   $\mu$ m to about 500  $\mu$ m, which is reasonable looking at the taken pictures, see Fig. 5.10a.

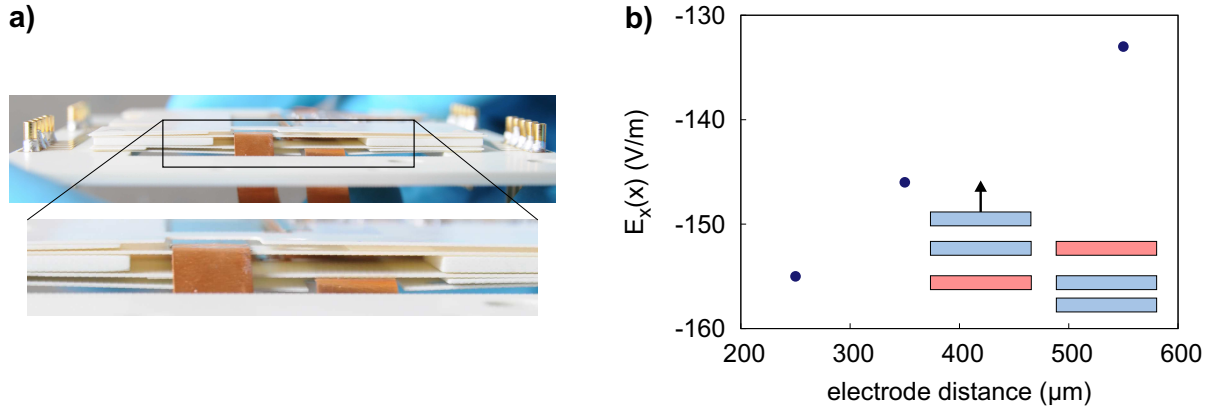


**Figure 5.10:** **a)** Picture of the laser cut trap from the rf side. The compensation boards are bent away from the trap boards in the center compared to the edges, where the distance is given by the thickness of the spacers. **b)** In FEM calculations, one compensation electrode array is shifted away from the rf ground electrodes, the compensation voltage is  $U_{ec} = 1$  V. From a distance equal to the spacer thickness of  $250 \mu\text{m}$  to about  $500 \mu\text{m}$  the field in the trap center decreases by about 15%. With one or two compensation boards bent away, the x component of the compensation field  $E_{ec}$  can decrease to about 30%, which gives a possible explanation for the discrepancy between measured data and calculation in Fig. 5.9.

On the other hand, along the y direction the ion is shifted by applying  $U_{tc}$  on the rf ground electrodes on the quadrupole trap boards. As these electrodes are more rigidly machined from one continuous wafer and measured secular frequencies have confirmed the expected rf quadrupole geometry, no relevant deviations in the applied dc fields, created by  $U_{tc}$ , are expected here. This gives a strong argument for the good agreement between the measurement and the calculations in the case of the vertical ion shift, where  $E_{rf,x}$  is measured.

### 5.3.2 Axial micromotion

To measure residual rf fields, a single ion was shifted in the direction of the trap axis and the micromotion was measured in all dimensions. The laser beams have been adjusted while shifting the ion, in order to prevent systematic uncertainties due to a change in the intensity at the ion position.

The axial rf field is shown in Fig. 5.11 and compared to FEM calculations, that include the contribution to the rf electric field due to the finite length of the trap as well as the slits between the electrodes, see Fig. 5.12.

In the calculations the dominant contribution to the axial field component is due to the electrode gaps with an estimated field gradient of about  $1.5 \times 10^3 \text{ V m}^{-2} U_{rf}^{-1}$ . Compared to this, the contribution due to the finite length of the trap is much lower with about  $5.1 \text{ V m}^{-2} U_{rf}^{-1}$ . Adding up these values and multiplying it with the measured rf voltage of about 810 V a gradient of  $\nabla E_{z,\text{calc}} = 1.22 \times 10^6 \text{ V m}^{-2}$  is compared to the

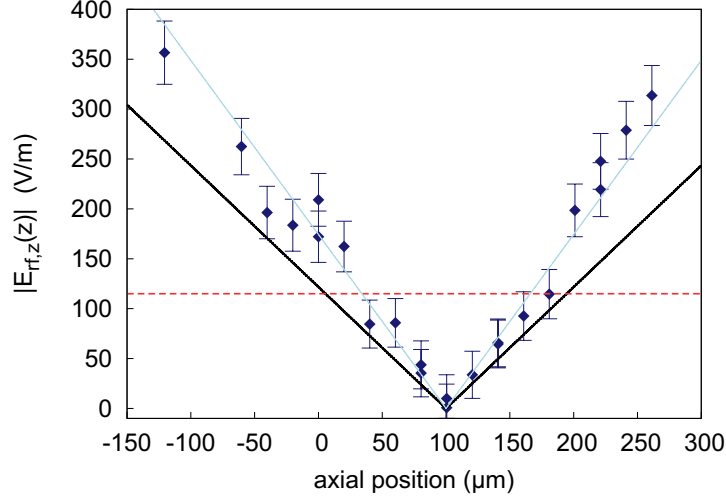


**Figure 5.11:** Residual axial rf electric field along trap axis derived from measured micromotion amplitude (diamonds) compared to axial rf field estimated from FEM calculations (solid black line), yielding a gradient of  $\nabla E_{z,\text{calc}} = 1.22 \times 10^6 \text{ V m}^{-2}$  at  $U_{\text{rf}} = 810 \text{ V}$ . The blue line indicates the function fitted to the data:  $E_{\text{rf},z}(z) = \nabla E_{\text{rf},\text{fit}} |z - z_0|$ , with  $\nabla E_{\text{rf},\text{fit}} = (1.74 \pm 0.05) \times 10^6 \text{ V m}^{-2}$  and  $z_0 = 100 \mu\text{m}$ . The dashed line indicates the rf field, for which the relative frequency shift induced by micromotion is smaller than  $10^{-18}$  for an indium ion optical clock. The zero axial position corresponds to the ion position for  $U_{\text{ax},1} = U_{\text{ax},3} = 4 \text{ V}$ , where the measurement was initiated.

measured value of  $\nabla E_{z,\text{fit}} = (1.74 \pm 0.05) \times 10^6 \text{ V m}^{-2}$ , see Fig. 5.11.

Alignment and machining uncertainties and their effect on the rf field have been investigated in [19] and presented in Ch. 2. According to that, variations in the width of the slits between the electrodes due to machining tolerances would affect the measured field gradient and can be an explanation for the slightly larger measured rf fields.

In order to determine the residual field in all dimensions, the radial components have been measured together with the axial component, see Fig. 5.13. With this an rf field of 115 V/m or below could be verified in the range of  $40 < z < 170 \mu\text{m}$  in all dimensions.

The sudden change in the range  $z \approx 0 \dots 75 \mu\text{m}$  in both graphs can be explained by changes of the trapping potential over a two-day measurement after compensating the micromotion only in the beginning. These can be caused by stray fields due to slowly varying patch potentials over night. Since the measurements were done in the central segment, the adjacent loading segment, which provides axial confinement could also have been contaminated when loading a new ion.

Besides that, a deviation of  $100 \mu\text{m}$  was observed between the ion position with minimum micromotion and the average ion position for symmetric axial dc voltages  $U_{\text{ax},1} = U_{\text{ax},3} = 4.0 \text{ V}$ , which is at  $z = 0$  in Fig. 5.11. This can be due to angular misalignment of the trap boards, leading to an offset in the axial rf field in the trapping region [19], machining tolerances of the electrode notches or dc stray fields, shifting the ion from their average position in the axial trapping potential. These effects are not distinguishable in the present setup.

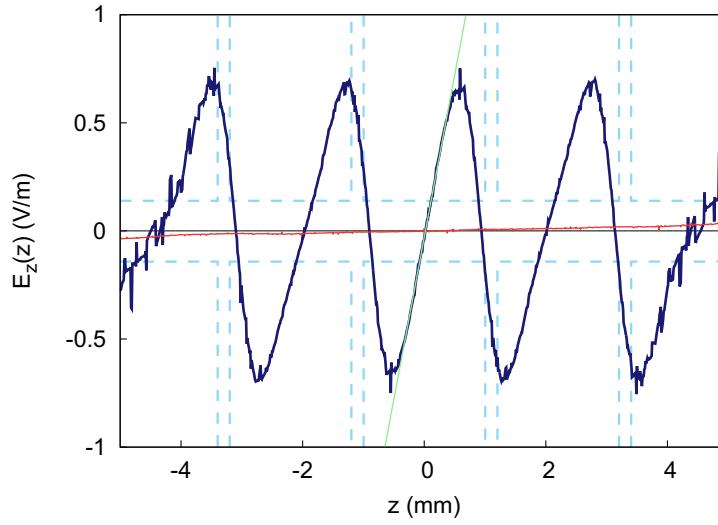


**Figure 5.12:** Calculated axial rf field of the laser cut trap for an rf voltage  $U_{\text{rf}} = 1 \text{ V}$ . Compared are the contributions of the electrode gaps (dark blue line) with the contribution due to the finite length of the electrodes (red line). A linear fit (green line) to the linearly increasing field in the trap center yields a value for the field gradient of  $(1.50 \pm 0.01) \times 10^3 \text{ V m}^{-2} U_{\text{rf}}^{-1}$ , which corresponds to the black line in Fig. 5.11 for  $U_{\text{rf}} = 810 \text{ V}$ . The finite length leads to a field gradient of about  $(5.11 \pm 0.03) \text{ V m}^{-2} U_{\text{rf}}^{-1}$ . The dashed light blue lines indicate the trap trap electrodes as used in the calculations.

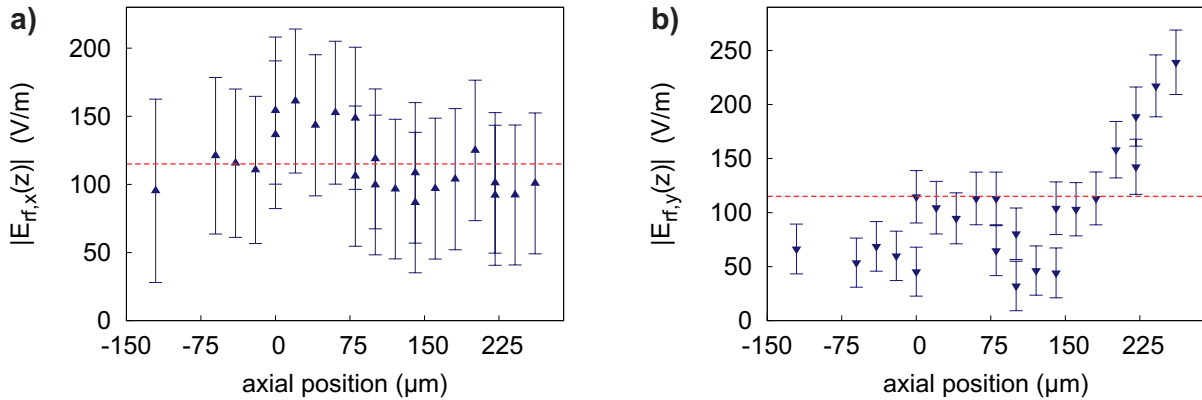


**Figure 5.13:** Residual radial rf field along the trap axis measured together with the axial field component. The x component is shown in a), the y component is shown in b). The measurements are done over two days, with the same trap parameters and compensation voltages. The offset of the data between  $z \approx 0 \dots 75 \mu\text{m}$  compared to the rest can be due to a slow drift in the compensation over night. The red line again indicates the level at which the micromotion induced fractional frequency shift amounts to  $1 \times 10^{-18}$ .

For optical clock operation with  $\text{In}^+$  ions, the amplitudes of axial rf fields need to be  $|E_{\text{rf}}| < 115 \text{ V/m}$  to guarantee a small enough fractional frequency shift due to time dilation of  $|(\Delta\nu/\nu)_{\text{mm}}| = 4E_{\text{rf}}^2 e^2 / (m^2 \Omega_{\text{rf}}^2) \leq 1 \times 10^{-18}$ . In the laser cut trap a length of  $\approx 130 \mu\text{m}$  is found for an rf voltage of  $810 \text{ V}$ , within which this condition is fulfilled. At full rf amplitude of  $1500 \text{ V}$ , this length is reduced by about a factor of two, allowing space for about 12 trapped ions.

For comparison the axial rf field has been measured in the milled trap as well. In Fig. 5.14 the results are compared to the measurement and the FEM calculation in the laser cut trap.

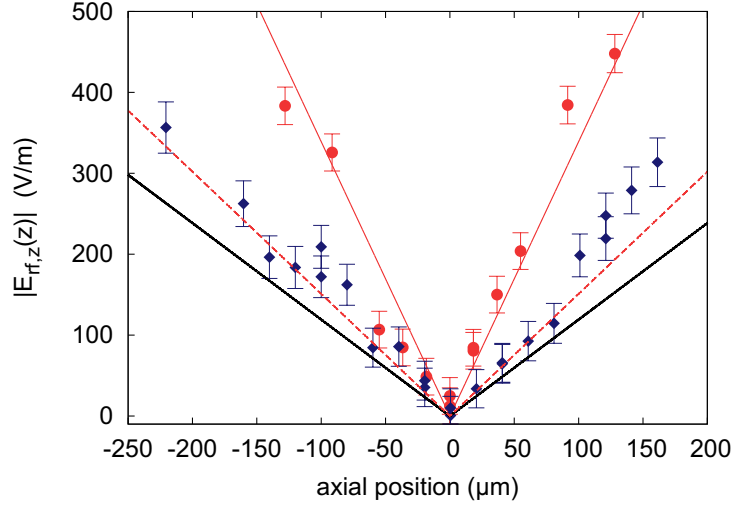


**Figure 5.14:** Residual axial rf field measured in milled trap (red circles) and compared to the measurements (blue diamonds) and calculations in the milled trap (dashed red line) and in the laser cut trap (black line). The data are fitted (solid red line) with  $|E_{\text{rf},z}(z)| = \nabla E_{\text{rf},z} |z|$  yielding a field gradient  $\nabla E_{\text{rf},z} = (3.4 \pm 0.2) \times 10^6 \text{ V m}^{-2}$ , which is a factor of two higher than in the laser cut trap.

A linear fit to the data yields a field gradient in the milled trap of  $\nabla E_{\text{rf},z} = (3.4 \pm 0.2) \times 10^6 \text{ V m}^{-2}$ , which is a factor of two higher than the gradient measured in the laser cut trap. An FEM calculation of the milled trap was done using the measured values for the slit width and segment length, see Sec. 3.3. A fit to the numerical data yields an axial field gradient of  $\nabla E_{\text{rf},z} = (1.56 \pm 0.01) \times 10^6 \text{ V m}^{-2}$  at  $U_{\text{rf}} = 810 \text{ V}$ . Here, the thicker wafers reduce the axial field component, whereas the larger gaps between the electrodes increase the axial field (see Sec. 2.4 and [19]), which causes the slight difference to the laser cut trap for a geometry without machining tolerances.

Comparing the two traps, it is found that the laser cut trap (milled trap) exhibits an increase in axial field gradient of about a factor 1.4 (1.8). A possible explanation for this difference can be machining quality of the milled wafers, as demonstrated in Fig. 3.6, leading to higher uncertainty of the slit width and therefore a larger contribution to the axial rf field. In fact, the scatter of the measured slit widths is about a factor of two worse for the milled trap compared to the laser cut trap.

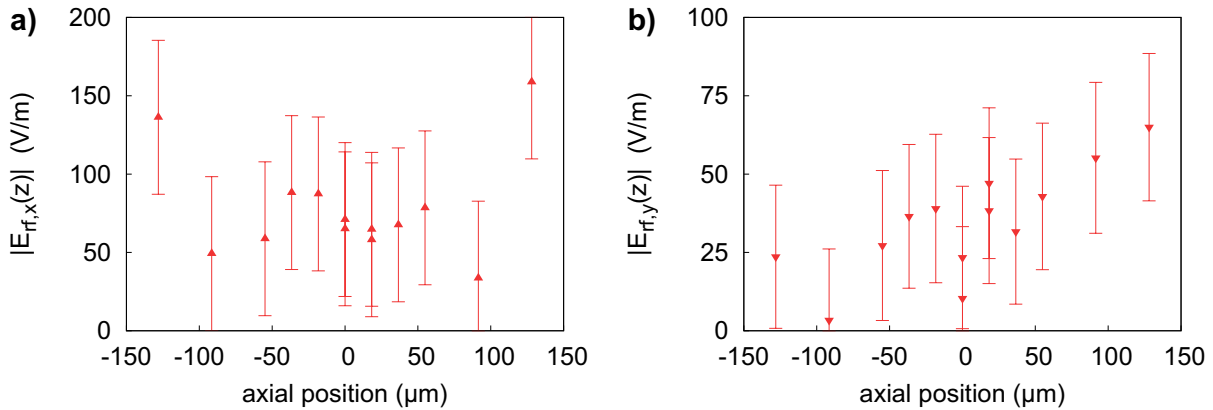


**Figure 5.15:** Residual radial rf field measured in the milled trap together with the axial component. In a) the x component is shown and in b) the y component. As in the laser cut trap, here the radial field is below the value of  $115 \text{ V m}^{-1}$  in the region of the axial zero crossing.

As a control measurement the radial components of the rf field have been measured together with the axial field in the milled trap, see Fig. 5.15.

### 5.3.3 Longterm analysis of micromotion compensation

In the laser cut trap the changing of micromotion compensation over time has been recorded in different measurements. One was carried out over several hours within one day including reloading the ion twice, in order to determine changes of the micromotion compensation due to contamination of the trap electrodes from the atomic beam. Compared are measurements in the loading segment and in the central segment: see Fig. 5.16. The trap parameters are  $U_{rf} \approx 810 \text{ V}$ ,  $U_t \approx 0.05 \text{ V}$ ,  $U_{ax} \approx 4 \text{ V}$ ,  $U_{tc,3} \approx -0.0552 \text{ V}$  and  $U_{ec,3} \approx 0.3497 \text{ V}$ ,  $U_{tc,2} \approx -0.0060 \text{ V}$  and  $U_{ec,2} \approx 0.6870 \text{ V}$ . The saturation parameter in each cooling laser beam is  $s \approx 0.6$ .

Plotted are the micromotion components in all dimensions in both segments, as well as the oven current to indicate the loading events. First, the data in the loading segment are discussed.

For the vertical component, which is sensitive to ion shifts in horizontal direction, a slow drift over about four hours is observed. The other two components do not exhibit any drift. At the beginning of the measurement, the oven was running for about 15 minutes at medium current, which is sufficient for atomic scans and loading of single ions, initializing the experiment. Eventually, the micromotion amounts to about  $150 \text{ V m}^{-1}$ .

At 16:00h, this micromotion was minimized by changing the compensation voltage by  $\Delta U_{ec} = 20.3 \text{ mV}$ , which corresponds to a dc field of  $\Delta E_{dc,x} \approx 3.2 \text{ V m}^{-1}$ . Directly after the compensation a new ion is loaded with the oven running for about five minutes, to investigate the influence of a loading event. No change in micromotion in all components is observed within the resolution.

About one hour later the oven is turned on again, this time for a longer period.



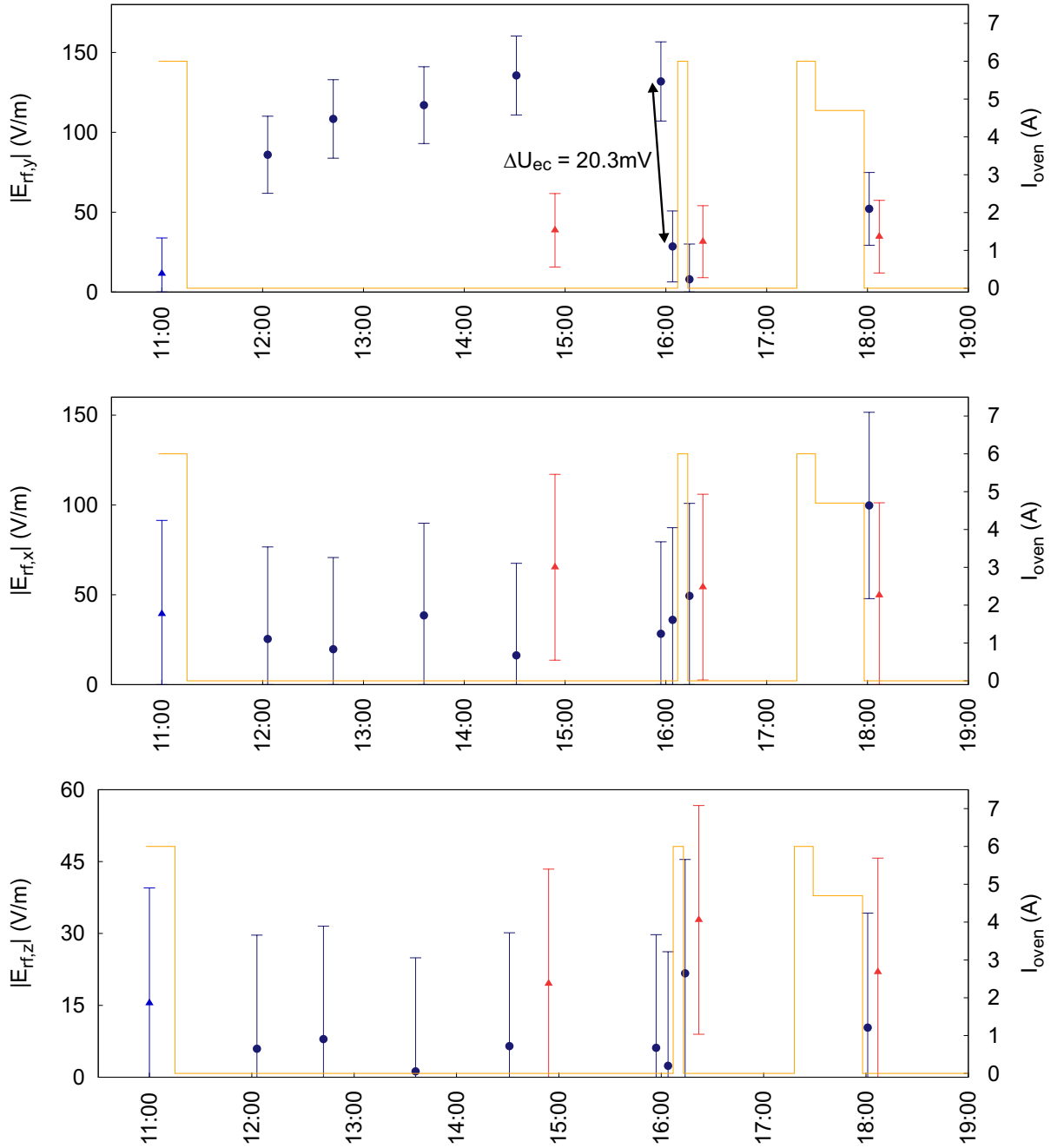


**Figure 5.16:** Longterm micromotion measurement in the loading segment (circles) and the central segment (triangles). In between, single ions are loaded to test the influence of atomic contamination of the trap electrodes on the micromotion compensation in the loading segment as well as in the central segment (red triangles). For the central segment a measurement from the preceding day is shown (blue triangles). The oven current (orange line) is indicated to mark the time for loading a new ion. **Top:** The vertical micromotion component, controlled by  $U_{\text{ec}}$ . The jump of the measured values at around 16:00 is due to minimization of the micromotion applying  $\Delta U_{\text{ec}} = 20.3 \text{ mV}$ , which corresponds to a dc electric field of about  $\Delta E_x \approx 3.2 \text{ V m}^{-1}$ . **Center:** The horizontal radial micromotion component. **Bottom:** The axial micromotion component.

After eventually loading an ion and switching off the oven a small drift of the measured micromotion is observed in both radial components, comparable to the drift observed earlier in the vertical component.

Looking at the micromotion in the central segment, however, shows no change within the measurement resolution in all components. The data points taken on the preceding day exhibit the same values as well.

From this, it can be said that loading of single ions does not influence the micromotion compensation significantly. The observed drifts are on the order of the measurement resolution and do not allow a quantitative statement.

In the central segment the influence of the oven is negligible for this measurement as one would expect, since here the electrodes do not get contaminated. The only change one might expect to see is in the axial micromotion component, because the contaminated loading segment provides axial confinement for the central segment. But stray fields in this order of magnitude do not shift the ion axially at a detectable level in this trap. In principle, the radial micromotion compensation voltages inhibit crosstalk to neighbouring segments. As shown in the next section, dc fields of this magnitude are also not detectable in neighbouring segments.

Furthermore, a heating of the trap due to constantly applying rf power does not show any visible effect on the micromotion compensation on this time scale, since this would affect the whole trap geometry and therefore the compensation in all trap segments. The drifts observed in this measurement only occur in the loading segment, see Fig. 5.16.

Another observation of the micromotion compensation was done over 41 days, measuring the micromotion in all dimensions at fixed trap parameters and compensation voltages in the central segment. The parameters are the same as in the measurement described before, the compensation voltages are  $U_{ec} \approx 0.552 \text{ V}$  and  $U_{tc} \approx -0.013 \text{ V}$ . The measured micromotion is shown in Fig. 5.17.

Within the plotted period of 41 days a maximal drift of about  $100 \text{ V m}^{-1}$  per day is observed in all components. For the x component there is drift showing up at the end of the period indicating, that the vertical compensation changes. For the y component all data points except the one from February 25th are constant within the resolution.

This demonstrates, that even over several days containing many loading events the micromotion compensation stays optimized, an important feature of the trap, for an application in clock spectroscopy.

The last analysis shows the dc compensation voltages obtained after minimizing micromotion recorded over several months. Compared are again the loading segment and the central segment, see Fig. 5.18.

For both segments the largest drift is observed in both dimensions between the measurements in the beginning of the year and the beginning of July. For the x components the optimal compensation field changes by about  $35 \text{ V m}^{-1}$  in both segments. This can be explained by the bake out of the apparatus in April, which was carried out with the trap in the vacuum chamber, see Sec. 4.4. Due to heating, expansion of the elastic trap boards leads to deformation of the trap stack, therefore changing the distance between the electrodes in x direction.

The drift of the compensation fields in the y direction is different for the two segments.

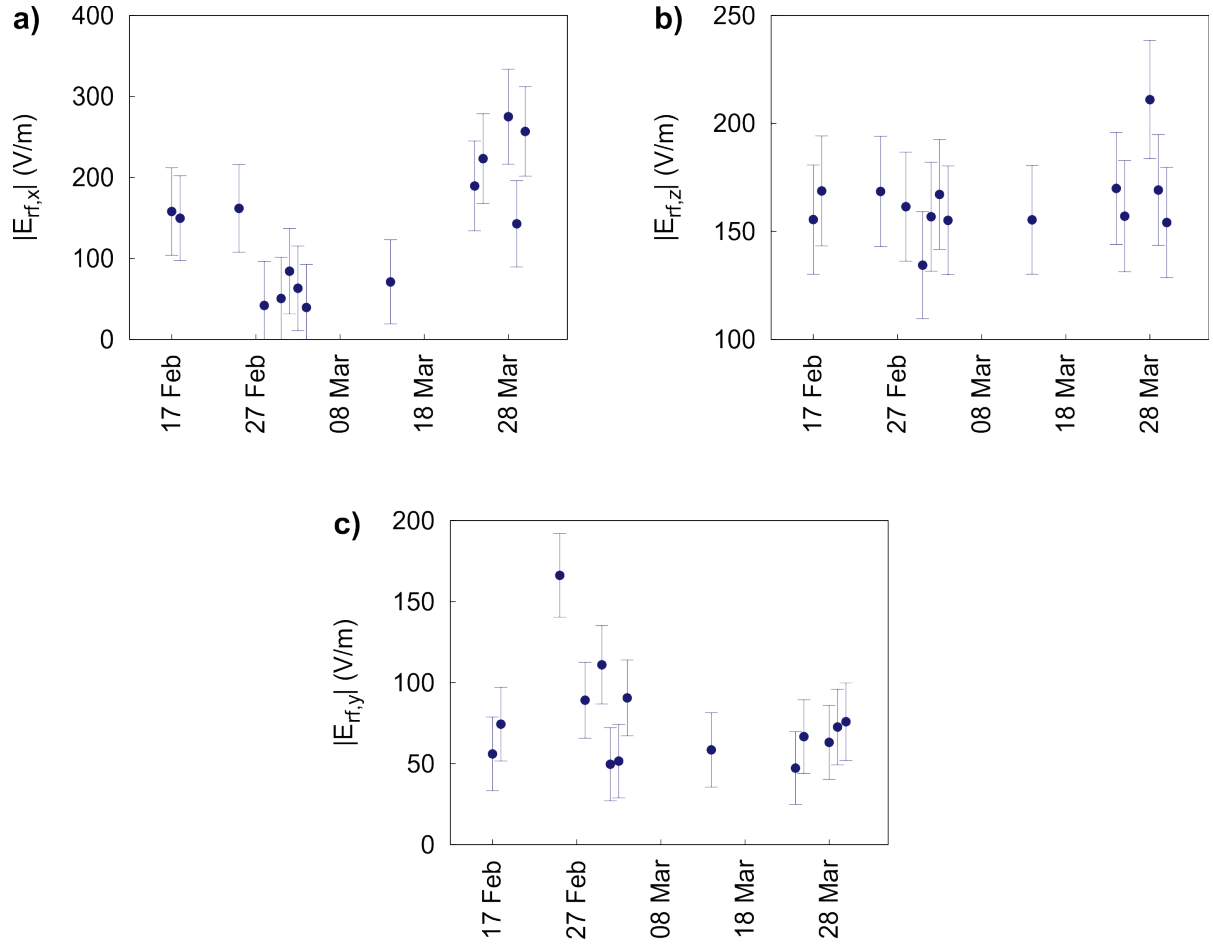


**Figure 5.17:** Measured micromotion at fixed parameters in the central segment over 41 days. The trap voltages are  $U_{rf} \approx 810$  V,  $U_t \approx 0.05$  V and  $U_{ax} \approx 4$  V. The compensation voltages are  $U_{ec} \approx 0.552$  V and  $U_{tc} \approx -0.013$  V. Shown are the a) x component, b) z component and c) y component.

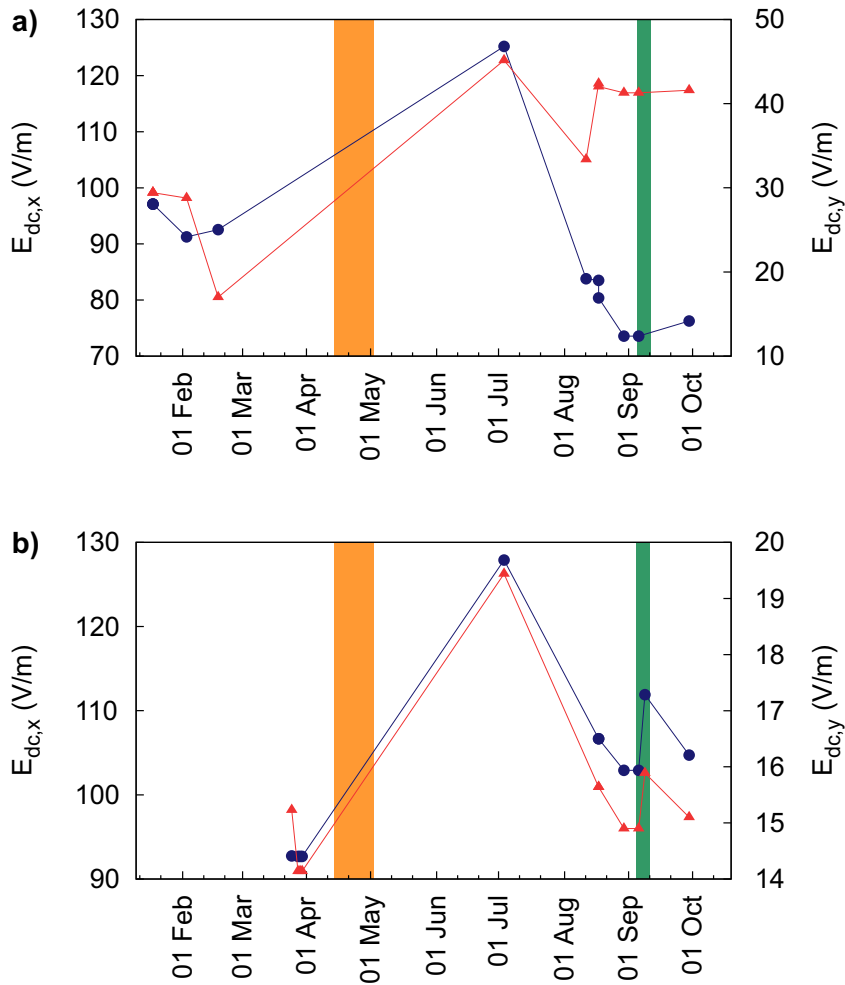


**Figure 5.18:** Compensation dc fields after minimizing micromotion recorded over several months in the **a)** loading segment and **b)** central segment. Plotted are the dc fields calculated from the applied compensation voltages. The blue circles indicate the x component, the red triangles indicate the y component. In April the whole apparatus was baked at a temperature between 65...100 °C for two weeks (orange bar). In September the trap operated over night, in total for  $\approx 34$  hours (green bar).

In the loading segment a drift of about  $25 \text{ V m}^{-1}$  similar to the x component is observed, whereas in the central segment only  $5 \text{ V m}^{-1}$  difference are measured. This differential change can be due to desorption of atomic ytterbium from the loading segment electrode during the bake out, since only the loading segment is contaminated and the thermal expansion of the trap stack is much less in y direction.

After the bake out the compensation fields drift differently for the two segments. At first, it looks like the expansion of the trap boards is reversed until the beginning of September in both segments. Only the y component in the loading segment starts again to drift in the opposite direction due to new contamination of the electrodes. After this, the values change only at a small rate, except for a sudden jump between two days observed in the central segment. This is possibly due to the fact that the trap was left running over night in order to test trapping times for a single ion. The return of the compensation voltages on September 30th almost back to the value before the two-day measurement implies a relaxation of the trap due to switching off the trap drive at night again.

### 5.3.4 Measurement crosstalk of compensation voltages

The crosstalk of compensation voltages to neighbouring segments was investigated in the laser cut trap using photon-correlation spectroscopy. For this, a single ion was loaded and trapped in the central segment and the micromotion measured as a function of the compensation voltages in the loading segment. For normalization the micromotion was measured while changing the compensation voltages of the central segment. The trap and laser parameters are the same as in the previous measurements. In Fig. 5.20 the results for changing  $U_{\text{tc},2}$  and  $U_{\text{tc},3}$  are shown. The data in each radial direction are fitted with linear functions. An example is given for the measured x component due to  $U_{\text{tc}}$ :

$$\left| E_{\text{rf},x}^{(i)} \left( U_{\text{tc}}^{(i)} \right) \right| = s_x^{(i)} U_{\text{tc}}^{(i)}, \quad (5.17)$$

$$\left| E_{\text{rf},x}^{(i)} \left( U_{\text{tc}}^{(i+1)} \right) \right| = s_x^{(i+1)} U_{\text{tc}}^{(i+1)}, \quad (5.18)$$

with the index  $i$  of the segment where the compensation voltage is applied. From the ratio of the slopes  $s_x^{(i)}$  and  $s_x^{(i+1)}$  the relative crosstalk  $c_{\text{tc},x}$  of  $U_{\text{tc}}$  to the neighbouring segment is obtained:

$$c_{\text{tc},x} = \frac{s_x^{(i+1)}}{s_x^{(i)}}. \quad (5.19)$$

This procedure is in the y direction similarly. The error is calculated using Gaussian error propagation. The results are presented in Tab. 5.3 and compared with FEM calculations. In the calculations the dc field components in the neighbouring segments are compared to each other directly, see Fig. 5.19. Thus, it is important to keep in mind, that the rf electric field components are measured orthogonal to the shifting dc field component.

**Table 5.3:** Cross-talk of compensation voltages  $U_{tc,3}$  and  $U_{ec,3}$  measured with a single ion in segment 2 and compared to FEM calculations. The measured rf field component is orthogonal to the shifting dc field component, thus the calculated dc field in x direction is compared to the measured rf field y component and vice versa.

		measured values	calculated ( $z = 0$ )	calculated ( $z = 300 \mu\text{m}$ )
$c_{tc}$	x	$0.007 \pm 0.001$	0.015	0.006
	y	$0.005 \pm 0.001$	0.019	0.007
$c_{ec}$	x	$0.073 \pm 0.005$	0.09	0.06
	y	$0.12 \pm 0.10$	0.05	0.01

The same procedure was applied for changing  $U_{ec}$ , see Fig. 5.21 and the results are given in Tab. 5.3 as well.

The comparison of the measured data to the calculated values shows a difference of up to a factor of four in the case of  $U_{tc}$ . This can be explained by looking at the calculation of the electric field along the trap axis, when applying a voltage in segment 3. An example for  $U_{tc}$  is given in Fig. 5.19, in which both radial field components are plotted along the trap axis for  $x = y = 0$  over all three inner segments.

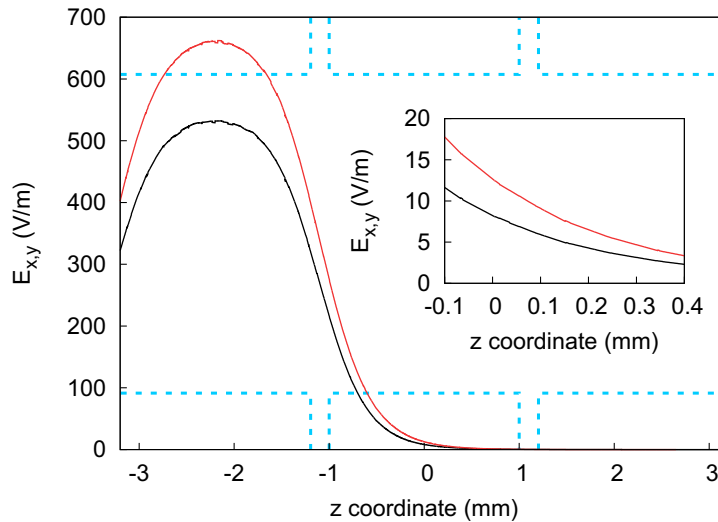


**Figure 5.19:** FEM calculation of the dc field, when applying  $U_{tc} = 1 \text{ V}$  in segment 3. The x (y) component is indicated by the black (red) line. The inset is a close up of the region around the center of segment two. The relative crosstalk is obtained from the ratio of the field amplitudes at the center of each segment:  $c_{x,y} = E_{x,y}(z = 0)/E_{x,y}(z = -2.2)$ .

The estimated values for the relative crosstalk given in Tab. 5.3 are evaluated by reading the values for the field components in the center of each segment. Since the field has a gradient, a region on the trap axis can be found a few hundred micrometers next

to the center, in which the calculated relative crosstalk matches the measured values, indicating that the ion may not be exactly in the center.

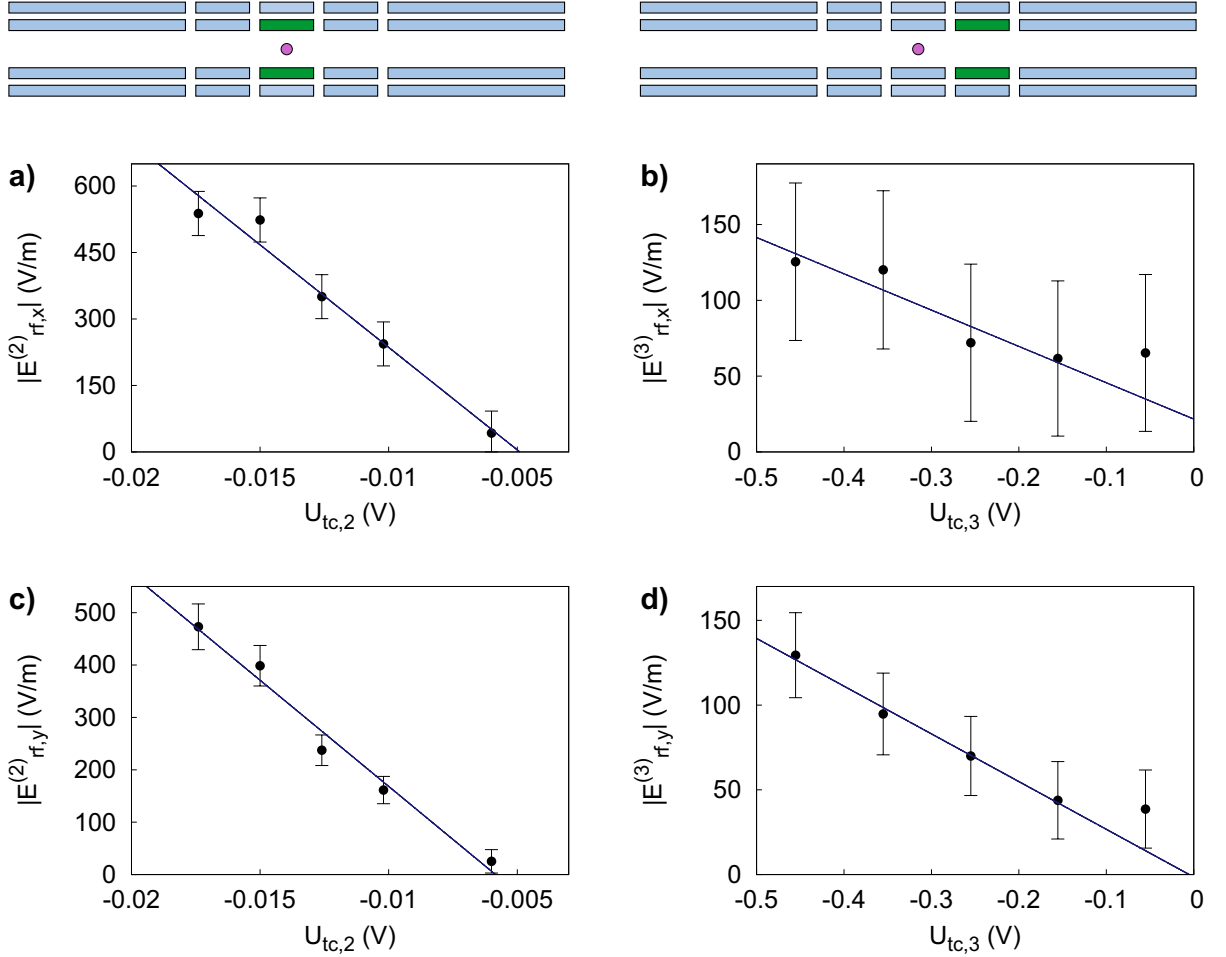


**Figure 5.20:** Measured rf field due to micromotion of a single ion trapped in the central segment (2). Plotted are the field components in x and y direction for changing  $U_{tc,2}$  (left) and  $U_{tc,3}$  (right). For the fits in the loading segment (3) the data at  $U_{tc,3} = -0.05$  V are not included, since around this value the micromotion is minimized and scaling cannot be observed. The fitted slopes in x direction are: a)  $s_{tc,2}^{(x)} = (-46.3 \pm 4.6) \times 10^3 \text{ V m}^{-1} U_{tc,2}^{-1}$  and b)  $s_{tc,3}^{(x)} = (-240 \pm 57) \text{ V m}^{-1} U_{tc,3}^{-1}$ , as well as in y direction: c)  $s_{tc,2}^{(y)} = (-40.5 \pm 3.4) \times 10^3 \text{ V m}^{-1} U_{tc,2}^{-1}$  and d)  $s_{tc,3}^{(y)} = (-282 \pm 15) \text{ V m}^{-1} U_{tc,3}^{-1}$ .

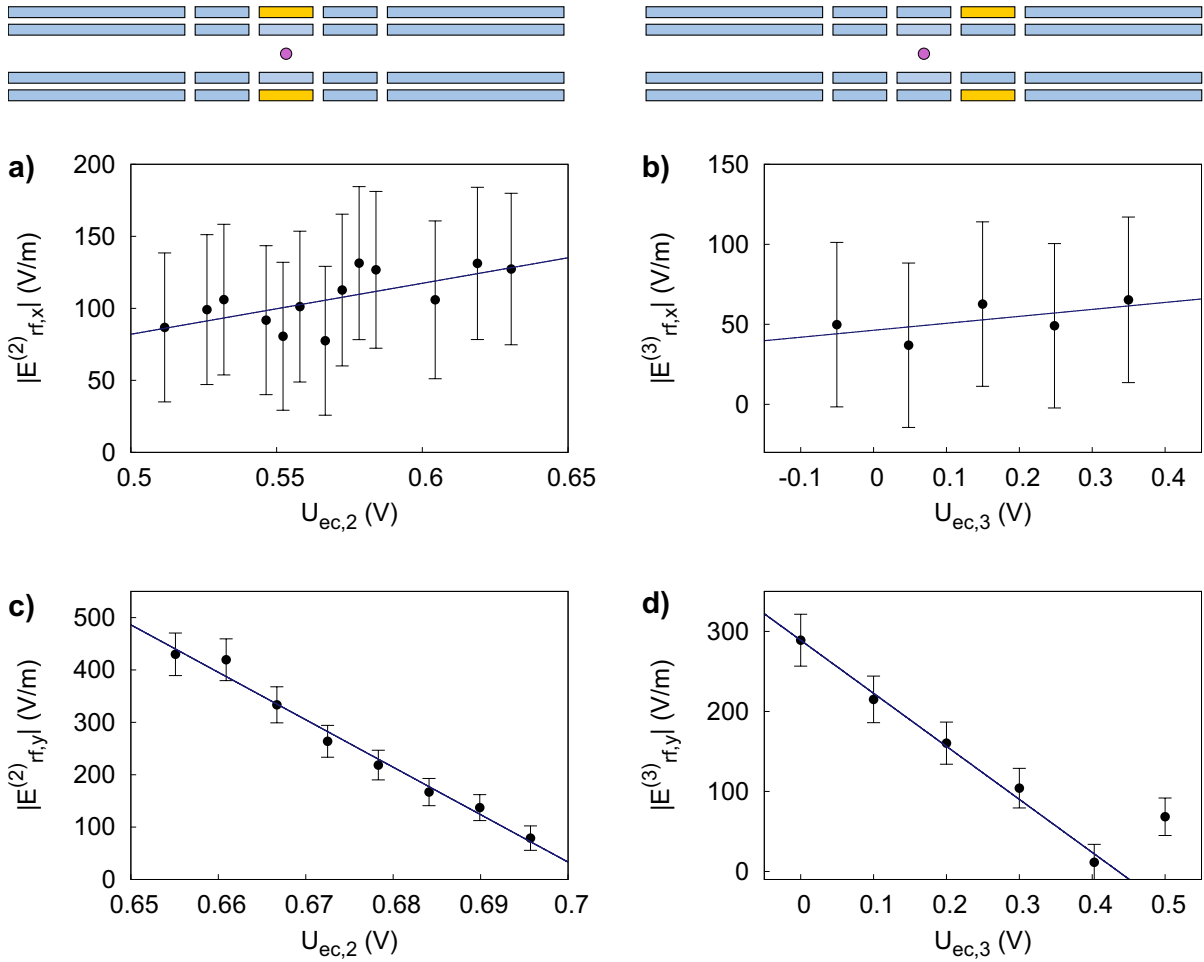


**Figure 5.21:** Measured micromotion of a single ion trapped in the central segment (2). Plotted are the micromotion components in x and y direction for changing  $U_{ec,2}$  (left) and  $U_{ec,3}$  (right). In d) the data at  $U_{ec,3} = 0.5$  V is not included in the fitting range. The fitted slopes in x direction are: a)  $s_{ec,2} = (354 \pm 120) \text{ V m}^{-1} U_{ec,2}^{-1}$  and b)  $s_{ec,3} = (43 \pm 34) \text{ V m}^{-1} U_{ec,3}^{-1}$ , as well as in y direction: c)  $s_{ec,2} = (-9.0 \pm 0.5) \times 10^3 \text{ V m}^{-1} U_{ec,2}^{-1}$  and d)  $s_{ec,3} = (-663 \pm 35) \text{ V m}^{-1} U_{ec,3}^{-1}$ .



## Chapter 6

# Structural phase transitions and topological defects in Coulomb crystals

With the prototype trap introduced in the preceding Chapters it was possible to carry out measurements on the dynamics of  $^{172}\text{Yb}^+$  Coulomb crystals during symmetry breaking phase transitions. This section details on the work presented in Pyka *et al.* [57].

First, a brief review and historical background of symmetry breaking phase transitions is given to introduce the physical background of the presented measurements. The Kibble-Zurek mechanism (KZM) is introduced as a possible scenario to predict the scaling of the rate of defect formation with the rate at which the transition is driven. Moreover, it tries to predict this scaling in a universal manner, such that it is applicable to a wide range of physical systems.

The second section focuses on the structural phase transition from a linear Coulomb crystal to a two dimensional “zigzag” configuration and gives the relevant equations derived in accordance with the theoretical model of phase transitions elaborated by Landau and Ginzburg. The KZM extends this model and includes non-equilibrium dynamics at the critical point of the transition to explain the formation of topological defects (in the following referred to as kinks) when the system changes from the symmetric (linear) to the symmetry-broken (zigzag) phase.

Numerical simulations are described in Sec. 3, that are carried out in order to find a range of experimentally feasible parameters as well as provide simulated data that may be compared to measurements. Furthermore, the dynamics of the kinks are investigated.

In Sec. 4, the experimental setup and measurement scheme are described in detail, focusing on the evaluation of the quench parameter, as well as the methods for analysis of the obtained data.

In the last section the analysis of the experimental data is presented. The measured data are compared to the simulated data and the observed scaling is analyzed.

## 6.1 Introduction to the field

Phase transitions are ubiquitous in nature, from the melting of ice to condensed matter, super fluidity, formation of magnetic domains or phenomena in cosmology [58–62]. Intriguing is the fact that the behaviour of such different systems in phase transitions exhibits universal characteristics that can be described by the same mathematical model. So far, this has led to a comprehensive effort of studies in a wide range of systems [62–67].

A successful phenomenological approach to describe phase transitions is based on theoretical work of Landau and Ginzburg [68, 69]. Here, the important properties that determine the behaviour of a system near a phase transition are the relaxation time, as a measure of the rate at which the system returns to its thermodynamic equilibrium, and the correlation length, as a measure for the scale at which fluctuations affect the system. Phase transitions are characterized by the divergence of the relaxation time as well as the correlation length in the vicinity of the critical point at which the transition occurs.

Because this diverging correlation length becomes much larger than the interatomic spacing of a system, its microscopic properties become less important and the behaviour of the system can be described by universal scaling laws that are represented the critical exponents [68]. Furthermore, the system exhibits anomalous static and dynamic physical properties near the critical point, for example the formation of local defects in the globally ordered structure of the symmetry broken phase of the system after the quench (change in a control parameter of the system that induces the phase transition).

Kibble proposed a scenario like this in the beginning of the universe during the cooling down and expansion after the Big Bang [58, 59] to understand its current structure. The idea was that fluctuations in the system freeze out when the temperature went under a critical value, including temporary defects in the structure. These defects occur because the fluctuations can only propagate within causally connected regions<sup>1</sup> (domains) before the freeze-out. After passing the critical point, the domains relax independently to the new state, stabilizing the defects. In his work he attempted to predict a scaling law of the formation of defects depending on the quench rate with which the phase transition takes place. However, since he assumed thermal equilibrium of the system, he found the creation of defects for the most part independent of the quench rate.

Zurek took over this idea and additionally took into account the non-equilibrium nature of phase transitions. His argument was that the actual value of the correlation length at the freeze-out time is determined by the rate at which the system can follow the quench, which is maximal at the freeze-out time. Like this the correlation length as a scale for the formation of defects is related to the quench rate. Based on this concept the Kibble-Zurek mechanism has been investigated theoretically in a variety of systems [60, 70–72].

Several experimental approaches were successful in demonstrating defect formation in homogeneous systems [62, 73, 74], but weak dependence on the transition rate and limited control over external parameters so far prevented conclusive results on KZM

---

<sup>1</sup>Here, Kibble introduces the size of domains as the distance on which fluctuations travel at the speed of light within the critical freeze-out time.

related scaling of defect formation. Another difficulty in comparing experiment with the theory is the task of determining the critical exponents of a system in order to give a realistic prediction of the scaling coefficient. Recent predictions for KZM scaling focus on inhomogeneous systems, in which the critical point is reached at different instances for different positions, in contrast to homogeneous systems. An illustrative example of each system type is given by the linear to zigzag transition of ions confined in a ring trap (homogeneous) or a linear trap providing three dimensional harmonic confinement (inhomogeneous). The latter is illustrated in Fig. 6.1.

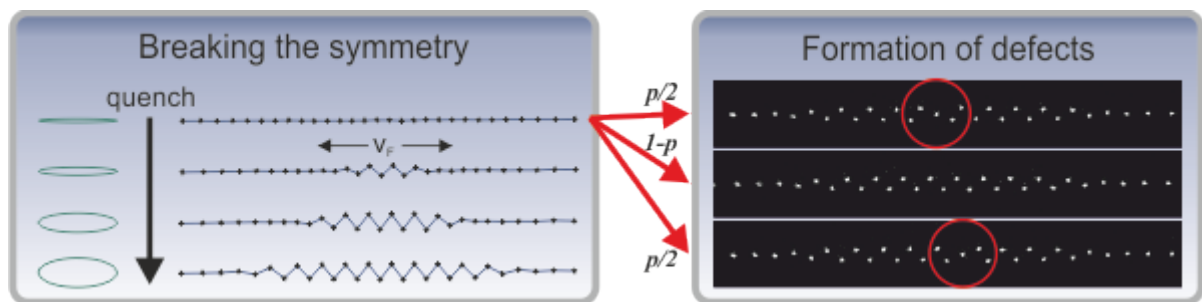


**Figure 6.1:** Illustration of a structural phase transition in a Coulomb crystal. **Left:** Release of the radial confinement at constant axial potential leads to a change from linear to “zigzag” configuration with lowest potential energy. The system undergoes a phase transition from a symmetric to a symmetry broken phase. In this finite inhomogeneous system the phase transition occurs first in the center of the chain and propagates on a front with velocity  $v_F$  to the ends of the crystal. **Right:** Depending on the front velocity the system chooses different configurations in the symmetry broken phase. Here, three outcomes are shown: a kink (anti-kink) in the top (bottom) or a regular “zigzag” without defects in the middle.

Here, due to the inhomogeneous inter-ion spacing, the phase transition first occurs in the center of the ion chain and moves out to the ends on a critical front. These dynamics enhance the role of causality and steepen the scaling of the rate of defect formation with the transition rate as predicted recently for various systems [71, 75–77].

In the presented work the defect density is measured as a function of the quench rate for the linear to zigzag transition in  $^{172}\text{Yb}^+$  Coulomb crystals using the experimental setup introduced in the preceding chapters. The experimental data are supported with numerical simulations at the experimental parameters. The results give rise to questions about new physical regimes in which a modification of KZM scaling is possible [74] with respect to the predictions made in del Campo *et al.* [71].

## 6.2 Theoretical description

In the presence of laser cooling, such that the kinetic energy becomes smaller than the Coulomb force-induced interaction energy, ions confined in a harmonic potential arrange into a crystal-like structure (*Coulomb* or *Wigner crystal*) exhibiting collective dynamics, which dominate the behaviour of the ensemble.

The particular structure depends on the interplay between the trap potential pushing the ions together and the counteracting Coulomb potential. The Hamiltonian of the system is:

$$H(\mathbf{r}, t) = \sum_{i=1}^{N_{\text{ion}}} \left( \frac{m}{2} \dot{\mathbf{r}}_i^2 \right) + E_{\text{trap}} + E_{\text{coul}}, \quad (6.1)$$

$$\text{with } E_{\text{trap}} = \sum_{i=1}^{N_{\text{ion}}} \left[ \frac{m}{2} (\omega_{x,i}^2 x^2 + \omega_{y,i}^2 y^2 + \omega_{z,i}^2 z^2) \right], \quad (6.2)$$

$$\text{and } E_{\text{coul}} = \frac{e^2}{4\pi\epsilon_0} \sum_{i<j}^{N_{\text{ion}}} \frac{1}{|\mathbf{r}_i - \mathbf{r}_j|}. \quad (6.3)$$

In order to minimize their potential energy the ions arrange into a structure that depends only on the ratio of the secular frequencies transverse to and in the direction of the symmetry axis. For a tight radial confinement the ions line up on the trap axis forming a chain. For constant axial confinement when lowering the radial trap frequency, at a certain point the ions experience an effective saddle-point potential [78] and the chain becomes unstable. Eventually the ions rearrange into a two-dimensional zigzag structure, see Fig. 6.1. Lowering the radial confinement even further leads to more complex three dimensional configurations. In Fishman *et al.* [79] the stability of Coulomb crystals has been investigated looking at the spectrum of the normal modes of the crystal. There it is found that the mode which first becomes unstable at the critical point is the zigzag mode and the critical frequency has been derived analytically from the dispersion relation for a homogeneous system. According to Steane *et al.* [80] this critical frequency can be well approximated for mesoscopic crystals ( $N_{\text{ion}} \sim 10 \dots 1000$ ) by:

$$\frac{\omega_{\text{rad}}}{\omega_{\text{ax}}} = 0.73 N_{\text{ion}}^{0.86}. \quad (6.4)$$

A more important outcome of the work in Fishman *et al.* [79] is the demonstration of the linear to zigzag transition to be a second order phase transition, which allows the determination of the critical exponents.

In homogenous systems, for example ion crystals in a ring trap, the phase transition occurs globally at the same instant. Here, the speed of sound is  $v = a \omega_{\text{ax}}$  [71], with the constant lattice parameter  $a$  and the axial trap frequency  $\omega_{\text{ax}}$ .

However, in inhomogeneous systems, for example ion crystals confined in a linear trap as presented in this work, the critical point of the phase transition is reached locally at different times. Here, the inter-ion distance  $a(z)$  is not constant and can be well approximated using the axial charge density  $n(z) = n(0)(1 - z^2/L^2) = 1/a(z)$  [81], with  $n(0) = \frac{3}{4}N_{\text{ion}}/L$  and the half-length of the crystal  $L$  at the axial ion position  $z$ . Thus, with the maximal ion density in the center of the crystal, the critical point is first reached in the middle, propagating on a front towards the ends of the crystal. From this it can be seen that defects can only form in a region where the front velocity is larger than the speed of sound, which is a measure for the velocity of fluctuations propagating

through the crystal. This enhances the role of causality, leading to a larger scaling of the formation of defects.

Another characteristic systematic feature is motional damping of the fluctuations driving the transition, sometimes also referred to as viscosity [82]. In the case of Coulomb crystals in ion traps this damping is induced by the dissipative process of laser cooling, which can be described in terms of the friction coefficient  $\eta$ :

$$\eta = \frac{2s}{(2+s)^2} \hbar k^2, \quad \text{at } \Delta = -\frac{\Gamma}{2}, \quad (6.5)$$

with the saturation parameter  $s$  of the cooling laser, its wavenumber  $k$  and its detuning  $\Delta$  with respect to the atomic transition with linewidth  $\Gamma$ , see [83]. As in the analogous case of a harmonic oscillator, the dynamics of the system, and thus the scaling of defect formation, depend strongly on the friction parameter. In the overdamped case, the dynamics close to the critical point are dominated by relaxation motion due to the strong damping. Moreover, the density of defects  $d_o$  directly depends on  $\eta$ , as was derived for the linear to zigzag transition in Coulomb crystals in [76]:

$$d_o \propto \frac{\eta \delta_0}{\tau_Q}. \quad (6.6)$$

Here,  $\delta_0$  is the amplitude of the quench, when ramping down the transversal trapping potential, and the quench time  $2\tau_Q$  is defined as half of the ramp duration.

In the underdamped regime, the dynamics is dominated by the oscillatory motion of the ions, leading to a scaling of the density of defects  $d_u$ , that is independent from the friction coefficient  $\eta$  and more pronounced [76]:

$$d_u \propto \left( \frac{\delta_0}{\tau_Q} \right)^{4/3}. \quad (6.7)$$

This is the regime in which the presented measurements are carried out.

Both scalings shown here are derived for an ion chain confined in a harmonic potential, obeying the inhomogeneous KZM (IKZM). The derivation is under the premise that the region  $x_d$  in which defects form is much smaller than the crystal size  $2L$ :  $x_d \ll 2L$ , in order to obtain a power-law scaling [84]. The scaling of  $4/3$  (1) derived here, is significantly enhanced compared to the scaling of  $1/3$  ( $1/4$ ) in the homogenous KZM regime for the underdamped (overdamped) case [76].

Currently under theoretical and experimental investigation is the situation in which the correlation length becomes comparable to  $x_d$ , in other words, where not more than one defect is created during a quench. In this case, it is suggested that the scaling of the density of defects is doubled compared to the IKZM scenario:

$$d_1 \propto \left( \frac{\delta_0}{\tau_Q} \right)^{8/3}, \quad (6.8)$$

which has also been observed in several other systems [72, 74, 85].

Two kinds of kinks have been identified [86] that are stable after the quench and therefore within reach for experimental investigation, see Fig. 6.2. The “odd” kink is created when a single ion between two independent domains is not able to follow the configuration of either one during the quench and therefore remains on the symmetry axis of the zigzag stabilized by the mutual Coulomb repulsion. This configuration is stable for shallow zigzag configurations. However, when lowering the radial confinement further, the ion breaks out into one of the edges of the zigzag rearranging the crystal in a new energetically favourable position. This configuration, with the discontinuity still present, is called “extended kink”. Because both kinks stem from the same creation mechanism, they obey the same statistics. Experimentally, these statistics cannot be recovered in every case due to loss mechanisms, as will be discussed later in this Chapter.

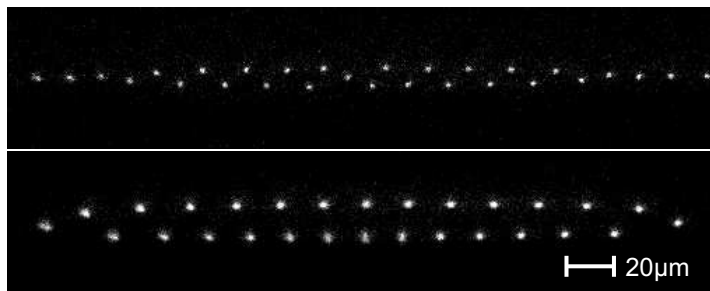


**Figure 6.2:** Pictures of experimentally obtained kinks. **Top:** “Odd” kink with the two domains separated by an ion trapped in on the symmetry axis through mutual Coulomb repulsion. This configuration is stable for shallow quenches. **Bottom:** “Extended” kink: here the ion dividing the two configurations moves out to one of the edges of the crystal. This is the energetically favourable position for quenches deeper into the zigzag regime.

## 6.3 Simulating dynamics of trapped Coulomb crystals

### 6.3.1 Method and kink detection

Numerical simulations have been carried out to investigate the dynamics of defect formation during quenches of the trapping potential, as well as to identify parameters that allow for experimental investigation [87]. For this, the trajectory of each ion during the simulation is calculated using a Runge-Kutta 4th order algorithm<sup>2</sup> from the equations of motion:

$$m\ddot{\mathbf{r}}_i = -\eta\dot{\mathbf{r}}_i + \nabla_i E_{\text{trap}}(t) + \nabla_i E_{\text{coul}} + \varepsilon_i(t), \quad (6.9)$$

with the stochastic force  $\varepsilon_i(t)$  implemented in the simulation by adding a random kick to the velocity at each time step in order to simulate thermal kicks according to temperature

<sup>2</sup>Courtesy: Ramil Nigmatullin

of the system. For the realization of the trap, the effective pseudo-potential  $E_{\text{trap}}$  is used with time-dependent radial trapping frequencies to create the quench. In this model micromotion and background collisions are not included. The ramp implemented is linear in the secular frequencies, see Fig. 6.3a. In the presented simulations the trajectories are calculated with a resolution of 1.3 ns. For evaluation of the data, however, it is advantageous to save computational resources by using a step size of  $1.3 \mu\text{s}$ , since the characteristic time scale set by the trap frequencies is on the order of a few tens of microseconds. Laser cooling is implemented as a uniform travelling wave in all three dimensions represented by the parameter  $\eta$  defined in Eq. 6.5, damping out the ion motion induced by the random kicks to thermal equilibrium.

The time evolution of the system is split into two intervals, one of which represents the quench  $t_1 = 2\tau_Q$  and the second,  $t_2$ , describes the relaxation of the system after the quench as governed by the dissipative force of the cooling laser, see Fig. 6.3a. To investigate the scaling of the kink density, the simulation is repeated several hundred times for each quench time and the statistics are evaluated.

The kink detector algorithm<sup>3</sup> scans the coordinates at each time step, evaluates the relative positions of neighbouring ions along the trap axis, and gives out a function that can take three possible values:  $f(\mathbf{r}_i, \mathbf{r}_{i+1}) = \{1, 0, -1\}$ , with  $i = 1 \dots N_{\text{ion}} - 1$ . In a regular zigzag pattern each ion will always be on the opposite site of the symmetry axis from its neighbours, thus giving:  $f_{zz}(\mathbf{r}_i, \mathbf{r}_{i+1}) = \{(-1)^i, (-1)^{i+1}\}$  depending on the orientation of the pattern. However, in the case of a kink, this alternating pattern has a discontinuity, i.e. two consecutive values with the same sign for an odd kink and a zero in the case of an extended kink, see Fig. 6.3b.

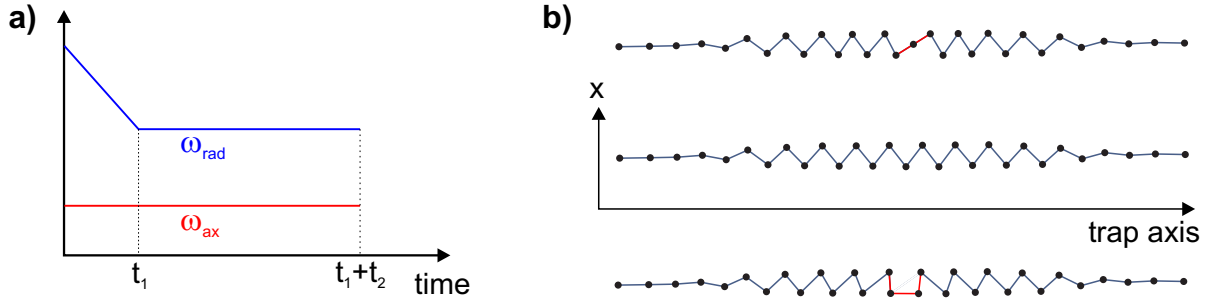


**Figure 6.3:** a) Scheme of the simulated quench. The ramp during  $t_1 = 2\tau_Q$  is linear in secular frequency. After the ramp the system relaxes for the duration  $t_2$ . To obtain statistical information this sequence is repeated between 250 and 3000 times. b) Schematic illustration of the kink detection in the simulated data. The algorithm scans the ion positions and gives discrete values  $f_{zz}(\mathbf{r}_i, \mathbf{r}_{i+1})$  for each pair of neighbouring ions, see text. In the case of a kink the regular zigzag pattern is interrupted, as indicated by the red lines. The outer regions of the crystal are ignored as an additional condition.

To analyze the dynamics of defects, the detection routine scans all recorded time steps of a simulation giving two important statistical outcomes. The first is the number

<sup>3</sup>For a detailed description, see [88].

of kinks that are created during the quench and thus accounted for by the KZM (in the following referred to as created kinks). The second is the number of kinks that is accessible in the experiment (in the following referred to as surviving kinks). The acquisition time of the camera is limited to a few tens of milliseconds, but the quench happens on the order of a few hundred microseconds or less. Therefore only kinks can be observed that survive until the acquisition time. As seen in Fig. 6.4, which shows simulated kink density as a function of time, there is a plateau in the kink density after the quench which indicates kinks that are stable long enough to be detected by the camera. Interestingly, this is not equal to the number of created kinks, which are partly lost due to several reasons that will be explained later.

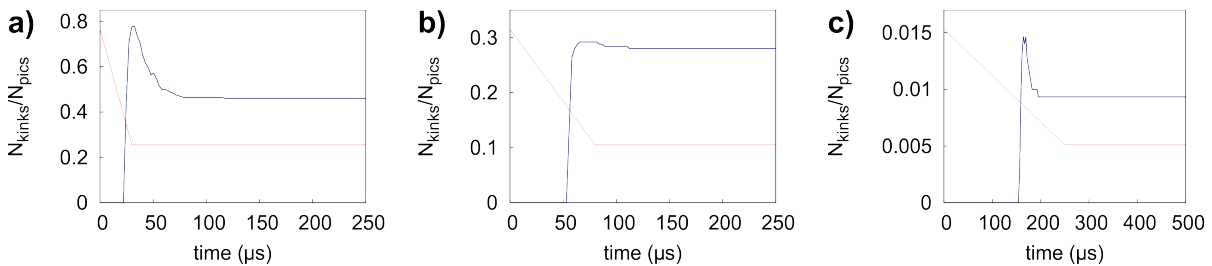


**Figure 6.4:** Time evolution of the kink density in the simulations [88]. The kink detector counts defects at each time step of the simulation (step size:  $1.3 \mu\text{s}$ ) for all sequences with the same quench time. Dividing this by the total number of quenches yields the kink density as a function of time (blue line). The quench is indicated by the red line. **a)** A simulation with  $2\tau_Q = 30 \mu\text{s}$ . Clearly visible is the peak of kinks created during the quench and the plateau of stable kinks. **b)** A simulation with  $2\tau_Q = 80 \mu\text{s}$ . The losses after the peak of created kinks is negligibly small, indicating that in this regime it should be possible to measure a scaling due to KZM. **c)** A simulation with  $2\tau_Q = 250 \mu\text{s}$ . Here, again losses are visible, this time during the quench. Reasons for the losses are given in Sec.6.3.3)

### 6.3.2 KZM regimes

A set of simulations has been carried out for a wide range of  $\tau_Q$  in order to find regimes that are accessible with the experimental setup in this work, yielding the graph shown in Fig. 6.5.

Plotted are the densities of created kinks for different quench times and the axial trap frequency  $\omega_{\text{ax}}$  suggested as an experimentally feasible parameter. On the left side, for slow quenches, the scaling is comparable to the one derived in Eq. 6.8 accounting for the DIKZM regime in which only one or no kink is created per quench. When increasing the speed of the quench, the scaling changes to a value similar to the one given for the IKZM regime. On the right the quench is fast enough that during the entire quench the front velocity is higher than the sound velocity. Here, even in an inhomogeneous system, due to the fast quench the homogeneous KZM [76] is recovered. For even faster quenches a plateau is reached, which is accounted for by the finite size of the system



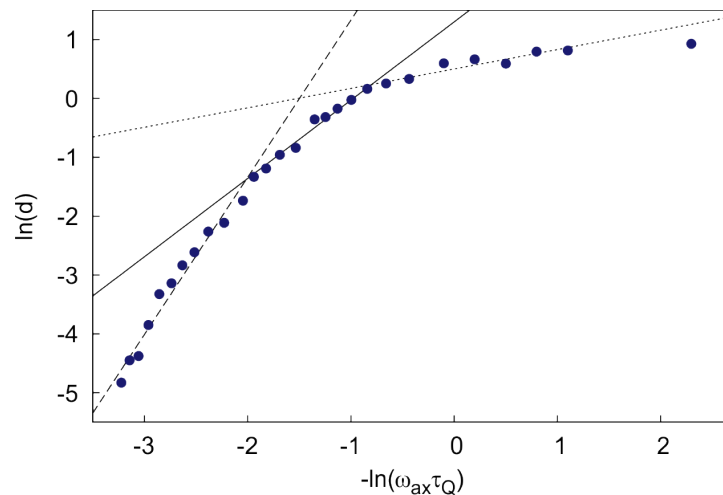


**Figure 6.5:** Density of created kinks plotted against quench time. For different ranges a change in the slope can be seen. On the left, for slow quenches, a steep slope of  $8/3$  is indicated (dashed line), suggesting kink probabilities of less than unity per realization. As the kink density increases with faster quenches, the scaling decreases to a value close to  $4/3$  (solid line), as determined by the IKZM. Increasing the quench rate further leads to a decrease of the slope to about  $1/3$  (dotted line) indicating that the velocity of the critical front exceeds the sound velocity over the whole crystal, thus recovering the homogeneous KZM regime. The friction is  $\eta = 1.5 \times 10^{-20} \text{ kg s}^{-1}$  in this simulations.

and kink-kink interactions. As already indicated in Fig 6.4 and as will be shown in the following section, not all of these regimes are accessible to the experiments.

### 6.3.3 Loss mechanisms

Not all regimes are accessible in the experiment for distinct reasons. A kink is stable because it does not have enough kinetic energy to pass a barrier, that is set by the Peierls-Nabarro potential [89], which builds up during the quench. For fast quenches a high amount of kinetic energy is brought into the system, enough for the kink to overcome the potential barrier and leave the zigzag structure. This mechanism is found to be sensitive to the laser cooling friction coefficient, see Fig. 6.6. The higher the dissipative force, the faster the system relaxes into thermal equilibrium, again providing a stable environment for the defects.

For slow quenches, when the speed of the front of the phase transition is comparable to the speed with which a defect can move within the ion crystal, losses can occur due to the inhomogeneity of the system. A kink created in the central region experiences only a low potential barrier, because the zigzag pattern is not yet completely developed. Moving faster than the front, the kink escapes the zigzag pattern to the ends of the crystal. This mechanism does not depend on the friction, see Fig. 6.6. Looking at Fig. 6.4c, the losses occur within a time of about  $40 \mu\text{s}$  or less, which corresponds to about one oscillation period at the axial trap frequency of  $\omega_{\text{ax}}/(2\pi) \sim 25 \text{ kHz}$ .

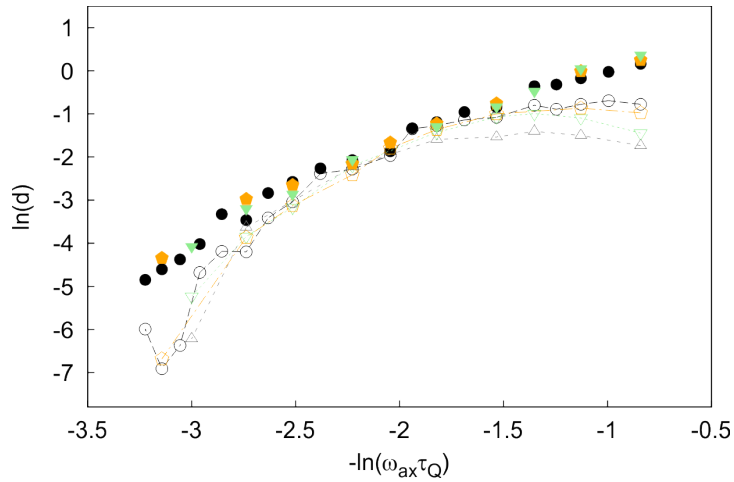


**Figure 6.6:** Kink density plotted against quench time for different friction parameters  $\eta$ :  $1.5 \times 10^{-20} \text{ kg s}^{-1}$  (circles),  $6.0 \times 10^{-21} \text{ kg s}^{-1}$  (pentagons),  $4.0 \times 10^{-21} \text{ kg s}^{-1}$  (inverted triangles) and  $3.0 \times 10^{-21} \text{ kg s}^{-1}$  (triangles). The filled symbols show the density of created kinks and the hollow symbols show the density of surviving kinks. The friction dependent losses of created kinks for fast quenches is due to excitation of the Coulomb crystal through the quench. For higher friction the motional damping is stronger and additional kinetic energy is dissipated, thus reducing the losses. The losses occurring at slow quenches appear to be independent from the friction. In this region a kink created during the quench can leave the not fully developed zigzag structure by passing the critical front.

Apart from these mechanisms, there is another property of the defects that should be considered. In case a pair of defects, naturally a kink and an anti-kink given the topological structure, is created they will annihilate when moving through the crystal. This is the case in particular for the extended kinks, which experience a Peierls-Nabarro potential that has a local minimum in the center of the crystal and a shallow modulation with periodicity of the inter-ion spacing. Thus, two kinks that are created away from the center and have sufficient thermal energy to overcome the shallow potential barriers of individual ions, they will move towards the center and annihilate. For an odd kink the Peierls-Nabarro potential has a local maximum in the crystal center and higher energy barriers between individual ions. For these kinks it is more probable to be stabilized within the zigzag. As soon as their thermal energy is high enough, they will move towards the edges of the crystal and disappear.

To determine at which point the kink density becomes larger than  $d_1$  in the simulations shown the absolute number of kinks is not counted, but rather the detection is limited to one kink per quench. Figure 6.7 shows the data of Fig. 6.5 in a closeup of the region, where the absolute density becomes larger than  $d_1$ . From this, a separation between the IKZM and the regime with an assumed doubled scaling coefficient is obtained.

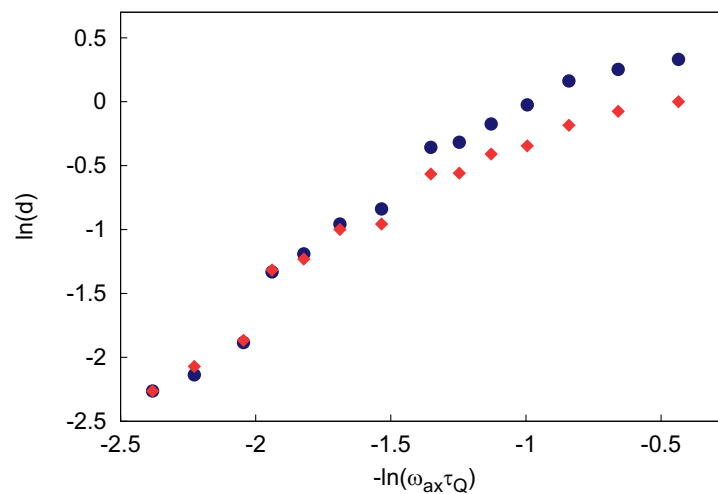


**Figure 6.7:** Kink density plotted against quench time. Here the kink detector is modified, such that it counts all kinks created (blue circles) or only detects one kink per quench regardless of the occurrence of other kinks (red rhombs). Visible is the region within which no more than one kink is detected in the ion chain, giving a distinction between the inhomogeneous KZM and the doubled IKZM regime in this system.

## 6.4 Experimental realization

### 6.4.1 Measurement sequence and parameters

The experimental realization of the described phenomenon is as follows. About 30 ions are loaded into the trap and shuttled from the loading segment (segment 3 in Fig. 3.1) into the spectroscopy segment (segment 1), which is protected from atomic contamination, by switching the dc voltages  $U_{t,i}$ . To drive the phase transition, the rf voltage is modulated with a control signal as shown in Fig. 6.8.

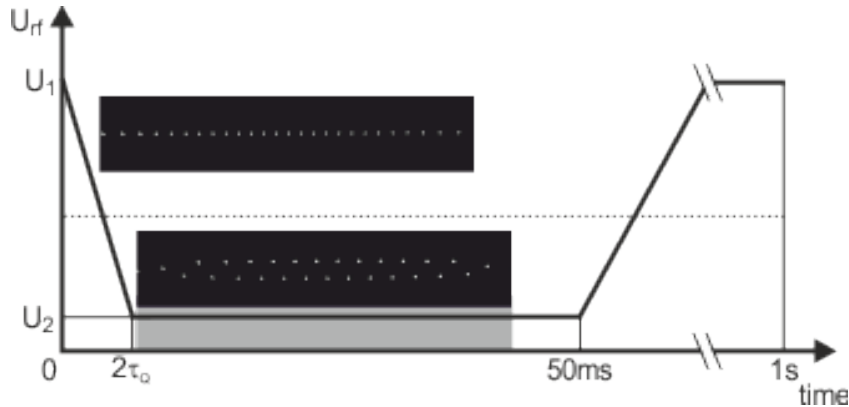


**Figure 6.8:** Schematic of the experimental sequence. To induce defect formation the radial trapping potential is quenched across the point of the linear-zigzag phase transition. For this, the rf voltage is lowered linearly, modulating the rf signal, as described in Sec. 4.5, with a control signal as shown. After the quench a picture is recorded with an exposure time of 40 ms (indicated by the grey area) and the trapping potential ramped up to the initial value. After one second the sequence is repeated.

First, a ramp linear in  $U_{rf}$  is applied with variable duration  $t_{\text{ramp}} = 2\tau_Q$ , followed by a detection time of  $t_{\text{det}} \approx 50$  ms in which a picture is taken with an exposure time of 40 ms for the presented measurements. Then the rf voltage is raised back to the initial value allowing the Coulomb crystal to relax to thermal equilibrium. This sequence is repeated with a period of  $t_{\text{cycle}} \approx 1$  s in order to obtain statistical information.

In principle this sequence can be arbitrarily repeated, but in practice there is a limitation due to collisions of the ions with the background gas. These lead to the creation of, for example,  $^{172}\text{YbOH}^+$  molecules with a rate on the order of minutes, that have an additional mass  $m_{\text{OH}}$  and experience a different ponderomotive potential, thus breaking the symmetry of the ion chain. To obtain sufficient statistics without the influence of molecules a new ion chain is loaded after molecules are created. In total several series of pictures (runs) with different ion ensembles are taken adding up to 200...4000 pictures for each quench time.

The radial trap parameters used in the measurements are given in Tab. 6.1. The axial trap frequency is  $\omega_{\text{ax}} = 2\pi \times (24.6 \pm 0.5)$  kHz measured repeatably over several months. In order to confine the ions in a two-dimensional plane an asymmetry of the radial trapping potential of about 30% is introduced by applying  $U_t \approx 0.5$  V. For cooling and detection

the beam H2 was used expanded in the horizontal dimension by a factor of about 10 with respect to the vertical dimension with a cylindrical lens of  $f = -50$  mm. With these beam parameters  $w_{\text{vert}} \approx 80 \mu\text{m}$  and  $w_{\text{hor}} \approx 8$  mm, and a power of  $P_{\text{H2}} \approx (630 \pm 30) \mu\text{W}$  at a detuning  $\Delta \approx -\Gamma/2$  the saturation parameter amounts to about  $s \approx 1$ . Assuming a single traveling wave this yields a friction coefficient of about  $\eta \approx 7 \times 10^{21} \text{ kg s}^{-1}$ .

radial axes	$\omega_{\text{lin}}/(2\pi)$ (kHz)	$\omega_{\text{trans.}}/(2\pi)$ (kHz)	$\omega_{\text{odd}}/(2\pi)$ (kHz)	$\omega_{\text{ext}}/(2\pi)$ (kHz)
1	500	275	204	140
2	517	315	255	200

**Table 6.1:** Radial trap frequencies measured before the quench  $\omega_{\text{lin}}$ , near the point of the phase transition  $\omega_{\text{trans.}}$  (when the first ions start to break out of the linear configuration) and after the quench. Depending on the depth of the quench the two defects can be produced reliably. For shallow zigzag structures at  $\omega_{\text{odd}}$  the odd kink is stable. Decreasing the radial confinement further to  $\omega_{\text{ext}}$ , the extended kink becomes the favourable configuration.

With a magnification of the camera of  $V \approx 28$  an area with length of about  $295 \mu\text{m}$  is imaged, allowing images of ion crystals with about 29 ions.

### 6.4.2 Controlled quench of the order parameter

Several tests were made to determine the correct experimental slope of the rf voltage ramp. For each ramp time the monitor voltage  $U_{\text{mon}}$  of the helical resonator is recorded and a linear function with slope  $s_{\text{real}}$  is fitted around the point of the phase transition, see Fig. 6.9.

This slope is compared to an ideal linear function with slope  $s_{\text{ideal}}$  when going from the initial to the final rf voltage within the ramp time. Due to the characteristics of the rf mixer that is used for modulation of the rf voltage, the fitted slope deviates from the ideal slope by a few percent. In order to compare the simulations with the experimental data, the “real” ramp time is deduced by  $t_{\text{real}} = s_{\text{ideal}}/s_{\text{real}} \cdot t_{\text{ideal}}$  with an error from the fit of  $\sigma_{s_{\text{real}}} = 5\%$ .

Another characteristic of the ramp, also evident in Fig. 6.9, is the smoothed edges at the beginning and the end of the slope. This is the response of the helical resonator, which acts as a bandpass filter to the linear ramp. The time constant  $\tau_{\text{hel}} \approx 7 \mu\text{s}$  of the resonator<sup>4</sup> practically limits the shortest ramp that can be applied to the rf voltage in this setup in order to obtain a linear function near the phase transition. For longer ramp times (including all of the ramp times used in these results) this behaviour becomes negligible.

In addition, the secular frequencies are measured as a function of the rf voltage in order to verify the linearity of the ramp in units of the radial trap frequency. The

<sup>4</sup>The time constant is obtained by fitting an exponential function to the response signal of a step function:  $U_{\text{mon}}(t) = U_{\text{mon}}(0) e^{-t/\tau_{\text{hel}}}$ .

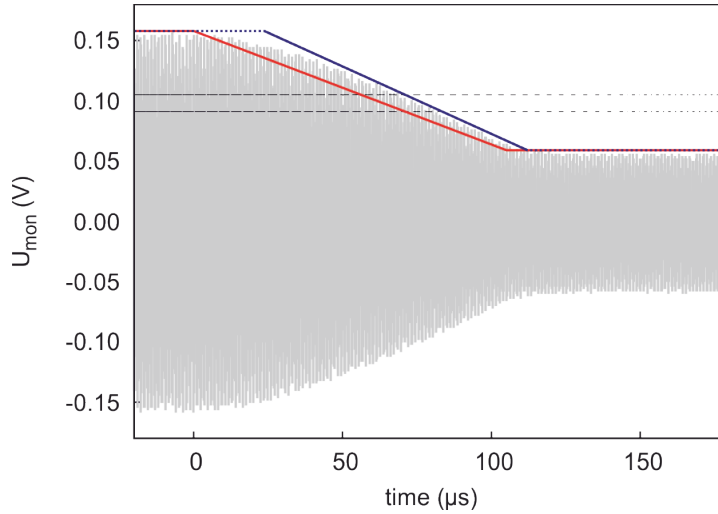


**Figure 6.9:** Monitor signal of the helical resonator (grey line) recorded during a quench with a set value of  $2\tau_Q = 105 \mu\text{s}$  (red line). The characteristics of the rf mixer lead to a change in the ramp of the rf signal from the intended ramp, which is fitted (blue line) in order to obtain the effective linearized ramp time at the critical point (area between dashed lines).

data are fitted with the analytical expression for the trap frequencies (see Eq. 5.1) and compared to an approximated linear function, which connects directly the initial and final values. The slope of this linear approximation deviates by less than two percent from the analytical expression around the region of the phase transition.

### 6.4.3 Kink detection and data analysis

For comparison pictures are recorded with and without molecules in the crystal, but for the KZM statistics only the pictures without the molecules are selected. The recorded pictures are inspected manually and the following information is extracted:

- kink/no kink
- molecule/no molecule
- kink position: left/center/right

The definition of the position of a kink in the zigzag is illustrated in Fig. 6.11. It shows that the ratio of ion pairs (as identified by the lines) left and right from the kink center should be  $4 : 6 \leq N_{\text{left}}/N_{\text{right}} \leq 6 : 4$  for a kink to be considered in the center.

After collecting the information from the pictures, statistical analysis of the data is carried out. For each run<sup>5</sup>  $i$  the kink density  $d_i$  is determined:

$$d_i = \frac{N_{\text{k},i}}{N_{\text{p},i}}, \quad (6.10)$$

<sup>5</sup>Remember: series of pictures shot with one ion ensemble without reloading.

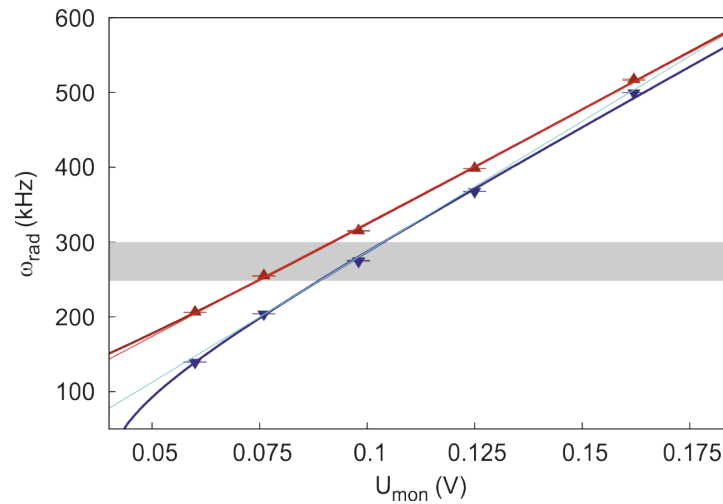


**Figure 6.10:** Radial secular frequencies measured for different rf voltages: at the initial and final points of the rf ramp and around the point of the phase transition. The uncertainty of this point (grey bar) is due to the fluctuating ion number for individual runs  $N_{\text{ion}} = 29 \pm 2$ . The dark coloured lines show a fit to the data with Eq. 5.1. These are compared with linear functions (light coloured lines), that are obtained by connecting the initial with the final values and a deviation in the slope of less than two percent is found at the region of the phase transition.

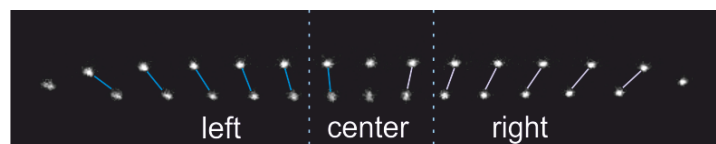


**Figure 6.11:** Definition of the position of a kink in the ion crystal.

with the number of detected kinks per run  $N_{k,i}$  and the number of pictures taken per run  $N_{p,i}$ .

For each quench time  $\tau_Q$  several runs  $n_{\text{run}}$  are recorded in order to obtain a higher statistical weight of the data, in particular for slow quenches where the kink probabilities are lower. The individual runs are combined by calculating a mean kink density  $d_m$  with the number of pictures in each run used as a weighting factor:

$$d_m = \frac{1}{\mathcal{N}} \sum_{i=1}^{n_{\text{run}}} (N_{p,i} d_i) \quad \text{with} \quad \mathcal{N} = \sum_{i=1}^{n_{\text{run}}} N_{p,i}. \quad (6.11)$$

Two contributions to the error of this mean kink density are considered:

$$\sigma_{d_m} = \sqrt{\sigma_{\text{sys}}^2 + \sigma_{\text{stat}}^2} \quad (6.12)$$

The first and more significant contribution is the scatter  $\sigma_{\text{sys}}$  of the densities  $d_{\text{run},i}$  for the individual runs  $i$ . This scatter mainly accounts for the uncertainty of the experimental conditions from one run the next, like fluctuations of the axial trap frequency, the ion number or in the cooling laser power. Because it is difficult to quantify the dependency of the kink density on systematic parameters in this regime, the uncertainty is given as the standard error of the weighted mean  $d_m$ :

$$\sigma_{\text{sys}} = \frac{\sigma_s}{\sqrt{n_{\text{run}}}}, \quad (6.13)$$

with the sample standard deviation  $\sigma_s$ , which is calculated as:

$$\sigma_s = \sqrt{\frac{\mathcal{N}}{\mathcal{N}^2 - \mathcal{P}} \sum_{i=1}^{n_{\text{run}}} [N_{p,i} (d_{\text{run},i} - d_m)^2]} \quad \text{with} \quad \mathcal{P} = \sum_{i=1}^{n_{\text{run}}} N_{p,i}^2. \quad (6.14)$$

The normalization is adjusted for small sample sizes and the number of pictures is used as a weighting factor for the individual runs.

The second contribution accounts for the statistical uncertainty assuming a binomial distribution of the data:

$$\sigma_{\text{stat}} = \sqrt{\frac{d_m(1 - d_m)}{\mathcal{N}}}. \quad (6.15)$$

This contribution is usually much smaller than the scatter  $\sigma_{\text{sys}}$  and only becomes significant when the number of runs is very small (about 2...4) and the scatter is heavily underestimated.

## 6.5 Results

### 6.5.1 KZM scaling

For the KZM scaling a total of about 26000 pictures were taken over different quench times. The result is compared to simulations with varying friction coefficients, see Fig. 6.12.



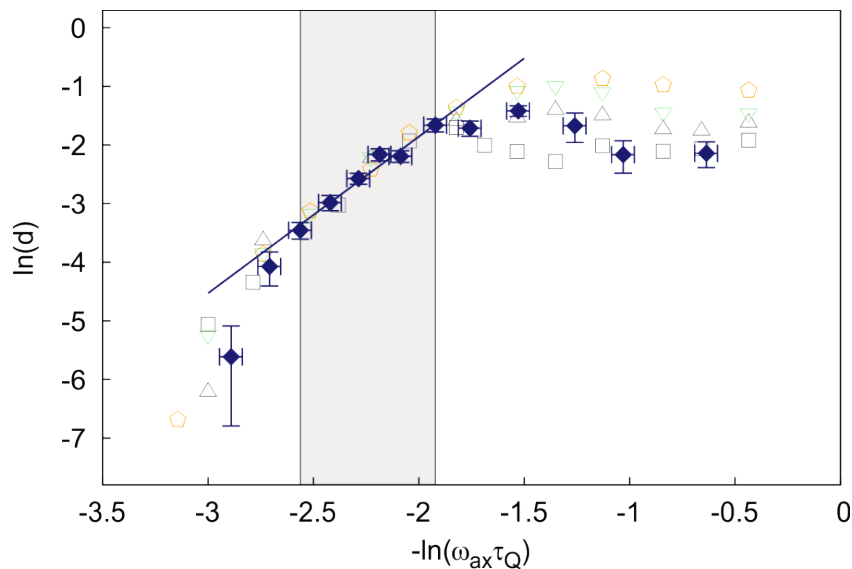


**Figure 6.12:** Kink density measured against quench time and compared to simulations with different friction parameters:  $6.0 \times 10^{-21} \text{ kg s}^{-1}$  (pentagons),  $4.0 \times 10^{-21} \text{ kg s}^{-1}$  (inverted triangles),  $3.0 \times 10^{-21} \text{ kg s}^{-1}$  (triangles) and  $2.5 \times 10^{-21} \text{ kg s}^{-1}$  (squares). An exponential fit weighted with the errors of the data in the region  $-2.6 \leq -\ln(\omega_{\text{ax}}\tau_{\text{Q}}) \leq -1.9$  yields an exponent of  $2.67 \pm 0.25$ .

First, a good agreement of the measurement with the simulated data of created kinks is visible at  $\eta \approx (2.5\dots 3) \times 10^{-21} \text{ kg s}^{-1}$  over the full parameter range. Second, the independence of the simulated data of created kinks from the friction parameter provides evidence that the system is in the underdamped regime, see Fig. 6.6. Fitting a power-law function  $d_{\text{det}} = a (\omega_{\text{ax}}\tau_{\text{Q}})^{-b}$  to the experimental data yields a scaling of the density of detected defects of  $b_{\text{exp}} = 2.67 \pm 0.25$  in that region. In the fit, the data points are weighted by their errors. A least squares test is done to test the quality of the fit, yielding a reduced residual sum of squares of  $\chi_{\text{red}}^2 = 1.2$ .

Furthermore, the simulated data shown in Fig. 6.6 are analyzed in terms of scaling of the defect density. Here, a fit to the density of created kinks in the region  $-3.2 < -\ln(\omega_{\text{ax}}\tau_{\text{Q}}) < -2$  yields a scaling of  $b_{\text{sim}} = 2.63 \pm 0.13$ .

Both results are in contradiction to the predicted scaling in the IKZM regime [71] by about a factor of two. This motivates the theoretical investigation of a doubling of the IKZM scaling in the regime where the correlation length is on the order of the size of the system and only a maximum of one defect is created per quench.

The simulated data in Fig. 6.7 demonstrated that the presented measurements were carried out in this regime.

In conclusion, this experiment demonstrated the creation of defects in structural phase transitions in harmonically confined Coulomb crystals. It provides experimental data that can be used to test theories of non-equilibrium dynamics during symmetry breaking phase transitions in inhomogeneous systems with well known parameters and boundary conditions. Thus, it paves the way for tests of KZM in a regime that is

experimentally well controlled and readily accessible.

### 6.5.2 Kink lifetime

To support the experimental data, the lifetime of the kinks in the trap has been estimated. For this additional measurement, a crystal with from a Coulomb crystal with  $N_{\text{ion}} = 31$  is trapped and after each quench with  $\tau_Q = 50 \mu\text{s}$  a series of 20 pictures is taken each having an exposure time of 40 ms. In each series the number of pictures in which a kink is detected is evaluated, only taking those series into account where the kink appears from the first picture. Presumably, these kinks are created during the quench (“spontaneous” kink creation is described later in this section). In Fig. 6.13 the number of surviving kinks is plotted over time.

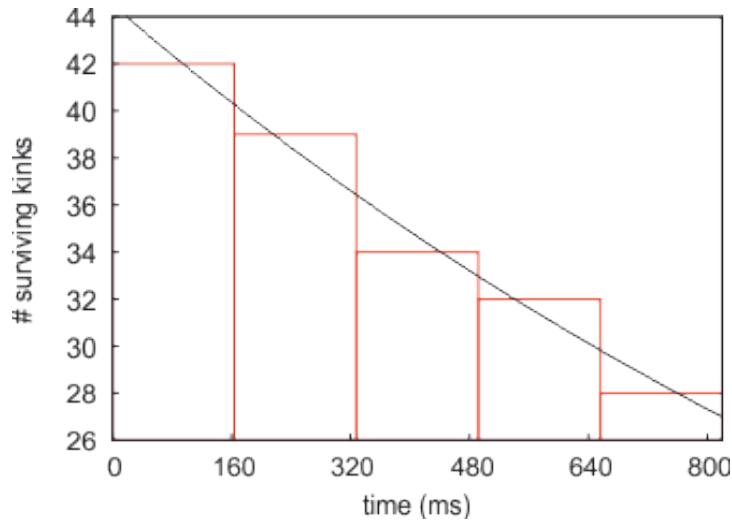


**Figure 6.13:** Measured lifetime of kinks in the trap. Plotted is the number of surviving kinks per time interval. The fit is the exponential function  $N(t) = N_0 e^{-t/\tau_l}$  yielding a time constant of  $\tau_l = (1.6 \pm 0.1)$  s. The losses of defects are due to collisions with the background gas.

Application of an exponential fit  $N(t) = N_0 e^{-t/\tau_l}$  yields  $N_0 = 44 \pm 1$  and a time constant of  $\tau_l = (1.6 \pm 0.1)$  s. This yields a rate of lost kinks of about 2% in 40 ms. This value is well within the relative error of about 10% of the measured kink densities and is thus negligible in the presented measurements.

The main reason for losses of kinks from the trap is collisions with background gas. To estimate a collision rate, a number of picture series has been recorded holding the radial potential constant in the zigzag configuration. In this way, a rate of 1 spontaneous kink in 67 s observation time is observed. Transformed into kink density this yields a value of  $d_{\text{sp}} \approx 0.0007$  ( $\ln(d_{\text{sp}}) \approx -7.4$ ), which can be neglected in the data shown in Fig. 6.12.

# Chapter 7

## Summary and outlook

In this work, the design of a segmented linear Paul trap was introduced and optimized for the operation in a multi-ion optical clock. Here, mixed-species Coulomb crystals are used with  $^{115}\text{In}^+$  as clock ions sympathetically cooled by  $^{172}\text{Yb}^+$  ions. The latter is furthermore used as a test system for the characterization of the trap and the experimental apparatus.

From FEM calculations, an optimized geometry could be derived together with an estimate for the required machining and alignment tolerances. Further estimations were done to give an upper boundary of tolerable rf phase shifts between separate electrodes that otherwise lead to non-vanishing rf electric fields and hence excess micromotion. From material considerations for the trap wafers, AlN emerged with the most desirable electric and thermal properties, as well as the need for elaborate machining processes. For the use in a first prototype Rogers 4350B<sup>TM</sup> turned out to be readily available with suitable properties. Two prototype traps could be assembled and put into operation.

The experimental apparatus to test the prototype trap was introduced. Here, the all-diode laser based optical setup for  $^{172}\text{Yb}^+$  as the atomic test system may be emphasized. The vacuum system was optimized to easily change the traps, versatile optical access for the used lasers and for characterizing trap structures in all dimensions in terms of rf fields. The detection scheme was set up for single-photon detection, as well as for spatial resolution of Coulomb crystals. The introduced high-Q helical resonator is designed for low-power rf feed of the trap and the presented dc control unit for low-noise and high-precision control of the ions in terms of micromotion compensation.

RF photon-correlation spectroscopy was implemented as the tool to measure excess micromotion in the traps and characterize them in terms of residual axial rf fields. With the presented setup a sensitivity to micromotion-induced systematic frequency shifts of  $|(\Delta\nu/\nu)_{\text{mm}}| \leq 10^{-19}$  could be demonstrated, suitable for the trap characterization with envisaged residual frequency shifts of less than  $10^{-18}$  over a large trapping region.

Both prototype traps were successfully set into operation and characterized in terms of excess micromotion. The measured axial fields were found to be in accordance with the FEM calculations considering machining tolerances of the trap parts. Here, a clear distinction can be made between the two traps in terms of the used fabrication techniques. The trap with the laser machined parts exhibit a smaller deviation from the calculated values, which assume zero tolerance. In the case of the milled trap, the derivation to

the calculations is about a factor of two larger compared to the laser cut trap, which is accounted for by the lower precision in machining.

As for the measurements on the linear to zigzag phase transition in  $^{172}\text{Yb}^+$  Coulomb crystals, a measurement scheme was demonstrated to investigate scaling laws of the rate of defects formed during the phase transition depending on the rate at which the transition occurs. The obtained results show good agreement to numerical simulations, which were also used to study kink dynamics directly after the phase transition, a regime that is not accessible with the experiment. The results may give rise to new possible regimes for the KZM in inhomogeneous systems with finite size. They are supported by the results of other experiments in similar, as well as different physical systems.

For the measurements regarding KZM scaling in the linear to zigzag phase transition, several scenarios are at hand for the near future.

First, to further support the existing data, measurements could be attempted in the inhomogeneous KZM regime, where the kink density is not limited by a maximum of one defect per quench, and to directly observe a scaling that is predicted within the KZM. For this to be realized, several aspects need to be considered: reduction of defect losses for fast quenches by increasing the friction<sup>1</sup>, measuring statistics of odd kinks instead of extended kinks, which easily annihilate due to the shape of the Peierls-Nabarro potential, see Sec. 6.3.3, and increasing the system size in the zigzag region (increase  $N_{\text{ion}}$ ) in order to reduce interaction between odd kinks.

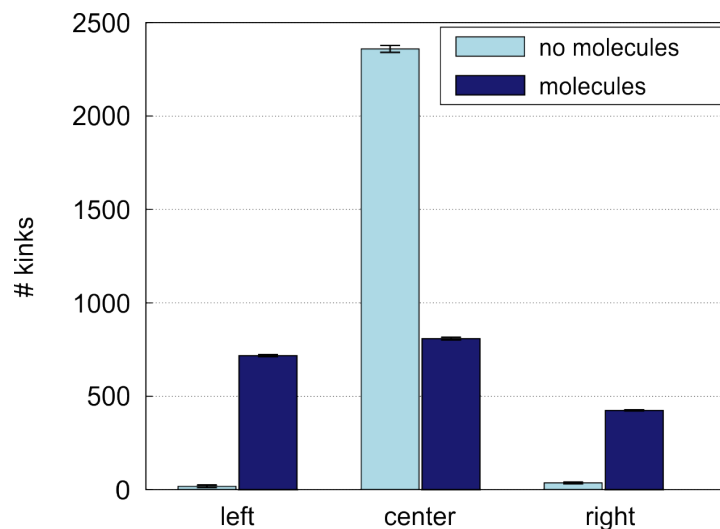


**Figure 7.1:** Spatial distribution of kinks detected along the crystal. Compared are kinks where no molecules are present (light blue) with kinks in the presence of molecules (dark blue). The error bars are calculated assuming a binomial distribution of the number of kinks. The asymmetry in the number of kinks counted on the left and right end could be explained by light-forces that act on the cooled  $^{172}\text{Yb}^+$  ions but not on the molecules, thus pushing the ions to the right, which displaces the molecules to the left.

<sup>1</sup>This is to a certain extent possible by increasing the cooling laser intensity in this experiment. In another setup the use of lighter ion species is possible.

Second, the inevitable occurrence of molecular ions due to background gas collisions leads to interesting studies of kink dynamics. For example, a molecule could be thought of as a seed for kinks, as a statistical analysis of pictures with Coulomb crystals containing molecules indicates. Here, the kink density increases for slow quenches compared to the kink densities measured without molecules, as shown in Fig. 6.12.

Furthermore, the fact that the heavier molecules experience a lower rf confinement may lead to a modification of the Peierls-Nabarro potential, such that a local minimum occurs at the position of the molecule, thus stabilizing the kink. This behaviour is indicated by the analysis shown in Fig. 7.1. Here, the spatial distribution of the number of detected kinks is plotted, according to the definition of location given in Fig. 6.11. The same data as for the statistical analysis in Ch. 6 are plotted as kinks without molecules (light blue boxes). Data not included in the KZM analysis due to the appearance of molecules are plotted as such (dark blue boxes). As the Peierls-Nabarro potential for extended kinks shows a local minimum in the center of the ion crystal the kinks are almost exclusively detected in the center of the trap, indicating the migration of kinks created at the sides of the crystal<sup>2</sup>. In contrast to that, the kinks that are created while a molecule is present in the crystal, are nearly equally distributed over the length of the zigzag. First simulations indicate that a molecule rather stops a kink than to act as a seed. Nevertheless, it can alter the kink density depending on the mass of the molecule and moreover its position in the crystal. As the creation of kinks seems to be suppressed in the center, its probability increases towards the edges of the crystal.

As a future perspective for the acquisitions of this work in terms of the trap development several points may be named.

Within the current setup, magnetic field measurements may be carried out in all three trap segments in order to characterize the field distribution within the prototype trap to evaluate the influence of external stray fields and field gradients, for example due to the ion-getter pump and the earth-magnetic field. This is important to give an estimate of the uncertainties depending on inhomogeneous magnetic fields and the size of the ion chains.

With compensation of the magnetic fields, detailed spectroscopy of the  $^2F_{7/2} \leftrightarrow ^1[5/2]_{5/2}$  transition of  $^{172}\text{Yb}^+$  may be done, in order to provide experimental data on the level structure of this theoretically non-trivial transition.

In terms of trap development, the realization of an ion trap based on AlN wafers with fully non-magnetic parts comes within reach, as laser cutting and coating techniques are currently optimized. The rigid structure together with low machining tolerances should lead to further reduction of axial rf fields due to machining tolerances. Currently under investigation is the heat distribution in a Rogers 4305<sup>TM</sup> model trap. This will help to estimate the uncertainty of frequency shifts due to blackbody radiation and is expected to be significantly reduced in an AlN based trap.

The first successful loading and trapping of mixed  $^{172}\text{Yb}^+ / ^{115}\text{In}^+$  Coulomb crystals (see Fig. 7.2) allows for the detailed experimental analysis of the crystal mode structure as a prerequisite to efficient sub-Doppler cooling, which is an inevitable step forward for

---

<sup>2</sup>As this should happen on time scales given by the axial trap frequency, this dynamics cannot be resolved with exposure times of tens of milliseconds.

recoil-free clock spectroscopy. This will be done with the stable laser which is currently being set up to drive the  ${}^2D_{5/2} \leftrightarrow {}^2S_{1/2}$  transition.

Mastering these preparatory tasks, paves the way towards versatile quantum sensors incorporated by laser cooled Coulomb crystals that can be manipulated in a well-controlled environment. These may find applications in optical frequency standards based on many  ${}^{115}\text{In}^+$  ions or precision spectroscopy with unprecedented resolution. Portable systems allow for applications in geodesy and navigation in space on a new level.



**Figure 7.2:** Coulomb crystal with  ${}^{172}\text{Yb}^+$  ions fluorescing at 369 nm and sympathetically cooled  ${}^{115}\text{In}^+$  ions (indicated by white circles). The indium ions are confirmed by measuring the mass-dependent secular modes of the crystal via parametric excitation.

# Appendix A

## DC control schematic

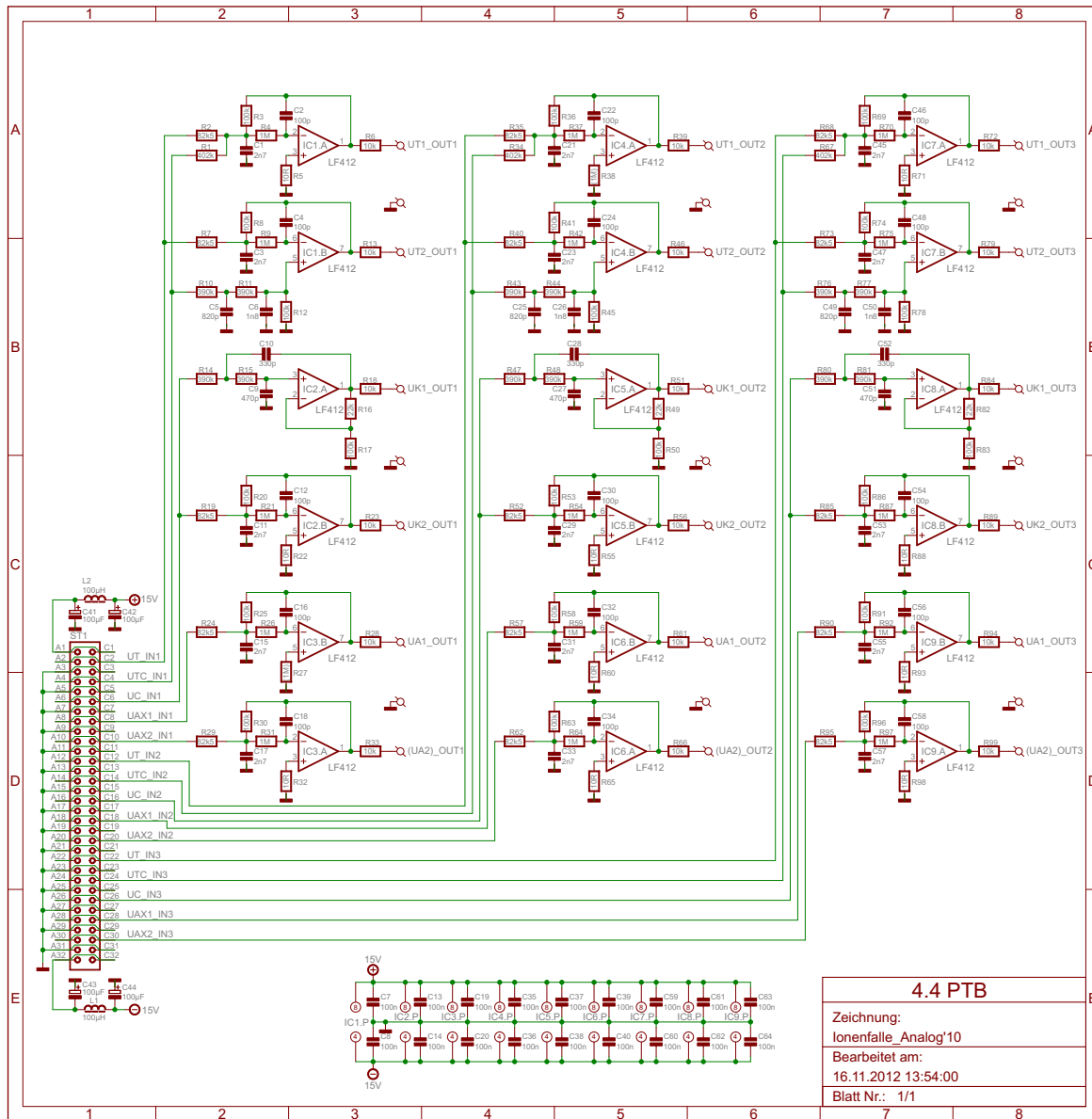


Figure A.1: Schematic of the dc control unit.



# Bibliography

- [1] F. Riehle, *Frequency Standards: Basics and Applications*. Wiley-VCH, 2004. 7
- [2] T. Rosenband *et al.*, “Frequency ratio of  $\text{Al}^+$  and  $\text{Hg}^+$  single-ion optical clocks; metrology at the 17th decimal place,” *Science*, vol. 319, no. 5871, pp. 1808–1812, 2008. 7, 12, 13
- [3] C. W. Chou, D. B. Hume, T. Rosenband, and D. J. Wineland, “Optical clocks and relativity,” *Science*, vol. 329, no. 5999, pp. 1630–1633, 2010. 7
- [4] L. Essen and J. V. L. Parry, “An atomic standard of frequency and time interval: A Caesium resonator,” *Nature*, vol. 176, pp. 280–282, 1955. 8
- [5] T. W. Hänsch and A. L. Schawlow, “Cooling of gases by laser radiation,” *Optics Communications*, vol. 13, no. 1, pp. 68–69, 1975. 8
- [6] D. J. Wineland and H. G. Dehmelt, “Principles of the stored ion calorimeter,” *Journal of Applied Physics*, vol. 46, no. 2, pp. 919–930, 1975. 8
- [7] D. J. Wineland, R. E. Drullinger, and F. L. Walls, “Radiation-pressure cooling of bound resonant absorbers,” *Physical Review Letters*, vol. 40, no. 25, pp. 1639–1642, 1978. 8
- [8] W. Neuhauser, M. Hohenstatt, P. Toschek, and H. Dehmelt, “Visual observation and optical cooling of electrostatically contained ions,” *Applied Physics A: Materials Science & Processing*, vol. 17, no. 2, pp. 123–129, 1978. 8
- [9] M. A. Kasevich, E. Riis, S. Chu, and R. G. DeVoe, “RF Spectroscopy in an Atomic Fountain,” *Physical Review Letters*, vol. 63, no. 6, pp. 612–615, 1989. 8
- [10] A. Clairon, C. Salomon, S. Guellati, and W. D. Phillips, “Ramsey resonance in a zacharias fountain,” *Europhysics letters*, vol. 16, no. 2, pp. 165–170, 1991. 8
- [11] W. Neuhauser, M. Hohenstatt, P. E. Toschek, and H. Dehmelt, “Localized visible  $\text{Ba}^+$  mono-ion oscillator,” *Physical Review A*, vol. 22, no. 3, p. 1137, 1980. 8
- [12] H. G. Dehmelt, “Mono-ion oscillator as potential ultimate laser frequency standard,” in *35th Annual Frequency Control Symposium. 1981*. IEEE, 1981, pp. 596–601. 8

- [13] B. C. Young, F. C. Cruz, W. M. Itano, and J. C. Bergquist, “Visible lasers with subhertz linewidths,” *Physical Review Letters*, vol. 82, no. 19, pp. 3799–3802, 1999. 8
- [14] T. Kessler, C. Hagemann, C. Grebing, T. Legero, U. Sterr, F. Riehle, M. J. Martin, L. Chen, and J. Ye, “A sub-40-mhz-linewidth laser based on a silicon single-crystal optical cavity,” *Nature Photonics*, vol. 6, no. 10, pp. 687–692, 2012. 8
- [15] D. J. Jones, S. A. Diddams, J. K. Ranka, A. Stentz, R. S. Windeler, J. L. Hall, and S. T. Cundiff, “Carrier-envelope phase control of femtosecond mode-locked lasers and direct optical frequency synthesis,” *Science*, vol. 288, no. 5466, pp. 635–639, 2000. 8
- [16] C. W. Chou, D. B. Hume, J. C. J. Koelemeij, D. J. Wineland, and T. Rosenband, “Frequency comparison of two high-accuracy  $\text{Al}^+$  optical clocks,” *Physical Review Letters*, vol. 104, p. 070802, 2010. 8, 13
- [17] P. O. Schmidt, T. Rosenband, C. Langer, W. M. Itano, J. C. Bergquist, and D. J. Wineland, “Spectroscopy Using Quantum Logic,” *Science*, vol. 309, no. 5735, pp. 749–752, 2005. 8, 10
- [18] M. Roberts, P. Taylor, G. P. Barwood, P. Gill, H. A. Klein, and W. R. C. Rowley, “Observation of an electric octupole transition in a single ion,” *Physical Review Letters*, vol. 78, pp. 1876–1879, 1997. 8, 44
- [19] N. Herschbach, K. Pyka, J. Keller, and T. E. Mehlstäubler, “Linear paul trap design for an optical clock with coulomb crystals,” *Applied Physics B*, vol. 107, no. 4, pp. 891–906, 2012. 8, 10, 12, 21, 22, 24, 72, 75, 77
- [20] C. Champenois, M. Marciante, J. Pedregosa-Gutierrez, M. Houssin, M. Knoop, and M. Kajita, “Ion ring in a linear multipole trap for optical frequency metrology,” *Physical Review A*, vol. 81, p. 043410, 2010. 8
- [21] M. J. Madsen, W. K. Hensinger, D. Stick, J. A. Rabchuk, and C. Monroe, “Planar ion trap geometry for microfabrication,” *Physical Review B: Lasers and Optics*, vol. 78, pp. 639–651, 2004. 9, 16, 30
- [22] J. P. Home and A. M. Steane, “Electrode configurations for fast separation of trapped ions,” *Quantum Information & Computation*, vol. 6, no. 4, pp. 289–325, 2006. 9
- [23] D. Stick, W. K. Hensinger, S. Olmschenk, M. J. Madsen, K. Schwab, and C. Monroe, “Ion trap in a semiconductor chip,” *Nature Physics*, vol. 2, no. 1, pp. 36–39, 2006. 9
- [24] S. Schulz, U. Poschinger, K. Singer, and F. Schmidt-Kaler, “Optimization of segmented linear paul traps and transport of stored particles,” *Fortschritte der Physik*, vol. 54, pp. 648–665, 2006. 9

- [25] W. K. Hensinger, S. Olmschenk, D. Stick, D. Hucul, M. Yeo, M. Acton, L. Deslauriers, J. Rabchuk, and C. Monroe, “T-junction ion trap array for two-dimensional ion shuttling, storage and manipulation,” *Physical Review Letters*, vol. 88, p. 034101, 2006. 9
- [26] D. R. Leibbrandt *et al.*, “Demonstration of a scalable, multiplexed ion trap for quantum information processing,” *arXiv:0904.2599*, 2009. 9
- [27] U. Tanaka, R. Naka, F. Iwata, T. Ujamaru, K. R. Brown, I. L. Chuang, and S. Urabe, “Design and characterization of a planar trap,” *Journal of Physics B: Atomic, Molecular and Optical Physics*, vol. 42, no. 15, p. 154006, 2009. 9
- [28] C. E. Pearson, D. R. Leibbrandt, W. S. Bakr, W. J. Mallard, K. R. Brown, and I. L. Chuang, “Experimental investigation of planar ion traps,” *Physical Review A*, vol. 73, p. 032307, march 2006. 9
- [29] D. T. C. Allcock *et al.*, “Heating rate and electrode charging measurements in a scalable, microfabricated, surface-electrode ion trap,” *Applied Physics B*, vol. 107, no. 4, pp. 913–919, 2012. 9
- [30] Q. A. Turchette *et al.*, “Heating of trapped ions from the quantum ground state,” *Physical Review A*, vol. 61, no. 6, p. 063418, 2000. 9, 12, 17
- [31] N. Daniilidis, S. Narayanan, S. A. Möller, R. Clark, T. E. Lee, P. J. Leek, A. Wallraff, S. Schulz, F. Schmidt-Kaler, and H. Häffner, “Fabrication and Heating Rate Study of Microscopic Surface Electrode Ion Traps,” *New Journal of Physics*, vol. 13, no. 1, p. 013032, 2011. 9, 17
- [32] E. Peik, G. Hollemann, and H. Walther, “Laser cooling and quantum jumps of a single indium ion,” *Physical Review A*, vol. 49, no. 1, p. 402, 1994. 10
- [33] T. Liu *et al.*, “Frequency control symposium, 2007 joint with the 21st european frequency and time forum,” in *IEEE International*, vol. 407, 2007. 10
- [34] J. A. Sherman, W. Trimble, S. Metz, W. Nagourney, and N. Fortson, “Progress on indium and barium single ion optical frequency standards,” in *LEOS Summer Topical Meetings, 2005 Digest of the*. IEEE, 2005, pp. 99–100. 10
- [35] C. Schwedes, E. Peik, J. Von Zanthier, A. Y. Nevsky, and H. Walther, “Narrow-bandwidth diode-laser-based blue and ultraviolet light source,” *Applied Physics B: Lasers and Optics*, vol. 76, no. 2, pp. 143–147, 2003. 10
- [36] J. B. Wübbena, S. Amairi, O. Mandel, and P. O. Schmidt, “Sympathetic cooling of mixed-species two-ion crystals for precision spectroscopy,” *Physical Review A*, vol. 85, p. 043412, 2012. 11
- [37] K. Sugiyama and J. Yoda, “Production of  $\text{YbH}^+$  by chemical reaction of  $\text{Yb}^+$  in excited states with  $\text{H}_2$  gas,” *Physical Review A*, vol. 55, p. 10, 1997. 11

- [38] D. J. Berkeland, J. D. Miller, J. C. Bergquist, W. M. Itano, and D. J. Wineland, "Minimization of ion micromotion in a Paul trap," *Journal of Applied Physics*, vol. 83, pp. 5025–5033, 1998. 12, 13, 16, 19, 67, 68
- [39] E. Peik, J. Abel, T. Becker, J. Von Zanthier, and H. Walther, "Sideband cooling of ions in radio-frequency traps," *Physical Review A*, vol. 60, no. 1, p. 439, 1999. 12
- [40] L. Deslauriers, S. Olmschenk, D. Stick, W. K. Hensinger, J. Sterk, and C. Monroe, "Scaling and suppression of anomalous heating in ion traps," *Physical Review Letters*, vol. 97, no. 10, p. 103007, 2006. 12
- [41] R. J. Epstein *et al.*, "Simplified motional heating rate measurements of trapped ions," *Physical Review A*, vol. 76, no. 3, p. 033411, 2007. 12
- [42] M. S. Safronova, M. G. Kozlov, and C. W. Clark, "Precision calculation of blackbody radiation shifts for optical frequency metrology," *Physical Review Letters*, vol. 107, p. 143006, 2011. 12, 13
- [43] T. Rosenband, W. M. Itano, P. O. Schmidt, D. B. Hume, J. C. J. Koelemeij, J. C. Bergquist, and D. J. Wineland, "Blackbody radiation shift of the  $^{27}\text{Al}^+ \ ^1\text{S}_0 \rightarrow \ ^3\text{P}_0$  transition," in *20th European Frequency and Time Forum (EFTF)*. IEEE, 2006, pp. 289–292. 12
- [44] T. Becker, J. V. Zanthier, A. Y. Nevsky, C. Schwedes, M. N. Skvortsov, H. Walther, and E. Peik, "High-resolution spectroscopy of a single  $\text{in}^+$  ion: Progress towards an optical frequency standard," *Physical Review A*, vol. 63, no. 5, p. 051802, 2001. 13
- [45] J. E. Bernard and A. A. Marmet, L. and Madej, "A laser frequency lock referenced to a single trapped ion," *Optics communications*, vol. 150, no. 1, pp. 170–174, 1998. 13
- [46] F. G. Major, V. N. Gheorghie, and G. Werth, *Charged Particle Traps: Physics and Techniques of Charged Particle Field Confinement*. Springer, 2004, vol. 37. 13, 17
- [47] P. K. Ghosh, *Ion Traps*. Clarendon Press Oxford, 1995. 13
- [48] C. A. Schrama, E. Peik, W. W. Smith, and H. Walther, "Novel Miniature Ion Traps," *Optics Communication*, vol. 101, pp. 32–36, 1993. 16
- [49] K. Smith and R. E. Alley, *Electrical Circuits: An Introduction*. Cambridge University Press, 1992. 20
- [50] B. C. Fawcett and M. Wilson, "Computed Oscillator Strengths, and Landé g-Values, and Lifetimes in Yb II," *Atomic Data and Nuclear Data Tables*, vol. 47, p. 241, 1991. 43, 44, 70
- [51] M. M. Schauer, J. R. Danielson, A. T. Nguyen, L. B. Wang, X. Zhao, and J. R. Torgerson, "Collisional population transfer in trapped  $\text{Yb}^+$  ions," *Physical Review A*, vol. 79, p. 062705, Jun 2009. 43

- [52] D. Das, S. Barthwal, A. Banerjee, and V. Natarajan, “Absolute frequency measurements in Yb with 0.08 ppb uncertainty: Isotope shifts and hyperfine structure in the 399 nm  $^1S_0 \rightarrow ^1P_1$  line,” *Physical Review A*, vol. 72, p. 032506, 2005. 50
- [53] Y. H. Wang, T. Liu, R. Dumke, A. Stejskal, Y. N. Zhao, J. Zhang, Z. H. Lu, L. J. Wang, T. Becker, and H. Walther, “Improved absolute frequency measurement of the  $^{115}\text{In}^+ 5s^2 ^1S_0\text{-}5s5p ^3P_0$  narrowline transition: Progress towards an optical frequency standard,” *Laser physics*, vol. 17, no. 7, pp. 1017–1024, 2007. 51
- [54] W. W. Macalpine and R. O. Schildknecht, “Coaxial Resonators with Helical Inner Conductor,” in *Proceedings of the Institute of Radio Engineers*, 1959, p. 2099. 52
- [55] P. D. Lett, W. D. Phillips, S. L. Rolston, C. E. Tanner, R. N. Watts, and C. I. Westbrook, “Optical molasses,” *Journal of the Optical Society of America B*, vol. 6, no. 11, pp. 2084–2107, 1989. 63
- [56] E. Peik, “Laserspektroskopie an gespeicherten In-Ionen,” Ph.D. dissertation, Max-Planck-Institut für Quantenoptik, 1993. 69
- [57] K. Pyka *et al.*, “Symmetry breaking and topological defect formation in ion coulomb crystals,” *arXiv:1211.7005*, 2012. 87
- [58] T. W. B. Kibble, “Topology of cosmic domains and strings,” *Journal of Physics A: Mathematical and General*, vol. 9, p. 1387, 1976. 88
- [59] T. W. B. Kibble, “Some implications of a cosmological phase transition,” *Physics Reports*, vol. 67, no. 1, pp. 183–199, 1980. 88
- [60] W. H. Zurek, “Cosmological experiments in superfluid helium?” *Nature*, vol. 317, no. 6037, pp. 505–508, 1985. 88
- [61] W. H. Zurek, “Cosmological experiments in condensed matter systems,” *Physics Reports*, vol. 276, no. 4, pp. 177–221, 1996. 88
- [62] S. M. Griffin, M. Lilienblum, K. Delaney, Y. Kumagai, M. Fiebig, and N. A. Spaldin, “From multiferroics to cosmology: Scaling behaviour and beyond in the hexagonal manganites,” *arXiv:1204.3785*, 2012. 88
- [63] I. Chuang, R. Durrer, N. Turok, and B. Yurke, “Cosmology in the laboratory: Defect dynamics in liquid crystals,” *Science*, vol. 251, no. 4999, pp. 1336–1342, 1991. 88
- [64] M. J. Bowick, L. Chandar, E. A. Schiff, and A. Srivastava, “The Cosmological Kibble Mechanism in The Laboratory: String Formation in Liquid Crystals,” *Science*, vol. 263, no. 5149, pp. 943–945, 1994. 88

- [65] R. Monaco, J. Mygind, M. Aarøe, R. Rivers, and V. Koshelets, “Zurek-Kibble Mechanism for The Spontaneous Vortex Formation in Nb-Al/Al-ox/Nb Josephson Tunnel Junctions: New Theory and Experiment,” *Physical Review Letters*, vol. 96, no. 18, 2006. 88
- [66] L. E. Sadler, J. M. Higbie, S. R. Leslie, M. Vengalattore, and D. M. Stamper-Kurn, “Spontaneous symmetry breaking in a quenched ferromagnetic spinor Bose-Einstein condensate,” *Nature*, vol. 443, no. 7109, pp. 312–315, 2006. 88
- [67] C. N. Weiler, T. W. Neely, D. R. Scherer, A. S. Bradley, M. J. Davis, and B. P. Anderson, “Spontaneous vortices in the formation of Bose-Einstein condensates,” *Nature*, vol. 455, no. 7215, pp. 948–951, 2008. 88
- [68] E. M. Lifshitz and L. P. Pitaevskii, “Landau and Lifshitz Course of Theoretical Physics. Statistical Physics, Vol. 5,” 1980. 88
- [69] V. L. Ginzburg and L. D. Landau, “On the theory of superconductivity,” in *On Superconductivity and Superfluidity*. Springer, 2009, pp. 113–137. 88
- [70] B. Damski and W. H. Zurek, “Soliton creation during a Bose-Einstein Condensation,” *Physical Review Letters*, vol. 104, p. 160404, 2010. 88
- [71] A. del Campo, G. De Chiara, G. Morigi, M. B. Plenio, and A. Retzker, “Structural defects in ion chains by quenching the external potential: The inhomogeneous Kibble-Zurek mechanism,” *Physical Review Letters*, vol. 105, no. 7, p. 075701, 2010. 88, 89, 90, 103
- [72] H. Saito, Y. Kawaguchi, and M. Ueda, “Kibble-Zurek mechanism in a quenched ferromagnetic Bose-Einstein condensate,” *Physical Review A*, vol. 76, no. 4, 2007. 88, 91
- [73] R. Monaco, J. Mygind, and R. J. Rivers, “Zurek-Kibble domain structures: The dynamics of spontaneous vortex formation in annular Josephson tunnel junctions,” *Physical Review Letters*, vol. 89, no. 8, 2002. 88
- [74] R. Monaco, J. Mygind, R. Rivers, and V. Koshelets, “Spontaneous fluxoid formation in superconducting loops,” *Physical Review B*, vol. 80, no. 18, 2009. 88, 89, 91
- [75] W. H. Zurek, “Causality in condensates: Gray solitons as relics of BEC formation,” *Physical Review Letters*, vol. 102, no. 10, 2009. 89
- [76] G. D. Chiara, A. d. Campo, G. Morigi, M. B. Plenio, and A. Retzker, “Spontaneous nucleation of structural defects in inhomogeneous ion chains,” *New Journal of Physics*, vol. 12, no. 11, p. 115003, 2010. 89, 91, 94

- [77] J. Sabbatini, W. H. Zurek, and M. J. Davis, “Causality and defect formation in the dynamics of an engineered quantum phase transition in a coupled binary Bose-Einstein condensate,” *New Journal of Physics*, vol. 14, no. 9, p. 095030, 2012. 89
- [78] A. Retzker, R. Thompson, D. Segal, and M. Plenio, “Double well potentials and quantum phase transitions in ion traps,” *Physical Review Letters*, vol. 101, no. 26, 2008. 90
- [79] S. Fishman, G. De Chiara, T. Calarco, and G. Morigi, “Structural phase transitions in low-dimensional ion crystals,” *Physical Review B*, vol. 77, no. 6, p. 064111, 2008. 90
- [80] A. Steane, “The ion trap quantum information processor,” *Applied Physics B: Lasers and Optics*, vol. 64, no. 6, pp. 623–643, 1997. 90
- [81] D. H. E. Dubin, “Theory of structural phase transitions in a trapped Coulomb crystal,” *Physical Review Letters*, vol. 71, no. 17, pp. 2753–2756, 1993. 90
- [82] P. Laguna and W. H. Zurek, “Critical dynamics of symmetry breaking: Quenches, dissipation, and cosmology,” *Physical Review D*, vol. 58, no. 8, p. 085021, 1998. 91
- [83] H. J. Metcalf and P. Van der Straten, *Laser Cooling and Trapping*. Springer Verlag, 1999. 91
- [84] A. del Campo, A. Retzker, and M. B. Plenio, “The inhomogeneous Kibble-Zurek mechanism: Vortex nucleation during Bose-Einstein condensation,” *New Journal of Physics*, vol. 13, no. 8, p. 083022, 2011. 91
- [85] J. Dziarmaga, “Dynamics of a quantum phase transition and relaxation to a steady state,” *Advances in Physics*, vol. 59, no. 6, pp. 1063–1189, 2010. 91
- [86] H. Landa, S. Marcovitch, A. Retzker, M. B. Plenio, and B. Reznik, “Quantum coherence of discrete kink solitons in ion traps,” *Physical Review Letters*, vol. 104, no. 4, p. 043004, 2010. 92
- [87] K. Kuhlmann, “Untersuchung des Inhomogenen Kibble-Zurek-Mechanismus in  $^{172}\text{Yb}^+$ -Coulomb-Kristallen,” Master’s thesis, Technische Universität Braunschweig, 2012. 92
- [88] D. M. Meier, “Ein Lasersystem zur Seitenbandspektroskopie von gemischten  $\text{In}^+/\text{Yb}^+$  Kristallen,” Master’s thesis, Technische Universität Braunschweig, 2012. 93, 94
- [89] O. M. Braun and Y. S. Kivshar, *The Frenkel-Kontorova Model: Concepts, Methods, and Applications*. Springer Verlag, 2004. 95





## Acknowledgments

At this point, I would like to thank all the people that helped me with this work. And I have to apologize, because I am not a sentimental guy, so please be assured that I really mean it when I say thank you.

First of all, there is Dr. Tanja E. Mehlstäubler who gave me the chance of being part of this project and always gave me the right push when I thought I didn't need it, although I did. It was particularly fun to see the empty lab getting filled up with technology and people and to see things working for the first time. Being the first in an empty lab is awesome and awful at the same time, but mostly awesome. Especially now that everything is running.

Second, I would like to thank Prof. Piet O. Schmidt, Prof. Christian Ospelkaus and Prof. Louis Santos for agreeing to referee this manuscript. I really appreciate it.

A particular thank you goes to all the people of the time and frequency division for sharing their experience and resources. Dr. Ekkehard Peik for his helpful advice and support. Martina Bäuml for helping me through the administrative procedures in the PTB. Hans-Albert Kremling, Thomas Leder and Sven Krenauer for their mechanical support and Burghard Lippert, Andreas Hoppmann and Michael Kazda for the electronic support.

A very special thanks goes to Norbert Herschbach, who has a lot of experience and an explanation for everything. It was a pleasure to set up everything with him. Jonas Keller is a great colleague to work with and to order pizza at night, and to correct my english from time to time. Many thanks goes to Lin Yi, who contributed a lot to the experiment in his short period in our group. It was a pleasure to work with you.

A special thanks goes to the rest of the Quest team, for a nice atmosphere in the office, for fruitful discussions about physics and everything else, for the pleasant group trips and christmas parties and more. Börge Hemmerling, Jannes Wübbena, Olaf Mandel, Florian Gebert, Yong Wan, Nils Scharnhorst, it was a pleasure. Sandra Ludwig gave great administrative support. Peter-Christian Carstens for his electronic support, as well as Christopher Bleuel and Olga Lick. Sven Klitzing and Alexander Pablocki for their mechanical support. Sven and Börge shared their appreciation of a good coffee, this is what Premium-usership is really about. It was a pleasure to give advice and share the lab with Kristijan Kuhlmann and David-Marcel Meier, as well as the monday night sneak peek. I also would like to thank my new colleagues, that will take over the experiment together with Jonas, Tobias Burgermeister and Heather Partner, who helped a lot in putting this thesis in a better shape. Thanks also for contributing that much to the paper. I will particularly miss the nights in the Roots sports bar to play billiards with Norbert, Jonas and Sven and sometimes Jannes.

The most thanks I have to give to my family for being the constant and ground in my life. At last, because I cannot express how important she is, I thank my wife Sana (thanks again Piet for hiring her) for always believing in me, for supporting me in particular in the final period of writing and for being this wonderful person. I hope I can give you half as much support, when it's your turn.

نحبك انت حبيبي



# Curriculum vitae

Karsten Pyka

## Contact information

karstenpyka@googlemail.com

## Personal information

Date of birth: 17.01.1983

Place of birth: Röbel/Müritz

Nationality: German

## Education

- 03/2009-04/2013    **Physikalisch-Technische Bundesanstalt, Leibniz Universität Hannover**, Germany  
Graduate student in the group of Dr. Tanja E. Mehlstäubler at the QUEST institute for experimental quantum metrology and at the time and frequency division  
Thesis topic: *High-precision ion trap for a multi-ion optical clock*  
Ph.D. thesis defense on May 14, 2013
- 10/2003-09/2008    **Universität Hamburg**, Germany  
Diploma student in the group of Prof. Klaus Sengstock at the Institute for laser physics  
Diploma thesis title: *Bragg-spectroscopy of degenerate quantum gases in optical lattices*
- 06/2002    **Joliot-Curie Gymnasium**, Germany  
Abitur

## List of publications

1. K. Pyka *et al.* Symmetry Braking and Topological Defect Formation in Ion Coulomb Crystals. *arXiv:1211.7005*, 2012.
2. K. Pyka, N. Herschbach, J. Keller and T. E. Mehlstäubler. A high-precision rf trap with minimized micromotion for an  $\text{In}^+$  multiple-ion clock. *arXiv:1206.5111*, 2012.
3. N. Herschbach, K. Pyka, J. Keller and T. E. Mehlstäubler. Linear Paul trap design for an optical clock with Coulomb crystals. *Applied Physics B: Lasers and Optics*, vol. 107, pp. 891–906, 2011.
4. P. T. Ernst, S. Götze, J. S. Krauser, K. Pyka, D.-S. Lühmann, D. Pfannkuche and K. Sengstock. Probing superfluids in optical lattices by momentum-resolved Bragg spectroscopy. *Nature Physics*, vol. 6, 2010.